

**Gas-Phase Methane Oxidation Investigated by
Laser-Induced Fluorescence, Species Profile Measurements
and Kinetic Reactor Simulations**

vorgelegt von
Dipl.-Ing.
Heiner Schwarz
aus Aachen

Von der Fakultät II – Mathematik und Naturwissenschaften
der Technischen Universität Berlin
zur Erlangung des akademischen Grades

Doktor der Ingenieurwissenschaften
– Dr.-Ing. –

genehmigte Dissertation

Promotionsausschuss:

Vorsitzender: Prof. Dr. Thorsten Ressler
Berichter/Gutachter: Prof. Dr. Robert Schlögl
Berichter/Gutachter: Prof. Dr. Reinhard Schomäcker
Berichter/Gutachter: Prof. Dr. Thomas Risse

Tag der wissenschaftlichen Aussprache: 12. Dezember 2013

Berlin 2013
D 83

“Vielfach sind allerdings Versuche unternommen worden, um für verschiedene Materialien die Menge und Leuchtkraft des aus der Gewichtseinheit erzeugbaren Gases kennen zu lernen, es ist von einzelnen Forschern auch die Zusammensetzung der erhaltenen Gase untersucht worden, aber es fehlt an Versuchen, welche alle Zersetzungsproducte in den Kreis ihrer Aufgaben einbeziehen, sie quantitativ bestimmen und damit ein vollständiges Bild des Vorganges gewähren.”

Fritz Haber, *Experimental-Untersuchungen über die Zersetzung und Verbrennung von Kohlenwasserstoffen*, 1896, Habilitationsschrift, Technische Hochschule Karlsruhe

Zusammenfassung

Seit dem Beginn der Industrialisierung Ende des neunzehnten Jahrhunderts ist Methan sowohl für die Energieerzeugung als auch bei der chemischen Synthese von zentraler Bedeutung. Die Erschließung neuer Erdgasvorkommen sowie geostrategische Interessen befeuern gegenwärtig Bestrebungen Erdgas als Rohstoffersatz für Eröl einzusetzen.

In der vorliegenden Dissertation wird Methanoxidation in der Gasphase unter industriellen Bedingungen untersucht, d.h. bei hohen Temperaturen und Drücken. Anlass dazu gibt das Bestreben, die Wechselwirkung von homogenen und heterogenen Reaktionen modellieren zu können, was wiederum von der Vorhersagegenauigkeit des verwendeten kinetischen Reaktionsmechanismus abhängt. Die durchgeführten Experimente zielen darauf ab, der Fachliteratur entnommene Reaktionsmechanismen zu beurteilen, insbesondere in Hinblick auf die oxidative Kopplung von Methan (im Englischen Oxidative Coupling of Methane, OCM). Der grundlegende Ansatz besteht darin, Reaktionsprofile zu messen und mit kinetischen numerischen Simulationen zu vergleichen. Von zentraler Bedeutung ist hierbei der von der Arbeitsgruppe entwickelte Profilreaktor. Da die Gasphasen-Methanoxidation über Radikal-Kettenreaktionen abläuft, liegt ein Schwerpunkt dieser Arbeit auf (i) der Entwicklung einer optischen Sonde zur Detektion transientser Spezies mittels Laser-Induzierter Fluoreszenz (LIF), sowie (ii) der Modellierung des Reaktors unter Zuhilfenahme kinetischer numerischer Simulationen, um die verwendeten Reaktionsmechanismen zu testen, die experimentellen Ergebnisse zu interpretieren und die Reaktionspfade nachzuvollziehen.

Eine neuartige Methodik wurde entwickelt, welche LIF Messungen durch eine optische Faser erlaubt und somit Zugang zu sonst optisch unzugänglichen Systemen gewährt. Auf diese Weise ist es nun möglich transiente Spezies nachzuweisen, welche bislang nicht detektierbar waren. Im Zuge der Arbeit wurden verschiedene Sonden-geometrien erprobt und die Methodik sowohl an Hydroxyl Radikalen (OH) als auch Formaldehyd (CH_2O) demonstriert. Außerdem wurde Schwingungs-Raman Thermometrie durch eine optische Faser erprobt, jedoch mangels eines geeigneten Markermoleküls nicht weiter verfolgt.

Die oxidative Kopplung von Methan in der Gasphase bei einem CH_4/O_2 Verhältnis von 8 wurde in einem Hochdruck-Durchflussreaktor untersucht. Dabei wurden die gemessenen Reaktionsprofile mit numerischen Strömungssimulationen (im Englischen Computational Fluid Dynamics, CFD), basierend auf einem geeigneten Reaktionsmechanismus, verglichen. Es stellt sich heraus, dass die Übereinstimmung in Bezug auf die Primärprodukte zufriedenstellend ist, jedoch wird insbesondere die Entstehung der C_2 Spezies weniger gut vorhergesagt. Auf Basis der Simulationen wurde eine Reaktionspfadanalyse durchgeführt, welche hilfreich für die Entwicklung effizienterer Prozesse sein kann.

Um die Detektierbarkeit von OH Radikalen unter fetten Bedingungen (Methan-

überschuss) zu eruieren, wurden Experimente durchgeführt, bei denen die Reaktion an einem Platinnetz verankert wurde. Unter mageren Bedingungen (Sauerstoffüberschuss, $\phi = 0.5$) ist die Detektion von OH ohne weiteres möglich, wobei OH unter diesen Bedingungen als Quasi-Gleichgewichtsprodukt vorliegt und hauptsächlich in der post-Reaktionszone aufzufinden ist. Unter fetten Bedingungen ($\phi = 2.0$) konnte hingegen kein OH detektiert werden, da die Konzentrationen unterhalb der Detektionsgrenze (~ 1 ppm) zu liegen scheinen. Somit ist die Detektion bei fetteren Gemischen, wobei noch geringere Konzentrationen zu erwarten sind, unwahrscheinlich. Die experimentellen Daten beider Bedingungen wurden mit Gasphasen-Simulationen verglichen und der katalytische Einfluss auf die Reaktion aufgezeigt.

In Bezug auf die Detektion von OH Radikalen kann geschlussfolgert werden, dass die Sensitivität von (durch eine optische Faser gemessener) LIF nicht ausreicht, um Konzentrationsprofile unter industriellen Bedingungen zu messen. Andere (spektroskopische) Methoden sind erforderlich, um OH in fetten Gemischen nachzuweisen.

Es konnte gezeigt werden, dass kinetische Simulationen ein wertvolles Hilfsmittel für die Interpretation experimenteller Ergebnisse darstellen. Die kinetischen Simulationen sind komplex und gleichzeitig Rechenzeit-intensiv, so dass es notwendig ist, einen Kompromiss zwischen der Komplexität des verwendeten Reaktormodells und dem Umfang des chemischen Mechanismus zu finden. Trotz jahrzehntelanger Bemühungen scheint es keinen universellen Mechanismus zu geben, der in allen stöchiometrischen Regimes exakte Vorhersagen liefert. Diese Beobachtung ist von Bedeutung für die Entwicklung eines Modells für die Kopplung homogener und heterogener Reaktionen. Nahe der Katalysatoroberfläche, d.h. in der katalytischen Grenzschicht, können die partiellen Drücke stark von der globalen Stöchiometrie abweichen, was wiederum Auswirkungen auf die Aussagekraft des Mechanismus haben kann.

Abstract

Methane conversion with respect to energy production as well as for chemical synthesis has been of perpetual importance since the dawn of the industrialization at the end of the nineteenth century. The interest in natural gas as an alternative feedstock to crude oil is currently boosted by the exploitation of newly available resources and geostrategical considerations.

In this thesis kinetics of gas-phase methane oxidation is investigated under industrially relevant conditions, namely high temperature and pressures. The work is motivated by the vision to build a model for homogeneous-heterogeneous coupling which crucially depends on the accuracy of the gas-phase kinetic mechanism. With this intention, experiments are performed to evaluate the performance of state-of-the-art kinetic mechanisms taken from literature, in particular with respect to oxidative coupling of methane (OCM). The key-approach is based on species profile measurements in conjunction with kinetic numerical simulations. The kinetic profile reactor, which had been developed by our group, is central to these investigation. Gas-phase methane oxidation

involves radical chain reactions and therefore the work focuses on (i) the development of a fiber-optic probe to measure transient species using laser-induced fluorescence (LIF) spectroscopy and (ii) the use of reactor models and kinetic numerical simulations in order to prove the accuracy of the applied kinetic mechanism, interpret the experimental results, and unravel the underlying chemistry.

A novel technique was developed which permits LIF measurements through an optical-fiber in otherwise optically inaccessible systems. This allows to measure transient species in the profile reactor which were previously not detectable. Different fiber-optic probe geometries were developed and applied for detection of hydroxyl radicals (OH) and formaldehyde (CH₂O). Vibrational Raman thermometry is attempted through an optical fiber but discarded due to the lack of an appropriate probe molecule under the investigated conditions.

Oxidative coupling of methane in the gas-phase is investigated in a high-pressure flow reactor at a CH₄/O₂ feed ratio of 8. Species profiles were measured and compared to computational fluid dynamics (CFD) simulations based on an appropriate kinetic mechanism. The agreement of experiment and simulation for the primary species is good. However, in particular the evolution of the C₂ species appears to be captured less accurately by the state-of-the-art mechanism. A pathway analysis gives insight into the kinetics of fuel-rich methane oxidation, in particular with respect to C₂ formation. The information may be helpful in the design of efficient coupling processes.

Methane oxidation over a platinum gauze was studied with the intention to verify the feasibility of detecting OH radicals under methane-rich conditions. OH radicals were readily detected under lean (excess oxygen) conditions ($\phi = 0.5$) where OH is a quasi-equilibrium product appearing mainly in the post-reaction zone. Under methane-rich conditions with an equivalence ratio $\phi = 2.0$ OH concentrations appeared to be just below the detection limit of the technique (~ 1 ppm) and thus, detection at higher methane partial pressures, where OH concentrations are expected to be even lower, is unlikely. Both experiments were compared to gas-phase kinetic simulations illustrating the impact of heterogeneous chemistry in either case.

Concerning the detection of OH radicals, the sensitivity of (optical-fiber) LIF has been proved to be insufficient to measure species profiles under industrial conditions common to chemical synthesis. Other (spectroscopic) methods which provide higher sensitivities may have to be employed to detect OH under methane-rich conditions.

Kinetic simulations were shown to be an invaluable tool in interpreting the experimental data. However, reactor modeling is challenging and computationally expensive requiring a trade-off between the level of detail of the reactor model and the complexity of the chemical mechanism. In spite of decades of research a universal kinetic mechanism accurately describing gas-phase methane oxidation in all stoichiometric regimes is not yet available. This fact has to be taken into consideration when coupling the gas-phase chemistry to a catalytic mechanism in a homogeneous-heterogeneous model. In proximity to the catalyst, i.e. within the catalytic boundary-layer, the partial pressures may be substantially different from the bulk gas-phase and hence, the accuracy of the mechanism may become questionable.

Contents

Introduction	8
1 Motivation	9
1.1 Economic and Ecological Interest of Methane Conversion	9
1.2 Methane Oxidation Processes	11
1.2.1 Methane Combustion	11
1.2.2 Chemical Synthesis	12
1.3 Homogeneous-Heterogeneous Coupling in OCM	17
1.4 Objective and Outline of the Thesis	18
2 Theoretical Background	20
2.1 Optics	20
2.1.1 Maxwell's Equations	20
2.1.2 Classical Approach to Light-Matter Interaction	21
2.1.3 Molecular Scattering in Gases on a Macroscopic Scale	23
2.1.4 Absorption and Emission of Radiation	24
2.2 Statistical Thermodynamics	25
2.2.1 Derivation of Partition Function	25
2.2.2 Transition State Theory	27
2.3 Conservation Equations	28
2.3.1 General Formulation of Conservation Equations	28
2.3.2 Numerical Solution	31
2.4 Homogeneous-Heterogeneous Reactor Dynamics	31
3 Methodology	36
3.1 Laser Spectroscopic Methods	36
3.1.1 Raman Scattering	36
3.1.2 Laser-Induced Fluorescence (LIF)	37
3.1.3 Resonance-Enhanced Multi-Photon Ionization (REMPI)	42
3.2 In Situ Laser Diagnostics using Optical Fibers	43
3.2.1 Optical Fiber Probes	43
3.2.2 Raman Thermometry through an Optical Fiber	44
3.3 Capillary Sampling	44

Results	46
4 Radical Detection in Harsh Environments by Means of Laser-Induced Fluorescence using a Single Bidirectional Optical Fiber	47
4.1 Introduction	47
4.2 Experimental	49
4.2.1 Characterization of Laminar Premixed Flame	49
4.2.2 Fiber Coupling and Laser-Induced Scattering	50
4.3 Geometrical Considerations on Collection Efficiency	53
4.4 Results	55
4.4.1 Collection Efficiency and Detection Volume of Bidirectional Fiber	55
4.4.2 LIF OH Detection using Bidirectional Fiber Probe in Harsh Environment	57
4.5 Conclusion	57
5 Fuel-Rich Methane Oxidation in a High-Pressure Flow Reactor studied by Optical-Fiber Laser-Induced Fluorescence, Multi-Species Sampling Profile Measurements and Microkinetic Simulations	59
5.1 Introduction	60
5.2 Experimental Methods	61
5.2.1 Profile Reactor Measurements	61
5.2.2 Fiber-Optic LIF Detection of CH ₂ O	62
5.2.3 LIF Corrections	66
5.3 Kinetic Reactor Simulations	68
5.3.1 Mechanism Reduction	68
5.3.2 Reactor Modeling	71
5.4 Results and Discussion	72
5.4.1 CH ₂ O LIF Profile Measurements	72
5.4.2 Species Profiles	74
5.4.3 Kinetic Discussion	78
5.5 Conclusion	83
6 Methane Oxidation over a Platinum Gauze at $\phi = 0.5$ and 2.0	85
6.1 Introduction	85
6.2 Experimental	86
6.2.1 Sampling Reactor	86
6.2.2 Fiber-optic LIF	87
6.3 Results and Discussion	90
6.3.1 Lean Combustion Regime ($\phi = 0.5$)	90
6.3.2 Fuel-Rich Regime ($\phi = 2.0$)	93
7 Summary and Conclusions	95
Bibliography	96

Introduction

Chapter 1

Motivation

This chapter gives a general overview for the interest in methane conversion, followed by a brief synopsis of (oxidative) methane processes. From this follows the motivation and the objectives of the present work.

1.1 Economic and Ecological Interest of Methane Conversion

Since the end of the nineteenth century, the advancing industrialization and a growing world population go hand in hand with an escalating demand for energy and exploitation of resources. Despite political incentives and technological development for the use of renewable sources, on a global scale mankind's primary energy consumption depends almost exclusively on fossil fuels. Apart from the nuclear fuels and coal which are almost exclusively used for generating electricity, crude oil and natural gas constitute the principal resources for electricity generation, heating, transportation and industrial production. Increasing demand on the one hand, and dwindling reserves and exploitation of new resources on the other hand are reflected in the prices for the individual hydrocarbon fuels. Figure 1.1 shows the development of prices for natural gas and crude oil for different production sites during the last three decades. It can be seen that there has been a generally increasing price trend since the turn of the millennium for both fuels, followed by a sharp decline in 2008–2009 (top graph). Although this drop may be attributed to the global financial crisis there is another trend which is recovered by looking at the relative prices of natural gas compared to oil (bottom graph). Hydraulic fracturing, a production technology for shale gas which has become available in the United States, has led to a strong relative cost advantage of natural gas in the US. However, also on the European continent, where skepticism towards fracking is more pronounced and the technology has not yet been established on a large scale, the general price trend is slightly in favor of natural gas (the dashed lines indicate the linear regressions for the European NG prices). Besides, there are indications that peak oil production outside the Organization of the Petroleum Exporting Countries (OPEC) has already been reached [1] and also geostrategical struggles may threaten the global supply with oil in the future. Chemical industry has ever since relied predominantly on crude oil as the feedstock for the production of liquid fuels and base chemicals. In the light of the above trends, chemical companies as well as national economies currently strive for a strategic diversification of resources and the conversion of natural gas to

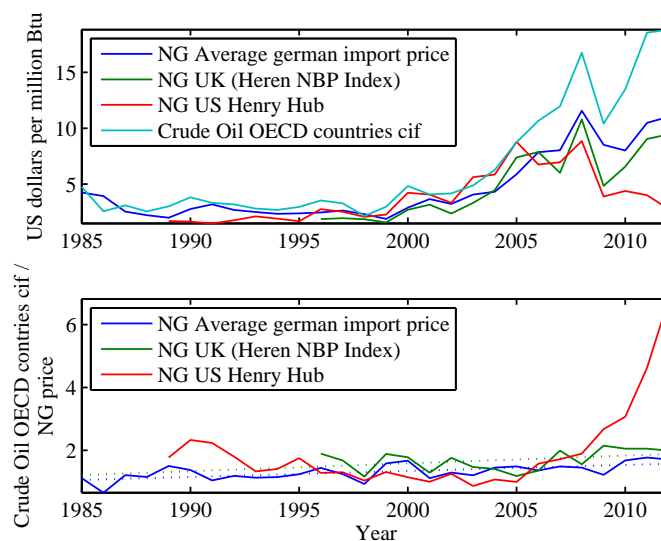


Figure 1.1: Natural gas (NG) and crude oil price trend (top), and ratio of crude oil price to natural gas price (bottom). The latter can be interpreted as a measure for the relative cost of NG vs. crude oil and shows a significant benefit for the US hub in recent years. The dashed lines are the respective linear regressions for the European hubs indicating a smaller upwards trend for these markets, too. (cif = cost+insurance+freight (average prices)). [data adapted from BP Statistical Review of World Energy, June 2013]

value-added chemical products are of key significance for this process.

Another motivation in the conversions of methane lies in the fact that many natural gas sites are located in remote areas or off-shore. Due to the low energy-density of methane and because pipelines or liquefaction facilities are costly transportation becomes uneconomical. Although prohibited in many countries, flaring of natural gas, which is dissolved in crude oil, is still a wide-spread routine, even though CO_2 released into the atmosphere has a smaller global warming impact than methane. Given this wasteful conduct, economical on-site processing might encourage utilization, increase profit and help saving resources [2]. Besides, methane may be produced from fermentation of organic material and might thus contribute to the development of a sustainable carbon-neutral society.

In order to illustrate the profitability of natural gas conversion, ethylene production will serve as an example for a brief economic consideration. Light olefins, such as ethylene and propylene, are essential industrial compounds and constitute precursors for various industrial and consumer goods in the form of plastics, fibers and other chemicals. In Europe ethylene is predominantly produced by steam cracking of naphtha [3] and in turn pricing is strongly dependent on crude oil supply. In Summer 2013 ethylene spot prices amounted to roughly 1000 EUR/mt FD NWE (free delivered northwest Europe). Direct conversion of natural gas by oxidative coupling of methane (OCM) is a potential direct production route for ethylene. The natural gas price in Europe recently amounts to ~ 10 U.S. dollar/million Btu (approx. 7.5 Euros/28 m^3) according to Figure 1.1. Assuming a 30 % yield one can roughly estimate that ethylene pricing is of the same order of magnitude (i.e. 1500 EUR per metric ton) as ethylene extraction from

crude oil. However, with respect to gas prices in the US we find an ethylene price of only 500 EUR per metric ton. Though this rough estimate does not take into consideration investment costs and running expenses, it shows that methane conversion might become a competitive process to conventional production. As a second example for the economic, political and geostategical interests in methane conversion serves the construction of the Pearl GTL plant in Qatar by Shell and Qatar petroleum. The plant has reached full production capacity in the last year and is the world's largest gas-to-liquids plant based on methane-to-olefins conversion via Fischer-Tropsch sythesis.

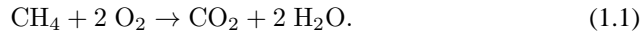
In spite of all economic and ecologic incentives for conversion of natural gas to higher-value chemical products, nowadays, natural gas is still predominately burned for heating and electricity generation purposes [4]. Combustion chemistry is a vivid research field and although combustion science may be considered a traditional and mature research field, methane oxidation is still of great importance for the design of e.g. domestic boilers and modern power plant gas turbines. The two research fields, combustion science and chemical synthesis, rely on the same governing chemo-physical principles, and therefore it is natural to approach the topic in this perspective and to tackle it with the experience and concepts of both disciplines.

1.2 Methane Oxidation Processes

Oxidative methane conversion can be categorized by the stoichiometry of the reactants, i.e. in terms of the methane-to-oxygen ratio CH_4/O_2 or likewise in terms of the equivalence ratio ϕ which is commonly used in the combustion community and defined as the ratio of the methane-to-oxygen ratio to the stoichiometric methane-to-oxygen ratio, i.e. $\phi = (\text{CH}_4/\text{O}_2) / (\text{CH}_4/\text{O}_2)_{\text{st}}$. Oxygen-rich stoichiometries ($\text{CH}_4/\text{O}_2 \leq 0.5$ or $\phi \leq 1$) are characteristic for combustion systems. In chemical synthesis methane-rich stoichiometries are employed up to the point of pyrolysis ($\text{CH}_4/\text{O}_2 \gg 1$ or $\phi \gg 2$). Table 1.1 summarizes oxidative as well as pyrolytic methane reactions with their reaction energies and entropies.

1.2.1 Methane Combustion

The products of methane combustion are carbon dioxide and water



In contrast to chemical processes, air is generally used as oxidizer in combustion processes which brings nitrogen chemistry into play. Despite the loss in efficiency modern gas turbines are generally operated with excess oxygen (lean operation mode) in order to ensure complete combustion on the one hand, and to decrease the maximum temperature on the other. The efficiency of an idealized gas turbine is thermodynamically given by

$$\eta_{\text{th}} = \frac{(T_2/T_0)(1 - \Lambda^{-\eta_{\text{T}}}) - (\Lambda^{1/\eta_{\text{C}}} - 1)}{(T_2/T_0) - \Lambda^{1/\eta_{\text{C}}}} \quad (1.2)$$

where T_0 is the ambient temperature, T_2 the turbine entrance temperature, $\Lambda(p/p_0)$ is a function of the compression ratio, η_{T} and η_{C} are the polytropic efficiencies of turbine and compressor, respectively (each can be assumed to be constants of approximately 0.9) [6]. It can be shown that, for a given compression ratio p/p_0 , the efficiency increases with the turbine entrance temperature T_2 which is given by the combustion

Reaction	$\Delta_r H^0$	$\Delta_r S^0$	$\Delta_r G^0$
$\text{CH}_4 \rightarrow 1/2 \text{C}_2\text{H}_6 + 1/2 \text{H}_2$	33	-6	35
$\text{CH}_4 \rightarrow \text{C(s)} + 2 \text{H}_2$	75	81	51
$\text{CH}_4 \rightarrow 1/2 \text{C}_2\text{H}_2 + 3/2 \text{H}_2$	189	110	156
$\text{CH}_4 + 2 \text{O}_2 \rightarrow \text{CO}_2 + 2 \text{H}_2\text{O(g)}$	-802	-5	-801
$\text{CH}_4 + 3/2 \text{O}_2 \rightarrow \text{CO} + 2 \text{H}_2\text{O(g)}$	-519	81	-544
$\text{CH}_4 + 1 \text{O}_2 \rightarrow \text{CO}_2 + 2 \text{H}_2$	-319	84	-344
$\text{CH}_4 + \text{O}_2 \rightarrow \text{CH}_2\text{O} + \text{H}_2\text{O(g)}$	-283	16	-288
$\text{CH}_4 + 3/4 \text{O}_2 \rightarrow 1/6 \text{C}_6\text{H}_6 + 3/2 \text{H}_2\text{O(g)}$	-274	-12	-271
$\text{CH}_4 + 3/4 \text{O}_2 \rightarrow 1/2 \text{C}_2\text{H}_2 + 3/2 \text{H}_2\text{O(g)}$	-174	44	-187
$\text{CH}_4 + 1/2 \text{O}_2 \rightarrow 1/2 \text{C}_2\text{H}_4 + \text{H}_2\text{O(g)}$	-141	10	-144
$\text{CH}_4 + 1/2 \text{O}_2 \rightarrow \text{CH}_3\text{OH(g)}$	-126	-49	-112
$\text{CH}_4 + 1/2 \text{O}_2 \rightarrow \text{CO} + 2 \text{H}_2$	-36	170	-87
$\text{CH}_4 + 1/4 \text{O}_2 \rightarrow 1/2 \text{C}_2\text{H}_6 + 1/2 \text{H}_2\text{O(g)}$	-88	-28	-80

Table 1.1: Overview of pyrolytic and oxidative methane conversion reactions (in kJ/mol and J/mol K, respectively at 300 K, thermodynamic parameters taken from [5]).

temperature. Therefore a maximum combustion temperature is aspired. However, there are two reason why this is impractical. (i) The rotor blades of the turbine's first stage at the outlet of the combustion chamber only resist a certain thermal load. Thanks to dedicated materials and internal blade cooling maximum temperatures of ~ 1700 K may be achieved in modern systems, though adiabatic flame temperature of methane-air amount to ~ 2200 K. (ii) Nitric oxides NO_x emissions are hold responsible since they lead to formation of acid rains and smog. However, NO concentrations depend on temperature exponentially and at temperatures characteristic for fuel combustion (1800 K and higher) the equilibrium NO concentrations exceeds 1500 ppm [7]. This process is known as thermal NO formation or Zeldovich mechanism:

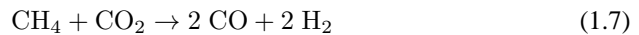
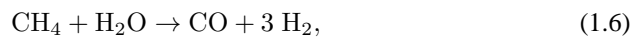


1.2.2 Chemical Synthesis

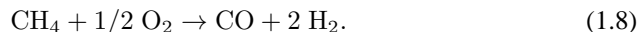
Chemical synthesis processes may generally be categorized into indirect and direct methods (e.g. [8, 9]).

Indirect Conversion

The indirect conversion route begins with synthesis gas (syngas) production by highly endothermic steam (or less often CO_2) reforming



or, alternatively, through exothermic partial oxidation



The H_2/CO ratio required for subsequent processing can be adjusted by the water gas-shift reaction



may be further converted in gas-to-liquid processes, like the Fischer–Tropsch synthesis or the Mobil process for liquid hydrocarbons generation, just to name some examples for syngas processing [10, 11, 2]. Alternatively, direct conversion routes would generally avoid the cost-intensive syngas generation step which amounts to 60-70 % of the cost of the overall process [12, 13].

Direct Conversion

Examples for direct conversion processes include pyrolysis (i.e. thermal coupling) and partial oxidation or oxidative coupling. While the desired product in partial oxidation is commonly methanol, here we will restrict our attention to oxidative coupling to C2 products. It is convenient to first look at thermodynamic considerations for pyrolysis of methane, and subsequently, discuss the oxidative process with respect to the formation of coupling products.

Pyrolysis Pyrolysis is the transformation of organic materials by heat in the absence of oxygen. It is an endothermic process and one general problem in pyrolytic coupling of methane is the fact that the C-C bond of the desirable coupling product ($\text{H}_3\text{C}-\text{CH}_3 \rightarrow 2 \text{CH}_3$, $\Delta_r H^0(298 \text{ K}) = 377 \text{ kJ/mol}$) is weaker than the C-H bond in the educt ($\text{H}-\text{CH}_3 \rightarrow \text{H} + \text{CH}_3$, $\Delta_r H^0(298 \text{ K}) = 439 \text{ kJ/mol}$) which poses an inherent thermodynamic handicap to the process [14]. The Gibbs free energy of formation can be interpreted as the physical concept underlying chemical intuition. The red curves in Figure 1.2 show the Gibbs free energies of formation $\Delta_f G^0$ per C atom for a number of hydrocarbons as a function of temperature. Given an initial ensemble of CH_4 molecules the Gibbs energy of formation $\Delta_f G^0$ of each hydrocarbon molecule reflects its relative stability with respect to its constituents and other hydrocarbon species, e.g. the formation of a C2 species is favorable if its Gibbs free energy is smaller than that of two methane molecules. It can be seen that methane constitutes the most stable hydrocarbon up to 1300 K. At higher temperatures benzene, and subsequently above 1700 K acetylene becomes the most stable hydrocarbon. However, at the same time the decomposition into molecular hydrogen and carbon is encouraged for temperatures greater than 800 K. Only for temperatures in excess of 4200 K acetylene is even more stable than the elemental species due to its negative slope. The resulting equilibrium calculations, which include constraints due to the conservation of elements, for pure methane as a function of temperature are shown in Figure 1.3. The highest acetylene yield is achieved above 1500 K. However, as noted before at these temperatures acetylene is less stable than C(s) and H_2 and therefore decomposition has to be overcome by quenching the reaction, i.e. short residence times on the order of 0.1–10 ms [15].

Oxidative Coupling By adding oxygen to the system the process becomes exergonic, i.e. the energy of the endothermic thermal coupling ($\text{CH}_4 \rightarrow 1/2 \text{C}_2\text{H}_6 + 1/2 \text{H}_2$, $\Delta_r G^0 = 36 \text{ kJ/mol}$ at 1000 K) is provided by binding the liberated hydrogen ($\text{CH}_4 + 1/4 \text{O}_2 \rightarrow$

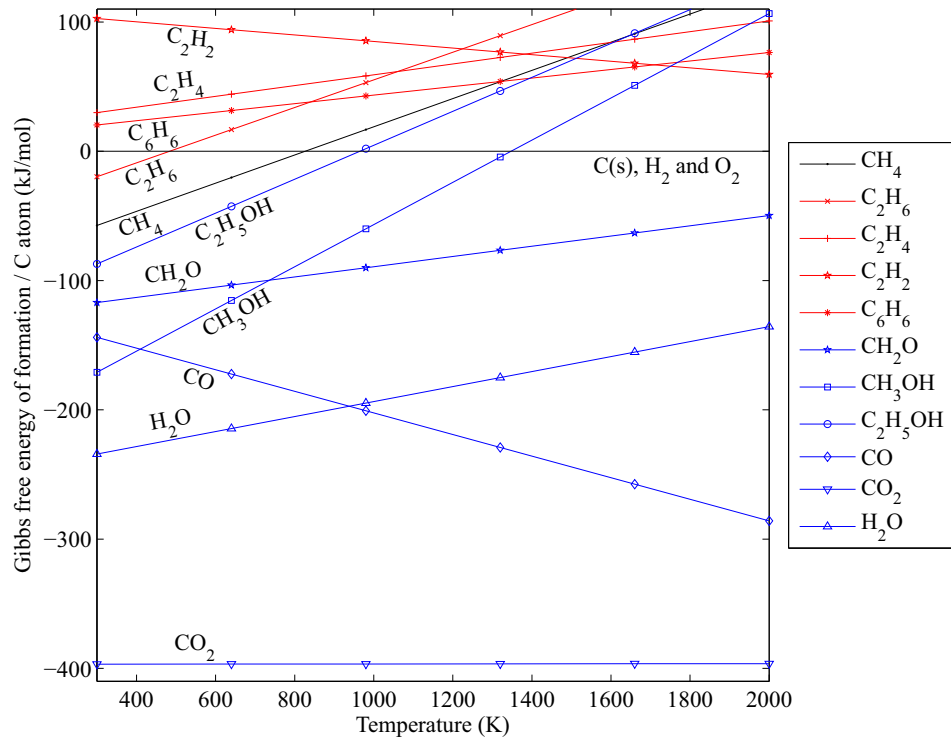


Figure 1.2: Gibbs energies of formation $\Delta_f G^0$ (per carbon atom) of hydrocarbons and water as a function of temperature. Red graphs refer to the pyrolysis process, while the blue graphs correspond to additional oxygenate products. The Gibbs energy of formation $\Delta_f G^0$ of each hydrocarbon molecule reflects its relative stability in terms of its elements with respect to another hydrocarbon molecule. At a given temperature, the most stable compound corresponds to the lowest Gibbs energy of formation (calculated from CHEMKIN thermodynamic database).

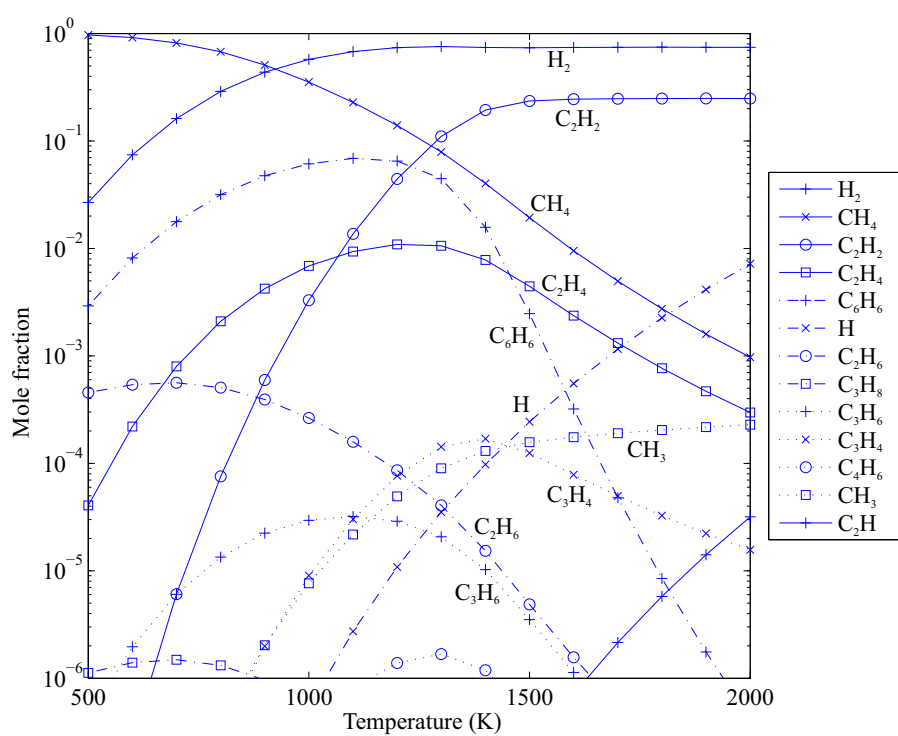


Figure 1.3: Equilibrium composition of methane pyrolysis at atmospheric pressure (calculated for constant pressure and temperature using CHEMKIN thermodynamic database, excluding C(s)).

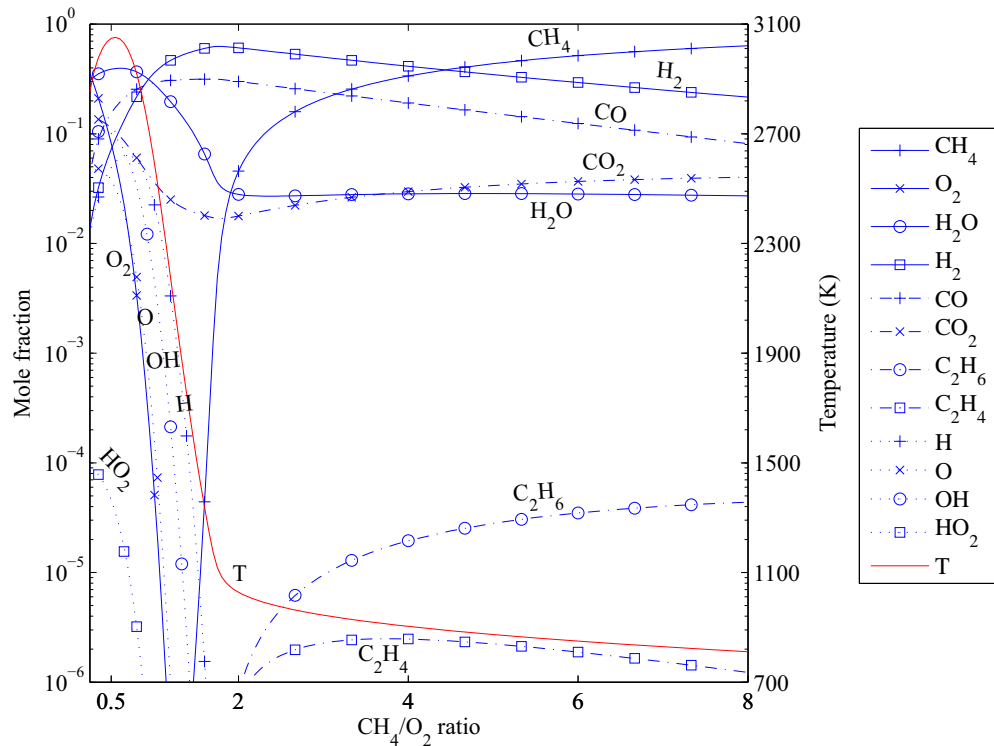


Figure 1.4: Equilibrium composition and temperature as a function of CH_4/O_2 ratio at atmospheric pressure (calculated for constant pressure and enthalpy using CHEMKIN thermodynamic database, excluding C(s)).

$1/2 \text{C}_2\text{H}_6 + 1/2 \text{H}_2\text{O}$, $\Delta_r G^0 = -60 \text{ kJ/mol}$ at 1000 K). This is also seen from Figure 1.2, now also taking into account the oxygen containing species depicted by the blue curves. The equilibrium composition and temperature as a function of CH_4/O_2 ratio is shown in Figure 1.4. For methane/oxygen ratios close to stoichiometry ($\text{CH}_4/\text{O}_2 = 0.5$) major products include not only H_2O , CO , CO_2 and H_2 but also OH as well as H and O atoms due to the exceedingly high temperature of the undiluted mixture (3000 K)¹. Around $\text{CH}_4/\text{O}_2 = 2$ partial oxidation to syngas has high yields. Beyond the stoichiometric point the equilibrium temperature falls drastically and remains around $\sim 900 \text{ K}$ for CH_4/O_2 ratios greater than 2. CO and hydrogen are the principal products, CO_2 and water are minor products on the order of some percent and ethane and ethylene are the only higher hydrocarbons above ppm level.

In contrast to the discussion for methane pyrolysis, where thermodynamics lead a long way, the thermodynamic considerations become tedious for methane oxidation at this point. High yields for C2 species cannot be expected from a thermodynamic point of view. However, a real system involves chemical kinetics as well as transport processes which may considerably alter the product pattern. Kinetics can be influenced e.g. by the use of a catalyst, and a positive transport effect is achieved e.g. by imposing

¹Though the adiabatic flame temperature of methane-air mixtures just reaches $\sim 2200 \text{ K}$, this is still sufficiently high to produce considerable equilibrium amounts of OH radicals ($\sim 3400 \text{ ppb}$). This may explain why OH is readily detected in combustion studies.).

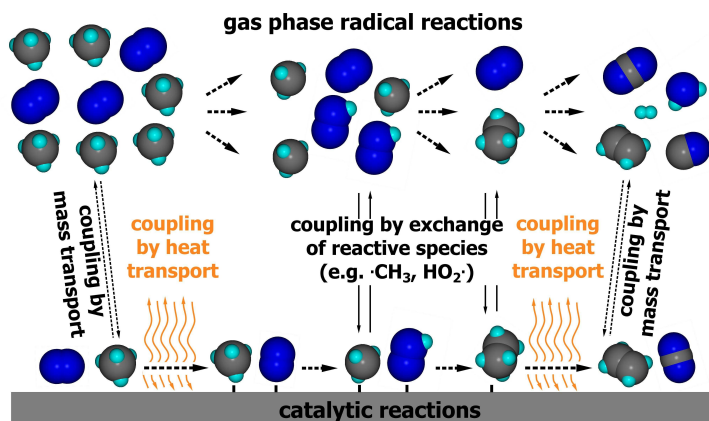


Figure 1.5: Heterogeneous-homogeneous coupling.

short contact times [16].

1.3 Homogeneous-Heterogeneous Coupling in OCM

Apart from the above general motivation, the present work is motivated by the groups' research on oxidative coupling of methane (OCM). For decades, oxidative coupling to ethylene has been a desired direct conversion route. Due to the thermodynamic limitations discussed above, it is necessary to manipulate the kinetics of the process. With this intention, research and industry have focused on the development of efficient catalysts, however yields of $\sim 30\%$ have not been overcome [17, 18]. It's noteworthy that there are reports which predict an upper bound of $\sim 30\%$ yield of a catalytic process based on thermodynamically consistent kinetics that can be incorporated into a reactor-transport model to generate yield trajectories [19]. Similar mechanistic constraints, independent of employed catalyst, were already put forward earlier [20]. It appears that the reaction proceeds via a heterogeneous-homogeneous mechanism [21]. That means that apart from the catalytic surface chemistry, gas-phase chemistry might become competitive due to initiation of gas-phase reactions (due to the high temperatures) and high rates of intermolecular collisions (due to elevated pressure under industrial operation). In addition to the catalytic and homogeneous activity, heat- and mass-transfer to and from the catalyst come into play, a process commonly referred to as homogeneous-heterogeneous coupling (Figure 1.5). The often cited mechanism by Lunsford suggests ethane is being produced mainly by the coupling of the surface-generated CH_3 radicals in the gas-phase [22]. In fact, it was shown earlier [23] and the present experiments confirm that OCM even occurs in the absence of a catalyst though a catalyst generally leads to increased selectivities. Hence it is natural to strive for a comprehensive model of homogeneous-heterogeneous dynamics comprising surface and gas-phase reactions as well as heat- and mass-transfer processes. Obviously, the model depends on an accurate kinetic mechanism to describe the gas-phase reaction network which is yet another motivation to the present kinetic studies.

1.4 Objective and Outline of the Thesis

With regard to the above motivation, the aim of this thesis is the investigation of gas-phase methane oxidation kinetics. Modeling of the extensive and complex reaction network relies on kinetic mechanisms listing Arrhenius parameters for the relevant elementary reactions. However, there are numerous mechanisms available in literature [24] and some kinetic parameters reported by different authors deviate from each other by orders of magnitude [21]. Many mechanisms originate from the combustion community (i.e. under conditions close to stoichiometry, in air-fed systems and elevated temperatures), some are optimized with respect to restricted conditions, and hence extrapolation to conditions typically found in the context of chemical synthesis may not be adequate. Throughout the thesis we will encounter three different methane-oxidation regimes: stoichiometric combustion in an open, atmospheric Bunsen-type flame, fuel-rich methane oxidation in a high-pressure flow reactor with intent to study gas-phase oxidative coupling kinetics, and catalytically assisted combustion and partial oxidation on a platinum gauze.

The thesis is based on a complementary approach, comprising experimental as well as numerical methods: (i) Since methane oxidation involves radical chain reactions, a special emphasis in this work lies on the laser-spectroscopic detection of radical species. To this effect, laser-induced fluorescence (LIF) is employed for the detection of OH hydroxy radicals, which is a species commonly interrogated using LIF in combustion science [25]. However, according to Chen et al. [21] methyl (CH_3) and hydrogen peroxy radicals (HO_2), are the most abundant radicals under conditions common to oxidative coupling (CH_4/O_2 2 - 8) and their concentrations are calculated to be on the order of 10^{-4} mol/m^3 ($\approx 1 \text{ ppm}$). Other radical concentrations are expected to be several orders of magnitude lower and therefore a major challenge lies in the required detection efficiency of the diagnostic. Another challenge is the development of a detection scheme allowing the in situ detection in a closed reactor without optical access which is accomplished by means of optical fibers. (ii) The second emphasis of the thesis lies in the kinetic modeling of the reacting flow. Based on the complete set of Navier-Stokes equations comprehensive computational fluid dynamics (CFD) simulations are performed which take into account the elementary kinetics of the system as well as heat and mass transport processes. In other cases, simplifying assumptions are made giving rise to reactor models which are computationally less expensive.

The thesis is divided into two parts: the introductory part provides the theoretical and methodological background, while in the second part the results are presented in the form of research articles which were or will be submitted to peer-reviewed scientific journals.

Introduction

Subsequent to the motivation, **Chapter 2** provides the theoretical background for the experimental and numerical methods used. Based on fundamental relations the important governing equations are developed. In **Chapter 3** some practical aspects of the experimental techniques are summarized. In particular the laser-spectroscopic methods employed throughout the work are presented.

Results

The novel fiber-optic probe enabling in situ LIF detection in harsh environment is introduced in **Chapter 4**. Detection of OH radicals is demonstrated in a stoichiometric

CH₄/air flame, which is characterized by vibrational N₂ Raman thermometry. **Chapter 5** is dedicated to the investigation of gas-phase fuel-rich methane oxidation, common to oxidative coupling conditions (CH₄/O₂ = 8), in a high-pressure flow reactor. Kinetic profiles are measured using a multi-species sampling technique as well as CH₂O detection by means of the fiber-optic LIF technique. Kinetic CFD simulation are performed and the results are compared to the experimental data. The OCM gas-phase reaction mechanism is discussed. Eventually, **Chapter 5** reports on catalytically stabilized methane oxidation on a platinum gauze which are intended to prove the feasibility of OH detection using LIF under the conditions of interest. OH radicals are readily detected under lean conditions ($\phi = 0.5$). However, in the fuel-rich regime ($\phi = 2.0$) OH concentrations are just below the detection limit which exposes the limitations of the diagnostic. Both experiments are compared to gas-phase chemistry simulations.

Chapter 2

Theoretical Background

In this chapter we will introduce governing equations which are of relevance for this work and thus lay the basis for a theoretical approach to the matters of interest.

2.1 Optics

2.1.1 Maxwell's Equations

The following section recapitulates the basics of light-matter interaction in terms of classical electrodynamics in order to summarize essential characteristics of the laser-diagnostics used in this work. Rayleigh, Raman scattering and absorption are derived from the same underlying principles of radiation-dipole interaction.

Many optical phenomena can be understood and interpreted based on Maxwell's equations [25]. Adopting the common notation by [26, 27], the differential set of Maxwell's (macroscopic) equations is:

$$\nabla \cdot \mathbf{D} = \rho \quad (2.1) \quad \nabla \cdot \mathbf{B} = 0 \quad (2.3)$$

$$\nabla \times \mathbf{E} = -\frac{\partial \mathbf{B}}{\partial t} \quad (2.2) \quad \nabla \times \mathbf{H} = \frac{\partial \mathbf{D}}{\partial t} + \mathbf{j} \quad (2.4)$$

where \mathbf{E} and \mathbf{H} denote, respectively, the electric and magnetic field. \mathbf{D} and \mathbf{B} are defined as the electric flux density (also called displacement field) and the magnetic flux density, respectively, and are specified by the electric and magnetic properties of the medium. ρ is the free (unbound) charge density and \mathbf{j} the current density.

Two more equations are required in order to solve the set of Maxwell's equations. The constitutive equations represent the electric and magnetic properties of the medium by defining the electric and magnetic flux densities \mathbf{D} and \mathbf{B} as

$$\mathbf{D} = \varepsilon_0 \mathbf{E} + \mathbf{P}(\mathbf{E}) \quad (2.5)$$

$$\mathbf{B} = \mu_0 \mathbf{H} + \mathbf{M}(\mathbf{E}) \quad (2.6)$$

While the electric permittivity ε_0 and the magnetic permeability μ_0 are natural constants, the polarization and magnetization density $\mathbf{P}(\mathbf{E})$ and $\mathbf{M}(\mathbf{H})$ are functions of \mathbf{E} and \mathbf{H} , respectively, and specify the response of the bound charges and currents to the acting fields \mathbf{E} and \mathbf{H} . In the vacuum \mathbf{P} and \mathbf{M} would vanish. Since this work focuses on non-magnetic media we assume $\mathbf{M} = 0$ and restrict our attention to the

2.1. Optics

\mathbf{P} -dependence on the electric field \mathbf{E} . However, the discussion may be assumed to be directly transferred to magnetic media. Generally, the response is non-linear and may be expressed in terms of a Taylor series

$$\mathbf{P} = \varepsilon_0 \sum_i \chi^{(i)} \mathbf{E}^i \quad (2.7)$$

where $\chi^{(i)}$ are the electric susceptibility tensors of degree $i + 1$.

In a molecular picture, a sinusoidal electric field \mathbf{E} exerts a force onto the charged particles constituting the molecule and the light electrons begin to oscillate against the heavy nuclei, creating an oscillating induced dipole. In fact, the polarization is defined as the sum over all molecular dipole moments induced by the electric field, but a molecular description of that process will be given in the next section. In most cases the charge displacement is small and it is sufficient to assume a linear response of the medium to the applied electric field \mathbf{E} , thus neglecting higher-order terms. Only if the electric field becomes sufficiently strong, i.e. comparable to atomic electric fields $\sim 10^5 - 10^8$ V/m, the non-linear terms become important. For instance, typical higher-order susceptibilities are on the order of $\chi^{(1)} \approx 1$, $\chi^{(2)} \approx 10^{-13} - 10^{-10} \frac{\text{m}}{\text{V}}$ (except for isotropic media where $\chi^{(2)}$ vanishes for reason of symmetry), $\chi^{(3)} \approx 10^{-23} - 10^{-18} \frac{\text{m}^2}{\text{V}^2}$ [28, 27].

In most cases a linear relation is sufficient, therefore higher-order terms are omitted and the constitutive equation becomes

$$\begin{aligned} \mathbf{D} &= \varepsilon_0 \mathbf{E} + \varepsilon_0 \chi^{(1)} \mathbf{E} \\ &= \varepsilon_0 (1 + \chi^{(1)}) \mathbf{E} \\ &= \varepsilon_0 \varepsilon \mathbf{E} \end{aligned} \quad (2.8)$$

where $\varepsilon = 1 + \chi^{(1)}$ is the medium's dielectric constant.

Using the above relation it is now possible to elucidate the propagation of light in matter. By taking the curl of equation (2.2) and using the vector identity $\nabla \times (\nabla \times \mathbf{E}) = \nabla(\nabla \cdot \mathbf{E}) - \nabla^2 \mathbf{E}$, we find the wave equation

$$\begin{aligned} \nabla^2 \mathbf{E} - \mu_0 \varepsilon_0 \varepsilon \frac{\partial^2 \mathbf{E}}{\partial t^2} &= 0 \\ \nabla^2 \mathbf{E} - \frac{n^2}{c^2} \frac{\partial^2 \mathbf{E}}{\partial t^2} &= 0 \end{aligned} \quad (2.9)$$

where we have used the definitions of the speed of light $c = (\mu_0 \varepsilon_0)^{-1/2}$ and (complex) refractive index $n = \sqrt{\varepsilon}$. An analogous expression is found for \mathbf{H} . Solutions of the wave equation are of the form $\mathbf{E} = \hat{\mathbf{E}}(\mathbf{x}) \exp(-i\omega t)$ and the full solution depends on individual boundary conditions.

2.1.2 Classical Approach to Light-Matter Interaction

The electric dipole moment of a molecule can be expressed in terms of the charge density $\rho(\mathbf{x}, t)$,

$$\boldsymbol{\mu} = \int \rho(\mathbf{x}, t) \mathbf{x} d^3\mathbf{x} \quad (2.10)$$

which in turn can be expressed in terms of the Dirac delta function $\delta(\mathbf{x})$, so that $\rho(\mathbf{x}, t) = \sum_i q_i \delta(\mathbf{x} - \mathbf{x}_i(t))$, where q_i is the point charge found at position $\mathbf{x}_i(t)$.

In the simplest case of say a proton and an electron separated by a distance vector \mathbf{d} , $\rho(\mathbf{x}, t) = e\delta(\mathbf{x} - \mathbf{d}/2) + (-e)\delta(\mathbf{x} + \mathbf{d}/2)$, and hence the permanent dipole is $\boldsymbol{\mu}_{\text{per}} = e\mathbf{d}$. Molecules are dynamic systems and their vibrational motion is best described in terms of the equilibrium coordinates $\boldsymbol{\varsigma}_i = \mathbf{x}_i - \mathbf{x}_{i0}$, where \mathbf{x}_{i0} are the equilibrium positions. The molecule is characterized by its $3N - 6$ normal modes (linear molecules have $3N - 5$ vibrational modes), each being associated with an eigenfrequency ω_v . As a consequence, the molecule's permanent dipole oscillates about its equilibrium value, $\boldsymbol{\mu}_{\text{per}}(t) = \bar{\boldsymbol{\mu}}_{\text{per}} + \boldsymbol{\mu}'_{\text{per}} \cos(\omega_v t)$.

An important consequence of Maxwell's equations is the fact that accelerated charges, represented by the dipole moment $\boldsymbol{\mu}$, emit electromagnetic radiation. In the far field, i.e. $r \gg \varsigma_i$, the electric field is

$$\mathbf{E} = \frac{1}{4\pi\epsilon_0 c^2} \frac{(\ddot{\boldsymbol{\mu}} \times \mathbf{e}_r) \times \mathbf{e}_r}{r}, \quad (2.11)$$

where \mathbf{e}_r is the unit vector in \mathbf{r} direction. In this classical picture, this implies that an oscillating molecule will emit at an angular frequency ω_v . Of course this picture is incomplete since we know from quantum mechanics that the vibrational modes are quantized and that a molecule can either emit or absorb radiation through transitions from one state to another. It was Planck's discovery, that the frequency of the electromagnetic wave is related to the energy carried by the photon by $h\nu = E_i - E_f$. However, it is interesting to note that this simple classical model can explain infra-red absorption of simple molecules: a molecule is infra-red active if there is a non-vanishing change of the dipole moment due to the vibrational motion, $\partial\boldsymbol{\mu}/\partial\varsigma_i|_0 \neq 0$. Generally, homonuclear diatomic molecules are not infrared-active since they do not possess a dipole moment at all, while heteronuclear diatomics and non-linear triatomic and larger molecules have infrared-active modes. A more rigorous explanation for this symmetry relations is provided by group theory. A vibrational mode is infrared-active if it has the same symmetry as a component of the dipole moment vector x, y, z . For this purpose, the symmetry properties are listed in the character tables.

Apart from the permanent dipole moment, a dipole can be induced by an incident electromagnetic field $\mathbf{E}_{\text{inc}} = \hat{\mathbf{E}}_{\text{inc}} \cos(\mathbf{k} \cdot \mathbf{x} - \omega t)$, where the wavelength $\lambda = 2\pi/|\mathbf{k}|$ is typically large compared to the characteristic size of the molecule. The polarizability tensor $\underline{\alpha}$ is the proportionality factor determining the response of the molecule in terms of the induced dipole moment $\boldsymbol{\mu}_{\text{ind}} = \underline{\alpha}\mathbf{E}_{\text{inc}}$. In other words, the nuclei are displaced from their equilibrium positions in the direction of the perturbing field \mathbf{E}_{inc} , and electrons are drawn in the opposite direction. However, according to the Born-Oppenheimer approximation the nuclei are comparably heavy it can be assumed that the displacement of the electrons is the principal source for the induced dipole moment. Every molecule has a non-zero polarizability even if it has a vanishing permanent dipole moment.

It is now of interest to examine the case when the angular frequency of the incident field ω is far from resonance, $\omega \gg \omega_v$. If we take into consideration that intramolecular forces will change if the charges are displaced from their equilibrium positions, the polarizability $\underline{\alpha}(\boldsymbol{\varsigma}_i)$ becomes a function of the coordinates $\boldsymbol{\varsigma}_i$ and as a first order estimate it can be rewritten as

$$\underline{\alpha} = \underline{\alpha}|_0 + \sum_i \nabla \underline{\alpha}|_0 \boldsymbol{\varsigma}_i. \quad (2.12)$$

For normal modes all oscillations are at the same frequency, $\boldsymbol{\varsigma}_i = \boldsymbol{\varsigma}'_i \cos(\omega_v t)$, and the

2.1. Optics

induced dipole moment of the molecule $\boldsymbol{\mu}_{ind}$ is therefore given by

$$\begin{aligned}\boldsymbol{\mu}_{ind} &= \underline{\alpha}|_0 \hat{\mathbf{E}}_{inc} \cos(\omega t) + \sum_i \nabla \underline{\alpha}|_0 \boldsymbol{\zeta}'_i \cos(\omega_v t) \hat{\mathbf{E}}_{inc} \cos(\omega t) \\ &= \underline{\alpha}|_0 \hat{\mathbf{E}}_{inc} \cos(\omega t) + \sum_i \nabla \underline{\alpha}|_0 \boldsymbol{\zeta}'_i \hat{\mathbf{E}}_{inc} (\cos((\omega_v - \omega)t) + \cos((\omega_v + \omega)t)).\end{aligned}\tag{2.13}$$

The first term in equation (2.13) is the origin of elastic Rayleigh scattering at the same frequency as the incident field, whereas the second term gives rise to the inelastic Raman effect. It comprises two Stokes shifted frequencies $\omega \pm \omega_v$ named anti-Stokes and Stokes respectively, where the less probable Stokes effect requires the molecule to be in an excited state and more energetic photons are emitted as are incident on the molecule, whereas in the other case energy is transferred to the molecule and it is left in an excited state.

Again, this classical expression is sufficient to determine whether a molecule is Raman-active. The requirement is that the change of the polarizability due to the vibrational motion is non-vanishing, $\partial\alpha/\partial\zeta_0 \neq 0$. We recall that the requirement for infra-red activity is $\partial\boldsymbol{\mu}/\partial\zeta_i|_0 \neq 0$.

2.1.3 Molecular Scattering in Gases on a Macroscopic Scale

A gas is constituted of randomly aligned molecules. The polarization is a tensor quantity and depends on the orientation of the molecule. We will account for directionality by taking the mean $\langle \dots \rangle$ over an ensemble of randomly aligned molecules. Hence the mean induced dipole moment $\langle \boldsymbol{\mu}_{ind} \rangle$ depends on the mean values $\langle \underline{\alpha}|_0 \rangle$ and $\langle \sum_i \nabla \underline{\alpha}|_0 \boldsymbol{\zeta}'_i \rangle$. For spherically symmetric molecules the former tensor $\langle \underline{\alpha}|_0 \rangle$ will be isotropic which results in scattering with the same polarization direction as the incident electromagnetic field, while in general it has to be considered to be non-isotropic. In the latter case the scattering comprises a depolarized component, i.e. perpendicular to the incident field. The depolarization ratio ρ_p represents the ratio of the parallel and perpendicular components and is of the order 10^{-2} for molecules in question in the context of this study [29]. Thus, in what follows, it is justified to consider the mean polarization $\langle \underline{\alpha}|_0 \rangle$ to be an isotropic tensor.

If one considers that the incident field is polarized along the z -axis, then so will be $\boldsymbol{\mu}_{ind}$ and the double cross product in equation (2.11) is equivalent to $\langle \ddot{\mu} \rangle \sin(\vartheta) \mathbf{e}_z$, where ϑ is the angle between the radial vector \mathbf{e}_r and the polarization axis. The resulting electric field is given by

$$\begin{aligned}\mathbf{E} &= \frac{\hat{E}_{inc}}{4\pi\epsilon_0 c^2 r} \sin(\vartheta) \left(\langle \alpha|_0 \rangle \omega^2 \cos(\omega t) + \right. \\ &\quad \left. \left\langle \sum_i \nabla \alpha|_0 \zeta'_i \right\rangle ((\omega - \omega_v)^2 \cos((\omega - \omega_v)t) + (\omega + \omega_v)^2 \cos((\omega + \omega_v)t)) \right) \mathbf{e}_z.\end{aligned}\tag{2.14}$$

It is noteworthy that the scattering signal itself is polarized in the same direction as the incident field and that it vanishes as $\sin(\vartheta) = 0$, i.e. there is no scattering in the direction of the incident field polarization.

The irradiance I in units of Wm^{-2} is found by taking the temporal integral, which yields $I = \frac{\varepsilon_0 c}{2} |\mathbf{E}'|^2$,

$$\begin{aligned} I_{\text{Ray}} &\propto \frac{1}{r^2} I_{\text{inc}} \sin^2(\vartheta) \langle \alpha|_0 \rangle^2 \omega^4 \\ I_{\text{Ram}} &\propto \frac{1}{r^2} I_{\text{inc}} \sin^2(\vartheta) \left\langle \sum_i \nabla \alpha|_0 \zeta'_i \right\rangle^2 (\omega \pm \omega_v)^4, \end{aligned} \quad (2.15)$$

for the Rayleigh scattering I_{Ray} at frequency ω and for the Raman signal I_{Ram} at Stokes shifted species specific frequencies $\omega \pm \omega_v$ respectively. The polarization term and the frequency dependence are conventionally accounted for in the cross-section σ to give $\sigma_{\text{Ray}} = \langle \alpha|_0 \rangle^2 \omega^4$ and $\sigma_{\text{Ram}} = \langle \sum_i \nabla \alpha|_0 \zeta'_i \rangle^2 (\omega \pm \omega_v)^4$.

On a macroscopic scale every molecule in the probe volume will contribute to the scattering process and the signal will be proportional to the number density n . In a gas mixture, characterized by mole fractions X_i , the effective cross section σ_{eff} is given by the mole fraction weighted average of the individual cross sections σ_i ,

$$\sigma_{\text{eff}} = \sum_i \sigma_i X_i. \quad (2.16)$$

It is convenient to express the signal strength in terms of power per solid angle

$$\frac{dP}{d\Omega} = \frac{IdA}{d\Omega} = Ir^2, \quad (2.17)$$

which we will denote by I_Ω , and we can write the final equation as

$$I_\Omega = I_{\text{inc}} \sin^2(\vartheta) n \sigma_{\text{eff}}. \quad (2.18)$$

2.1.4 Absorption and Emission of Radiation

The above classical derivation gives a qualitative picture for dipole radiation processes but fails to provide a complete model for the dipole transitions and their intensities. Again, the electric dipole is key to understand this, but now in the framework of quantum mechanics. The electric transition dipole moment between states i to j is given by:

$$\mu_{ij} := \int \Psi_i^* \hat{\boldsymbol{\mu}} \Psi_j d^3\mathbf{x} = \langle \Psi_i | \hat{\boldsymbol{\mu}} | \Psi_j \rangle \quad (2.19)$$

where $\Psi_i = \psi(\mathbf{x}) \exp(-iE_i t/\hbar)$ denotes the time-dependent wave function, $\psi(\mathbf{x})$ the stationary wave function, $\hat{\boldsymbol{\mu}} = \sum_n q_n \mathbf{x}_n$ the electric dipole moment operator and $\langle \dots \rangle$ the common bra-ket notation. For $i = j$ the time-dependence cancels and due to the symmetry of the integrand the transition moment vanishes. In contrast to the classical model, in quantum mechanics there is no static or oscillating dipole moment and therefore no radiative exchange of energy is possible. If $i \neq j$ the time-dependent terms yield $\exp(-i(E_i - E_j)t/\hbar)$ so that now there is a oscillating dipole moment of frequency $\omega = (E_i - E_j)/\hbar$. In this way the Planck relation is recovered.

The probability of a transition between two states i and j is proportional to the square of the transition dipole moment

$$M_{ij} = \left| \int \psi_i^* \hat{\boldsymbol{\mu}} \psi_j d^3\mathbf{x} \right|^2. \quad (2.20)$$

For vanishing M_{ij} the transition is said to be forbidden, which leads to the definition of selection rules. The transition moment can be separated in an electronic, vibrational and rotational parts. Each contribution can be analyzed individually resulting in distinct selection rules for electronic, vibrational and rotational transitions. For brevity we will not go further into this discussion, Herzberg [30, 31] and many other references provide detailed derivations for selection rules and list transition energies and intensities of various molecular systems.

2.2 Statistical Thermodynamics

The approach of this section is inspired by reference [32]. The ultimate goal of the first subsection is to derive an expression for the population distribution of a system in thermodynamic equilibrium, i.e. the partition function. The molecular partition functions are important to interpret molecular spectra. Moreover, they can also be used to arrive at a reaction rate expression similar to the Arrhenius equation based on transition state theory.

2.2.1 Derivation of Partition Function

After Boltzmann, the macroscopic entropy of a thermodynamic system S is related to the probabilities of the possible microstates p_i through the relation:

$$S = -k_B \sum_i p_i \ln p_i. \quad (2.21)$$

This relation links the experimental (observable) entropy to the states of the molecules constituting the gas (or any other collection of independent particles be it atoms or electrons in a free electron gas) on account of their microscopic properties. The thermodynamic equilibrium postulate attributes an equal probability to each accessible microstates of an isolated system, i.e. $p_i = 1/\Omega$ with $\Omega = \Omega(U, N, V)$ being the number of microstates consistent with the given macroscopic boundary conditions (U, N, V) . Such a system is called microcanonical and simple algebraic transformations yields the equation in the form in which it is engraved into Boltzmann's tombstone

$$S(U, N, V) = k_B \ln \Omega(U, N, V). \quad (2.22)$$

The canonical ensemble describes a closed system S with indefinite energy but in thermal equilibrium with a reservoir \mathcal{R} . This implies that the system sustains its temperature T by exchange of energy with the reservoir and that its temperature is given by the reservoir's temperature. The reservoir \mathcal{R} itself is supposed to be much larger than the canonical system S (and therefore has an energy which remains essentially unaffected from any changes of the energy of S). It is crucial to note that the total system consisting of reservoir \mathcal{R} and subsystem S constitutes a microcanonical system to which the postulate of equal probability applies again.

We would like to know the probability $f(E)$ of finding the canonical subsystem S in a microstate of energy E_i under the constraint of a given energy $U_{\text{tot}} = U_{\mathcal{R}} + E_i$ of the total system¹, which can be expressed in terms of the number of states of the

¹A simple analogy is instructive. Consider a set of three dice, one of which is red, the remaining two being white. The three dice have been thrown many thousand times. Whenever the sum of the numbers on the three dice has been 12 (and only then), the number on the red die has been recorded. The red die is the

reservoir having an energy $U_{\text{tot}} - E_i$ (see e.g. [33])

$$f(E) = \frac{\Omega_{\mathcal{R}}(U_{\text{tot}} - E)}{\Omega_{\text{tot}}(U_{\text{tot}})}. \quad (2.23)$$

Since the expressions in the numerator and denominator are related to the reservoir \mathcal{R} and total system, respectively, they can be expressed in terms of the entropies (equation (2.22))

$$f_i = \frac{\exp(S_{\mathcal{R}}(U_{\text{tot}} - E_i)/k_B)}{\exp(S_{\text{tot}}(U_{\text{tot}})/k_B)}. \quad (2.24)$$

At this point we will need another important law of thermodynamics which is the Gibb's fundamental equation

$$dU(S, V, N) = TdS - pdV + \mu dN \quad (2.25)$$

where U is a function of the independent extensive quantities S, V, N and we have employed the definitions of the intensive quantities temperature $T = \partial U / \partial S$, pressure $p = -\partial U / \partial V$, and chemical potential $\mu = \partial U / \partial N$. We note that $S_{\text{tot}}(U_{\text{tot}}) = S_{\mathcal{R}}(U_{\text{tot}} - U) + S_S(U)$ where U is the average energy of the canonical system \mathcal{S} . We note further that $S_{\mathcal{R}}$ can be expanded around $U_{\text{tot}} - U$, we obtain:

$$S_{\mathcal{R}}(U_{\text{tot}} - E_i) = S_{\mathcal{R}}(U_{\text{tot}} - U + U - E_i) \quad (2.26)$$

$$= S_{\mathcal{R}}(U_{\text{tot}} - U) + \frac{U - E_i}{T} \quad (2.27)$$

where we have used the equation 2.25, $dS = dU/T|_{V,N}$. Resubstituting into equation 2.24 yields

$$f(E_i) = \exp\left(\frac{U - TS}{k_B T}\right) \exp\left(\frac{-E_i}{k_B T}\right). \quad (2.28)$$

Without elaborating on the recovered expression $F = U - TS$ known as the Helmholtz potential, we observe that $\exp(U - TS/k_B T)$ is independent of E_i and can be interpreted as a normalization term when summing over all states

$$\sum_i f_i = \exp\left(\frac{F}{k_B T}\right) \sum_i \exp\left(\frac{-E_i}{k_B T}\right) = 1 \quad (2.29)$$

$$\Rightarrow Z(T) := \exp\left(\frac{-F}{k_B T}\right) = \sum_i \exp\left(\frac{-E_i}{k_B T}\right). \quad (2.30)$$

This expression is the canonical partition function denoted by $Z(T)$ which can be evaluated in terms of the microscopic properties of the system given by all states i of energy E_i . The molecular partition functions of common molecular models are summarized in table 2.1.

The partition function can be interpreted in several ways. On the one hand, the partition function is a measure of the number of thermally accessible energy states, i.e. if the temperature increases the particles can more easily access higher energy levels. E.g. a partition function of order unity dictates that essentially all particles reside in the

analogue of our system of interest, the white dice correspond to the reservoir, the numbers shown correspond to the energies of the respective systems, and the restriction to throws in which the sum is 12 corresponds to the constancy of the energy of the total system. [33, p. 349]

2.2. Statistical Thermodynamics

System	Energy	Partition function
Translation of particle of mass m confined to a volume V	$E_{\text{trans}} = \frac{p^2}{2m} = \frac{\hbar k^2}{2m}$	$Z_{\text{trans}}(T) = \frac{(2\pi m k_B T)^{3/2} V}{h^3}$
Rotation of rigid linear molecule with rotational constant B	$E_{\text{rot}} = hc B J(J+1)$	$Z_{\text{rot}}(T) = \frac{k_B T}{hc B}$
Rotation of rigid spherical top molecule with rotational constant B	$E_{\text{rot}} = hc B J(J+1)$	$Z_{\text{rot}}(T) = \sqrt{\pi \left(\frac{k_B T}{hc B}\right)^3}$
Rotation of rigid symmetric top molecule with rotational constants B and A	$E_{\text{rot}} = hc B J(J+1) + (A - B) K^2$	$Z_{\text{rot}}(T) = \sqrt{\frac{\pi}{B^2 A}} \left(\frac{k_B T}{hc}\right)^3$
Vibration of molecule with i vibrational degrees of freedom with eigenfrequencies ω_i	$E_{\text{vib}} = \hbar \omega_i (v + \frac{1}{2})$	$Z_{\text{vib}}(T) = \prod_i \left(1 - e^{-\frac{\hbar \omega_i}{k_B T}}\right)^{-1}$
Electronic excitation with first excited state's energy $E \gg k_B T$	$E_{\text{el}}(\text{ground state}) = 0,$ $E_{\text{el}}(\text{excited states}) \gg k_B T$	$Z_{\text{el}}(T) = g_{\text{el}}$ (g_{el} degeneracy of ground state)

Table 2.1: Molecular energy terms and partition functions (adapted from [32] with energy terms and partition functions according to [30]).

ground state. More precisely, the Boltzmann distribution prescribed by equation (2.28) defines the temperature in terms of the molecular population distribution and hence provides the basis for laser thermometry. On the other hand, it is possible to derive all macroscopic properties of a system based on the knowledge of the system's partition function. E.g. it follows by definition from (2.30) that $F = -k_B T \ln Z$, and the average energy $U = \langle E \rangle$ of an ensemble is found by writing

$$\begin{aligned} \langle E \rangle &= \sum_i E_i f(E_i) = \sum_i E_i \frac{\exp(-\beta E_i)}{Z} = -\frac{1}{Z} \sum_i \frac{\partial}{\partial \beta} \exp(-\beta E_i) \\ &= -\frac{1}{Z} \frac{\partial Z}{\partial \beta} = -\frac{\partial \ln Z}{\partial \beta}. \end{aligned} \quad (2.31)$$

where we have introduced the thermodynamic beta $\beta = 1/(k_B T)$.

2.2.2 Transition State Theory

In a nutshell, transition state theory allows to obtain the reaction rate constant k from the molecular properties of the reactants and the corresponding transition state complex [32]. The so-called activated complex is supposed to be in quasi-equilibrium with the reactants and once the transition state is reached it is assumed that the product is formed



The molecular partition functions are key to calculating the reaction rate constants based on the above assumption and it was Eyring [34] who first formulated a relation for the bimolecular reaction rate constant

$$k = \kappa \frac{Z^\ddagger}{Z_A Z_B} \frac{k_B T}{h} \exp\left(\frac{-E^\ddagger}{k_B T}\right) \quad (2.33)$$

where κ is the transmission coefficient, and E^\ddagger the difference in energy between the initial substances and the activated state at the absolute zero. He also commented on the resemblance to Arrhenius' equation introduced in a rather phenomenological fashion already in 1889 [35]. Since the transition complexes are known only for a number of relatively simple reactions, kinetic mechanisms still rely to a large extent on experimentally determined expressions for the rate constants, but there is a growing number of reactions that have also been evaluated on the basis of transition state theory. However, literature mechanisms are commonly provided in terms of the modified Arrhenius equation

$$k = A T^\beta \exp\left(\frac{-E_a}{k_B T}\right) \quad (2.34)$$

where the pre-exponential factor A , the temperature exponent β and the activation energy E_a are specified as kinetic parameters.

2.3 Conservation Equations

2.3.1 General Formulation of Conservation Equations

It is possible to derive a general conservation equation for a conserved quantity. Let's consider an identifiable material element of fixed mass and let Φ be a conserved property of it, then the corresponding intensive quantity φ is defined by

$$\Phi = \int_V \varphi dm = \int_V \varphi \rho dV \quad (2.35)$$

where ρ is the material's density. The material change $D\Phi/Dt$ has to equal all sources and sinks which we will denote by S_Φ . Reynolds' transport theorem [36, Art. 14; 37] states that the material change of a (tensor) property Φ may be expressed in terms of the temporal change of Φ within the occupied volume and the net flux of Φ through the volume's boundary ∂V

$$\frac{D\Phi}{Dt} = \int_V \frac{\partial \varphi \rho}{\partial t} dV + \int_{\partial V} \varphi \rho \mathbf{u}_S \cdot \mathbf{n}_S dS \quad (2.36)$$

where \mathbf{u}_S is generally the velocity of the boundary surface ∂V but since we are considering a material element it is equal to the material's velocity \mathbf{u} at the boundary. \mathbf{n}_S is the outward-directed normal vector of the surface element dS . By applying Gauss' divergence theorem

$$\int_V \nabla \cdot \mathbf{f} dV = \int_{\partial V} \mathbf{f} \cdot \mathbf{n}_S dS \quad (2.37)$$

to the last term of equation (2.36), it can be translated to a single volume integral

$$\frac{D\Phi}{Dt} = \int_V \left(\frac{\partial \varphi \rho}{\partial t} + \nabla \cdot \varphi \rho \mathbf{u} \right) dV. \quad (2.38)$$

2.3. Conservation Equations

The most simple interpretation of the above result is the continuity equation arising from the conservation of mass. The conserved quantity is the mass m and therefore $\varphi = 1$. Since there are no mass source terms ($S_\Phi = 0$) $Dm/Dt = 0$ and we obtain

$$\int_V \left(\frac{\partial \rho}{\partial t} + \nabla \cdot \rho \mathbf{u} \right) dV = 0. \quad (2.39)$$

which has to be true for any volume V . Hence the integrand itself has to be zero and we retain the continuity equation

$$\frac{\partial \rho}{\partial t} + \nabla \cdot \rho \mathbf{u} = 0. \quad (2.40)$$

Generally, the source term S_Φ can be broken up in two parts, one representing volumetric sources s_φ^{vol} , the other corresponding to surface sources s_φ^{surf} ,

$$S_\Phi = \int_V s_\varphi^{\text{vol}} dV + \int_{\partial V} s_\varphi^{\text{surf}} \cdot \mathbf{n}_S dS \quad (2.41)$$

Depending on the conserved quantity, examples for the volumetric source term are gravity and heat release due to chemical reactions. Examples for surface source terms include the pressure gradient or diffusion effects such as viscous stress or heat diffusion. Again, by applying the Gauss' theorem the surface integrals can be expressed in terms of a volumetric integral. Diffusion terms are of particular importance, since they introduce the second order derivatives into the conservation equations. In the end, a generalized conservation equation of the form

$$\frac{\partial \rho \varphi}{\partial t} + \nabla \cdot \rho \mathbf{u} \varphi = \Gamma \nabla^2 \varphi + s_\phi \quad (2.42)$$

can be formulated, where Γ is the general diffusion coefficient. In a reacting fluid the conserved quantities are mass m , momentum $m\mathbf{u}$, energy E , and the mass of each species m_i . Table 2.2 lists the $5 + N$ conservation equations. Including a constitutive equation such as the ideal gas law, there are $6 + N$ equations to solve for all unknowns.

It is noteworthy that the left hand side of the conservation equation is often written in a similar, and in fact, identical form. The density ρ then appears in front of the material derivative. By employing the chain rule and using the mass conservation equation it can be shown that

$$\begin{aligned} & \frac{\partial \rho \varphi}{\partial t} + \nabla \cdot \rho \mathbf{u} \varphi \\ &= \rho \frac{\partial \varphi}{\partial t} + \varphi \frac{\partial \rho}{\partial t} + \rho \mathbf{u} \cdot \nabla \varphi + \varphi \nabla \cdot \rho \mathbf{u} \\ &= \rho \frac{\partial \varphi}{\partial t} + \rho \mathbf{u} \cdot \nabla \varphi + \varphi \left(\frac{\partial \rho}{\partial t} + \nabla \cdot \rho \mathbf{u} \right) \\ &= \rho \left(\frac{\partial \varphi}{\partial t} + \mathbf{u} \cdot \nabla \varphi \right). \end{aligned} \quad (2.43)$$

Conserved quantity	Conservation equation	Unknowns	Number of equations
m	$\frac{\partial \rho}{\partial t} + (\nabla \cdot \mathbf{u})\rho = 0$	ρ	1
$m\mathbf{u}$	$\frac{\partial \rho \mathbf{u}}{\partial t} + (\nabla \cdot \mathbf{u})\rho \mathbf{u} = \mu \nabla^2 \mathbf{u} - \nabla p$	\mathbf{u}, p	3
E	$\frac{\partial \rho c_v T}{\partial t} + (\nabla \cdot \mathbf{u})\rho c_v T = \lambda \nabla^2 T + s_e$	T	1
m_i	$\frac{\partial \rho Y_i}{\partial t} + (\nabla \cdot \mathbf{u})\rho Y_i = -\rho D_i \nabla^2 Y_i + s_i$	Y_1, \dots, Y_N	N
ideal gas law	$p = \rho R T$		1

Table 2.2: Conservation equations and constitutive equation for a reacting fluid. The conserved quantities are mass m , momentum $m\mathbf{u}$, energy E , and species' mass $m_i, i = 1, \dots, N$. Note that the additional constraint $\sum_i^N Y_i = 1$ can be used to cut down the number of species conservation equations to $N - 1$ by stating $Y_N = 1 - \sum_i^{N-1} Y_i$.

In many cases it is convenient to reduce the order of the differential equations which greatly simplifies the solution. By writing the equations in a non-dimensional fashion it is possible to obtain dimensionless numbers which compare the magnitude of the diffusive term to the convective term. For the three conservation equations for momentum, energy and species' mass the respective dimensionless numbers are the Reynolds number

$$Re := \frac{\rho u L}{\mu}, \quad (2.44)$$

the Péclet number for heat transport

$$Pe_T := \frac{u \rho c_p L}{\lambda}, \quad (2.45)$$

and the Péclet number for mass transport for each species

$$Pe_{m_i} := \frac{u L}{D_i}. \quad (2.46)$$

Here L is the characteristic length scale, μ the dynamic viscosity, c_p the heat capacity at constant pressure, λ the thermal conductivity, and D_i the diffusion coefficient of species i . In case the diffusive term is much smaller than the convective term, i.e. the dimensionless numbers are much larger than unity, it is permissible to neglect the second order derivative and the differential equation becomes first order. Yet another important simplification are the boundary layer equations inspired by the Prandtl's observation that high Reynolds number flows can be divided into two domains, one of which is the outer flow which is considered inviscid, and the other is the thin layer close to the wall where viscous effects are pronounced and viscosity can not be neglected, that is the boundary layer [38]. In the boundary layer the above simplification applies only with respect to certain directions. Notably, this changes the characteristic of the partial differential equations from elliptic to parabolic, which has substantial implications for numerical solution. In respect to chemically reacting flows in a tubular reactor, which is of interest in this thesis, this has been implemented in the software package CHEMKIN as the Cylindrical Shear-Flow Reactor (CSFR) model [39].

2.3.2 Numerical Solution

Computational fluid dynamics (CFD) is concerned with the numerical solution of the conservation equations. Here I would like to give a concise overview of the procedure. In order to solve the conservation equations numerically they need to be discretized. For sake of simplicity let's look at the general conservation equation in Cartesian coordinates and one dimension

$$\frac{\partial \varphi}{\partial t} + u \frac{\partial \varphi}{\partial x} = \frac{\Gamma}{\rho} \frac{\partial^2 \varphi}{\partial x^2}. \quad (2.47)$$

One way to achieve a *temporal* discretization at a fixed point in space is the Euler forward method

$$\frac{\partial \varphi}{\partial t} = \frac{\varphi^{i+1} - \varphi^i}{\Delta t} \quad (2.48)$$

$$\Rightarrow \varphi^{i+1} = \varphi^i + \Delta t \frac{\partial \varphi}{\partial t} \quad (2.49)$$

$$\varphi^{i+1} = \varphi^i + \Delta t \left(\frac{\Gamma}{\rho} \frac{\partial^2 \varphi}{\partial x^2} - u \frac{\partial \varphi}{\partial x} \right) \quad (2.50)$$

where the subscript i represents the time step. A solution is obtained through iteration until a steady state solution $\partial \varphi / \partial t \rightarrow 0$ is achieved, i.e. the residual vanishes $\varphi^{i+1} - \varphi^i \rightarrow 0$. The aim of *spatial* discretization is to express the spatial derivatives $\partial \varphi / \partial x$ and $\partial^2 \varphi / \partial x^2$ as functions of the adjacent nodes $\varphi_x, \varphi_{x\pm 1}, \varphi_{x\pm 2}, \dots$, e.g. one could apply the so-called first-order upwind approximation:

$$\left. \frac{\partial \varphi}{\partial x} \right|_x = \frac{\varphi_x - \varphi_{x-1}}{\Delta x} + O(\Delta x^1). \quad (2.51)$$

Applied to equation (2.50) and neglecting the diffusion term, we obtain an arithmetic expression for the next time-step $i + 1$

$$\varphi_x^{i+1} = \varphi_x^i + \Delta t u \frac{\varphi_x^i - \varphi_{x-1}^i}{\Delta x} \quad (2.52)$$

$$= \varphi_x^i + \frac{\Delta t u}{\Delta x} (\varphi_x^i - \varphi_{x-1}^i) \quad (2.53)$$

where the Courant-Friedrich-Lewy (CFL) number is defined as $\text{CFL} = \Delta t u / \Delta x$, which is a critical parameter for the stability of computational fluid dynamics (CFD) simulations. Now, using equation (2.53) it is possible to iteratively find a solution of φ given an initial guess of φ_x^0 and the required boundary conditions. The above considerations should suffice to conceive the algorithm involved in CFD simulations; however, it has to be pointed out that the discussion only provides a qualitative picture, whereas the true numerical solution in commercial CFD softwares is much more involved [40].

2.4 Homogeneous-Heterogeneous Reactor Dynamics

In catalytic systems, heterogeneous and homogeneous reactions may be strongly coupled through heat and mass transfer, or by exchange of reactive intermediates and radical species. The catalyst surface may provide sufficient heat to the boundary layer to ignite gas phase reactions, transfer limiting reactants from and to the boundary layer, or act as a source or sink of radicals. It is important to distinguish between two regimes:

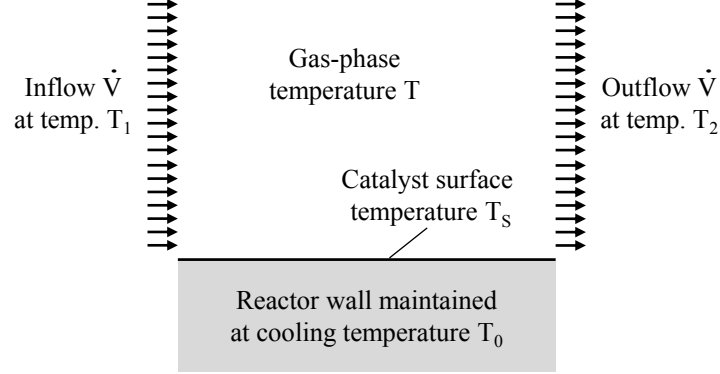


Figure 2.1: Homogeneous-heterogeneous reactor model.

catalytic reactions on the surface on the one hand, and *catalytically stabilized reactions in the gas phase* on the other hand. In the former, reactions and heat release occur primarily on the catalyst surface, while in the latter case homogeneous and heterogeneous reactions play an important role.

In order to illustrate the dynamics, it is sufficient to introduce a simple reactor model (inspired by [41, 42]) consisting of a gas-phase flow and a cooled catalyst surface (Figure 2.1). Steady-state energy balance equations for the catalyst surface with temperature T_s and the gas-phase with temperature T may be written as

$$\text{surface energy balance:} \quad 0 = \dot{Q}_s^{\text{react}} - \alpha A (T_s - T) - K (T_s - T_0) \quad (2.54)$$

$$\text{gas phase energy balance:} \quad 0 = \dot{Q}^{\text{react}} + \alpha A (T_s - T) - \dot{V} n c_p \Delta T \quad (2.55)$$

where \dot{Q}^{react} is the heat release by chemical reaction on the surface and in the gas phase respectively (in W), α the convective heat transfer coefficient between the two phases (in W / (m² K)), A the catalyst surface area (in m²), K the cooling heat transfer coefficient (in W / K) with cooling temperature T_0 , \dot{V} the volumetric flow rate (in m³ / s), n the number density (in mol / m³), c_p the heat capacity (in J / (mol K)), and $\Delta T := T_2 - T_1$ the temperature increase in the gas phase (in K). In both equations the first term represents the reaction heat generation, the second is the heat exchange between the two phases, and the last term the heat removal by cooling and convection, respectively. It is permissible to make a simplified Arrhenius ansatz for the rate expression of the form $k_{(s)}(T_{(s)}) \propto \exp(-E_{\text{act}}^{(s)} / RT_{(s)})$ for both phases. Hence, the chemical heat release on the surface and in the gas-phase are, respectively, is $\dot{Q}_s^{\text{react}} = A k_s(T_s) \Delta_r Q_s$ and $\dot{Q}^{\text{react}} = V n k(T) \Delta_r H$. Here, A and V are the catalyst surface area and the gas-phase volume, respectively, $\Delta_r Q_s$ is the reaction heat release per area on the surface (in J / m²), and $\Delta_r H$ the reaction enthalpy per mole in the gas phase (in J / mol).

$$0 = A k_s(T_s) \Delta_r Q_s - \alpha A (T_s - T) - K (T_s - T_0) \quad (2.56)$$

$$0 = V n k(T) \Delta_r H + \alpha A (T_s - T) - \dot{V} n c_p \Delta T. \quad (2.57)$$

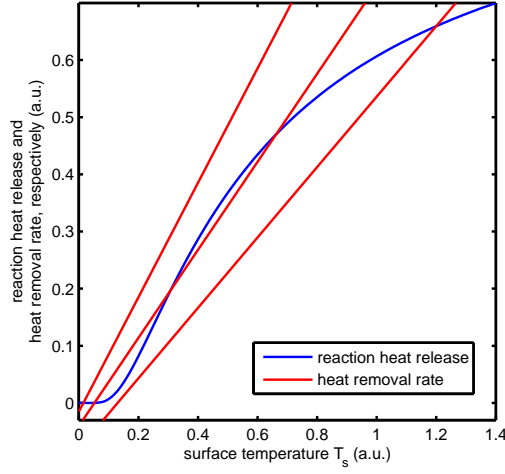


Figure 2.2: Reactor stability diagram, showing the reaction heat release and heat removal rate (red and blue curves, respectively) as a function of the surface temperature T_s . The reaction heat release is plotted as a generic inverse temperature exponential of the form $\exp(-a/T_s)$, while the heat removal rates correspond a set of generic linear functions $bT_s + c$. (adapted from [41])

In the **catalytic reaction regime** the role of the catalyst is to provide alternative reaction pathways. Catalyst activation energies E_{act}^s are usually smaller than in the homogeneous phase $E_{\text{act}} > E_{\text{act}}^s$, implying smaller catalyst ignition temperatures $T_{\text{ign}}^s < T_{\text{ign}}$ compared to the gas phase. Evidently, reactions on the catalyst surface are limited by the rate at which reactants are transported to the surface or at which products can be transported away. Assuming a gas temperature $T < T_{\text{ign}}$, i.e. too low to ignite gas phase reactions, one finds the the solution:

$$A k_s(T_s) \Delta_r Q_s = K (T_s - T_0) + \dot{V} n c_p \Delta T. \quad (2.58)$$

The solution is a function of the catalyst temperature T_s only and can be represented in a reactor stability diagram, in which the left- and right-hand side of the equation are plotted (Figure 2.2). Operation is stable if the heat generated by reaction (left-hand side equation) is removed by cooling and convection (right-hand side equation). Intersections of the two graphs correspond to steady state conditions, referred to as kinetically controlled at low temperatures (left graph) and mass transfer controlled operation at high temperatures if catalyst reactions are ignited (right graph). For the middle graph the reactor would operate in an unstable condition since there is not a singular stable operation point which leads to instationary behavior and oscillation of the reactor temperature. Naturally, the reaction rate has also be convoluted by a rate limiting mass transfer term, but despite the fact that mass transfer has not been included in this simple model, it shows general operation conditions. In this case, the gas phase temperature $T = T_s - \dot{V} n c_p \Delta T / (\alpha A)$ is generally smaller than the catalyst temperature.

In the **catalytically supported homogeneous reaction regime** elevated temperatures may lead to the ignition of gas phase reactions. This results in the following solution:

$$A k_s(T_s) \Delta_r Q_s + V n k(T) \Delta_r H = K (T_s - T_0) + \dot{V} n c_p \Delta T \quad (2.59)$$

which is no longer a function of T_s alone and cannot be plotted in a simple way. This already indicates that operation in this regime may be more difficult to describe, let alone mass transfer limitations which have not been accounted for here. As a consequence, in high temperature catalysis it is difficult to disentangle the coupled homogeneous-heterogeneous reactions.

Homogeneous-heterogeneous reactor dynamics have been studied experimentally and analytically by references [41, 43, 44]. For instance in experiments by [43, 44], a stationary stagnation flow (which can conveniently be described by means of a stream function depending on one spatial coordinate only) impinging on a platinum plate was studied. The catalyst plate was resistively heated and the surface temperature was monitored as a function of heating power for different fuel-to-air ratios (Figure 2.3 (a)). At low heating power, surface temperature increases essentially linearly with power while the surface is basically cooled convectively by the flow. At a certain power the surface temperature increases rapidly due to heat release by exothermic surface reactions, leading to a nonlinear increase (curves C and D). In this region a transition from a kinetically limited reaction to a mass transfer limited reaction occurs. Under appropriate conditions the state is a self-sustaining autothermal state which leads to hysteresis effects when heating power is withdrawn. A further increase eventually leads to homogeneous ignition. It is important to note that ignition, extinction, and autothermal characteristics are observable only under consideration of both, homogeneous and heterogeneous reactions.

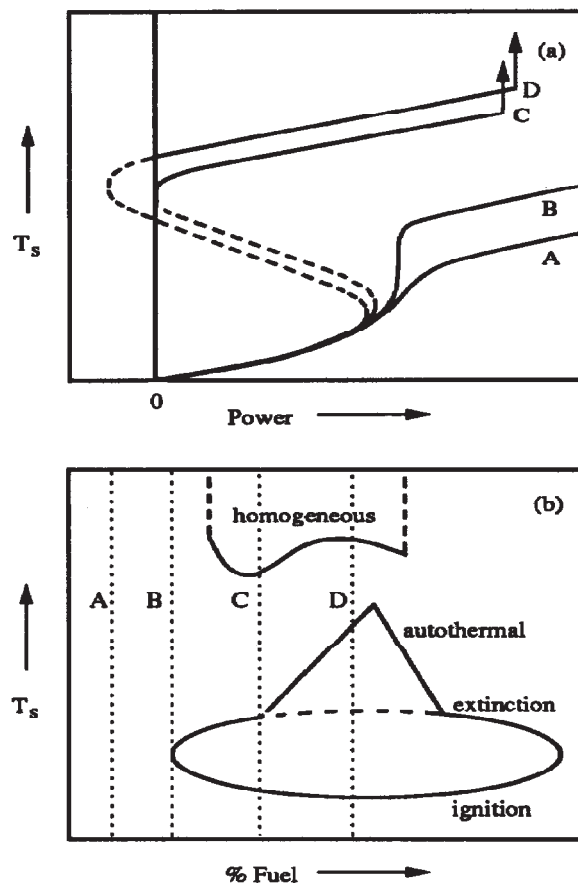


Figure 2.3: Schematic representation of one-parameter (power) and two-parameter (power and feed composition) bifurcation diagrams. Each curve of (a) is obtained by varying power with all remaining parameters fixed. A family of curves, of which four are shown, is generated by varying feed composition. The surface temperature at the bifurcation and autothermal points for each one-parameter curve is plotted as a function of feed composition to produce the two-parameter bifurcation diagram of (b). (reprinted from [44] R.J. Olsen, W.R. Williams, X. Song, L.D. Schmidt, and R. Aris. Dynamics of homogeneous-heterogeneous reactors. Chemical Engineering Science, 47(9-11):2505 - 2510, 1992. Twelfth International Symposium on Chemical Reaction Engineering Today, with permission from Elsevier)

Chapter 3

Methodology

3.1 Laser Spectroscopic Methods

Laser-spectroscopy methods have been applied for thermometry purposes as well as for the detection of transient reaction intermediates, namely OH and CH₂O.

3.1.1 Raman Scattering

Raman scattering is an inelastic scattering process in which the dipole radiation induced by the incident electromagnetic field is modulated by the molecular motion. The process is accompanied by a transfer of energy between the molecule and the incident photon, and the wavelength of the scattered Raman signal is shifted by the vibrational or rotational energy with respect to the excitation wavelength (Table 3.1 shows Raman shifts and scattering cross-sections for selected species). The red-shifted bands are called Stokes, while the blue-shifted band are named Anti-Stokes. An example for the vibrational Stokes Raman spectrum of molecular nitrogen in ambient air is shown in Figure 3.1.

Despite the λ^{-4} dependence of the scattering intensity (cf. equation (2.15)) the frequency doubled Nd:YAG line at 532 nm has been identified to be the most suitable common laser wavelength for Raman scattering [45]. For shorter wavelength the signal-to-background ratio in fuel-rich flames is spoiled by the strong fluorescence mainly from polycyclic aromatic hydrocarbons. Figure 3.2 shows Anti-Stokes and Stokes Raman spectra of N₂ in a stoichiometric methane-air flame. In the top spectra, considerable amounts of chemiluminescence and laser-induced emission spoil the spectrum. In order to compensate for the strong background signals it is possible to take advantage of the polarization properties of the Raman signal. In one instance the laser polarization has been set perpendicular to the detection optical axis (\perp), in the other case it was adjusted to be parallel (\parallel). In the parallel case the induced dipole oscillation is parallel to the optical axis and since a dipole radiation in that direction vanishes (cf. equation (2.11)) there is no Raman signal, while the background signal remains. In fact, the signal does not vanish absolutely because the mean polarization tensor may have off-diagonal elements, however the depolarization ratio for small molecules is usually very small (cf. Section 2.1.3 and [29]). The difference spectra are shown in the bottom graphs of Figure 3.1. A clear vibrational spectrum could thus be recorded.

3.1. Laser Spectroscopic Methods

Species	Raman shift (cm ⁻¹)	Raman cross-section (cm ² /sr x 10 ⁻³⁰)	Rayleigh cross-section (cm ² /sr x 10 ⁻²⁸)
H ₂	4156	1.10	1.32
H ₂ O	3652	0.98	4.4
C ₂ H ₄	3020	1.9	
	1623	0.76	
CH ₄	3017	1.7	13.4
	2917	2.65	
CH ₃ OH	2955	2.75	20.3
C ₃ H ₈	2890	1.80	79.0
N ₂	2331	0.37	6.1
CO	2143	0.34	7.8
O ₂	1555	0.42	5.0
CO ₂	1388	0.46	14.0
	1286	0.30	
C ₂ H ₆	993	0.6	

Table 3.1: Vibrational Raman shifts for selected species, along with Raman and Rayleigh cross-sections with respect to 532 nm excitation (adapted from [50] and [25]).

There are two ways to extract information about the vibrational temperature from the Raman spectra [46, 47]. First, it is possible to compare the intensities of the Anti-Stokes and Stokes band. This is because the Anti-Stokes band arises only from elevated states, while the Stokes band is dominated by the ground state population. It can be seen in the Figure that the total intensity of the Anti-Stokes band is smaller than the Stokes counterpart. The problem is that this technique requires a calibration constant since the efficiency of the detection system may not be identical for both wavelengths. However, in fact the same information about the vibrational population distribution is also contained in either one spectrum. Due to anharmonicity the upper vibrational Q-branches are blue-shifted and one perceives the $1 \rightarrow 0$, $2 \rightarrow 1$ and even the $3 \rightarrow 2$ bands in the spectrum. In Chapter 4 this has been used to measure the temperature profile in a stoichiometric methane-air flame. By using Boltzmann's distribution law (2.28), the vibrational temperature is calculated from the vibrational band intensity I_v (i.e. the sum of all rotational lines within a $v + 1 \rightarrow v$ band) [48]:

$$I_{v+1 \rightarrow v} \propto \frac{(v+1)}{\lambda_R^4 Z_{\text{vib}}} \exp\left(-\frac{E(v)}{k_B T}\right) \quad (3.1)$$

v being the vibrational quantum number, λ_R the Raman wavelength, Z_{vib} the partition function, and $E(v)$ the molecular energy term.

3.1.2 Laser-Induced Fluorescence (LIF)

A reactor for in-situ species and temperature profile measurements has been developed by the group. In the current experimental setup gas phase composition and temperature

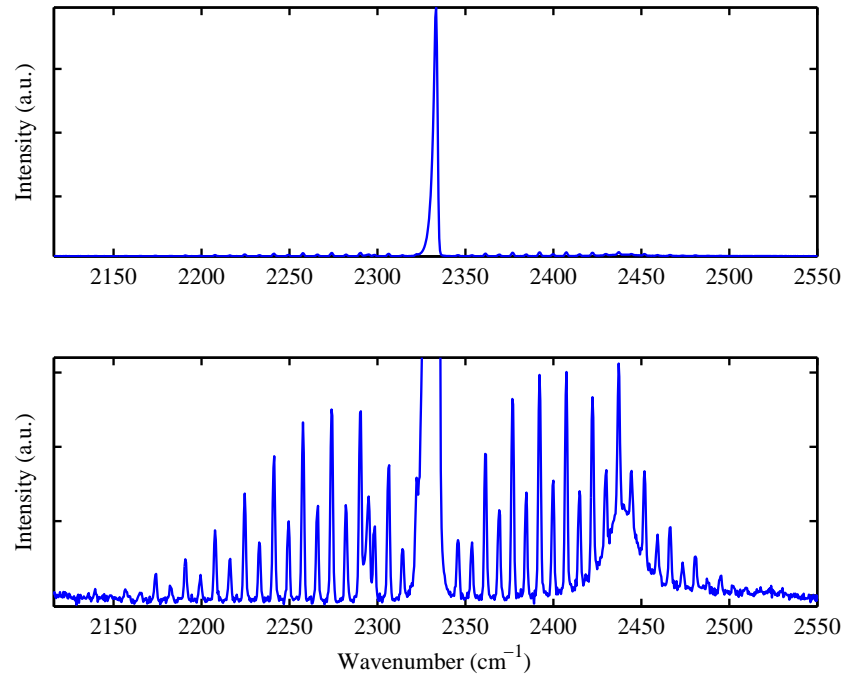


Figure 3.1: Vibrational Raman spectrum of N_2 in ambient air, showing the dominant Q-branch ($\Delta J = 0$). The bottom plot shows the same spectrum on a different scaling in order to bring out the rotational O- and S-branches ($\Delta J = \pm 2$), where the line separation corresponds to four times the rotational constant B . The intensity alternation of the branches is due to nuclear spin statistics [49]. The additional line appearing at 2295 cm^{-1} belongs to the $2 \rightarrow 1$ hot band. The broad feature at 2440 cm^{-1} (611 nm) is presumably attributed to an Eu^{3+} transition of the laboratory lighting.

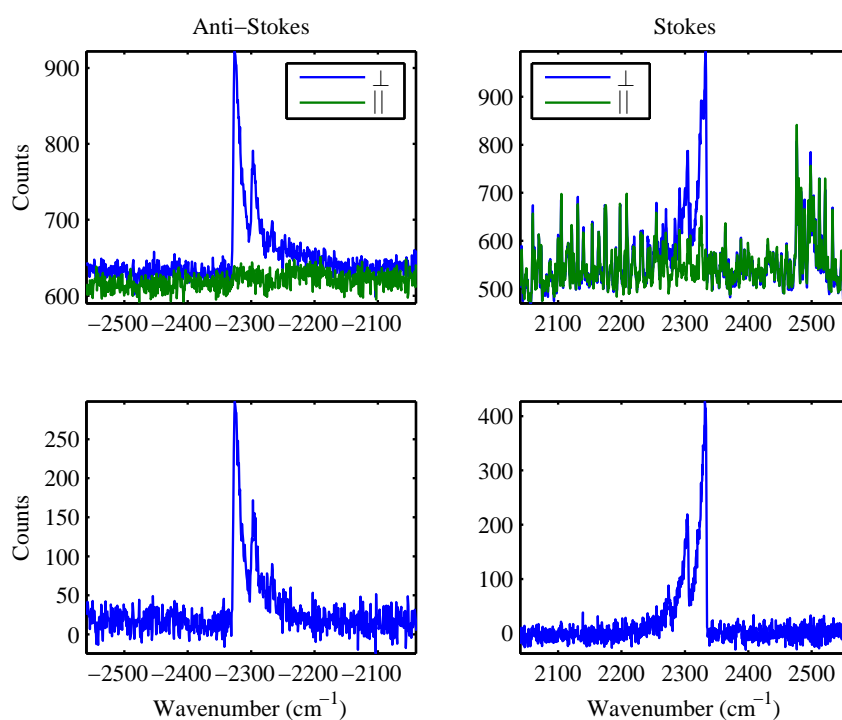


Figure 3.2: Vibrational Anti-Stokes and Stokes Raman spectrum of N_2 in a methane/air flame. The top spectra show the polarized (\perp) and depolarized (\parallel) spectra, the difference spectra of which are shown in the bottom graphs. The laser power is at 10 W and the spectra were integrated over 4x25 seconds.

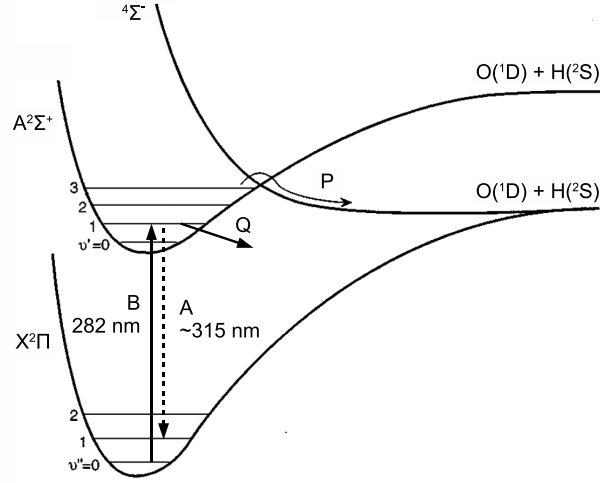


Figure 3.3: OH potential energy diagram and LIF scheme. Typical rates for spontaneous emission are $A = 1/\tau_{\text{rad}} \approx 10^6 \text{ s}^{-1}$, collisional quenching $Q \approx 10^9 \text{ s}^{-1}$ in flames at atmospheric pressure [51], predissociation $P \approx 10^{10} \text{ s}^{-1}$ for $v' = 3$ [52] (Figure adapted from [53]).

are measured by means of a quartz capillary that can be traversed along the reactor axis. The capillary houses a thermocouple for the temperature measurement and at the same time allows for extraction of reaction gases through the capillary. The gases are then analyzed using standard diagnostic methods, such as gas chromatography (GC) and mass spectrometry (MS). Unlike stable reaction species, radicals are short-lived (such as OH) and do not survive the sampling process. Other species are prone to dissolve in water which in turn condenses in the tubing (such as CH_2O) or the vapor pressure of the species itself may be too low to guide the gases sample to the diagnostics.

Laser-induced fluorescence (LIF) spectroscopy is a commonly applied non-intrusive and sensitive spectroscopic tool for detection of minor species. It is a resonant, incoherent¹ method which works as follows: a laser pulse creates an electronic excitation of one of the vibrational-rotational energy levels; this excitation is followed by the emission of fluorescence photons at a unique wavelength, which are then detected. As a first-order estimate the number density in the detection volume is assumed to be proportional to the fluorescence signal. The process is illustrated in Figure 3.3, also showing the non-radiative de-excitation channels, namely collisional quenching Q and predissociation P .

A quantitative expression for the number of detected fluorescence photons N_{ph} which helps to understand the factors influencing the LIF process is:

$$N_{\text{ph}} = \underbrace{\frac{B_{12} I_{\nu} \tau}{c}} n V f_B(T) \underbrace{A_{21} \tau_{\text{eff}}}_{\text{fluorescence yield}} \underbrace{(\Omega/4\pi) \eta}_{\text{detection efficiency}} \quad (3.2)$$

where B_{12} is the Einstein coefficient of absorption (in $\text{m}^3 \text{ Hz J}^{-1} \text{ s}^{-1}$), I_{ν} the spectral irradiance of the laser (in $\text{W / m}^2 \text{ Hz}$), τ the pulse length (in s), c the speed of light;

¹In this context, incoherent refers to the uniform radiation in all directions, in contrast to coherent non-linear optical techniques, such as Coherent Anti-Stokes Raman Spectroscopy (CARS), where the signal is emitted in a laser-like beam of radiation.

n is the number density of LIF molecule in the electronic ground state ($1 / \text{m}^3$), V the detection volume (in m^3), $f_B(T)$ the temperature-dependent Boltzmann fraction i.e. the portion of molecules in the vibrational-rotational level being excited, $A_{21} = 1/\tau_{\text{rad}}$ Einstein coefficient for spontaneous emission (in $1 / \text{s}$) and the corresponding radiative lifetime τ_{rad} , τ_{eff} the effective lifetime of the laser excited state (in s), Ω the collection solid angle, and η the instrumental detection efficiency.

The expression constitutes three parts corresponding to the excitation-absorption process, the fluorescence emission, and the detection system efficiency, respectively. The spectral energy density is $\rho_\nu = I_\nu/c$ so that the first part of the right hand side equation $B I_\nu/c\tau$ stands for the excitation probability of an individual molecule in the radiation field. Hence, the whole expression $B I_\nu \tau/cn V f_B(T)$ represents the molecule-specific excitation-absorption characteristics and thus the actual number of molecules being excited, in which the Boltzmann fraction is a function of temperature T . Generally, it is possible to determine a vibrational-rotational ground state which is to a large extent insensitive to temperature variations, that is $f_B(T) \simeq \text{const.}$ for the relevant temperature regime. The term $A\tau_{\text{eff}}$, often referred to as the quantum yield Φ , is a measure for the amount of fluorescence photons emitted per molecule excited and accounts for non-radiative decay of the excited state, either by predissociation or collision-induced intra- and intermolecular energy transfer. It is desirable to find an excitation scheme which is little sensitive to non-radiative quenching, or a means for compensation of its effect. The quantum yield Φ may be in a first-order attempt written as (with respect to Figure 3.3)

$$\Phi = A\tau_{\text{eff}} = \frac{A}{A + Q + P} \quad (3.3)$$

where P denotes the predissociation rate and Q the collisional quenching rate, the latter being a function of pressure and composition in particular. The last term $(\Omega/4\pi)\eta$ corresponds to the efficiency of the detection system and is largely dependent on experimental conditions.

Hydroxyl Radical Laser-Induced Fluorescence

From a molecular point of view OH is a diatom characterized by an unpaired electron, while from a kinetic perspective it is an aggressive reaction intermediate; however, from the thermodynamic perspective it is an equilibrium product of considerable amount at typical combustion conditions (Figure 3.4). It becomes evident why OH LIF in combustion environments can be accomplished with relative ease, whereas detection of OH at fuel-rich conditions becomes challenging due to drastically decreased concentrations.

OH probing is commonly done via the $A^2\Sigma \leftarrow X^2\Pi$ band, i.e. the ground and first excited electronic state.² Brockhinke and co-workers [51] have measured time-resolved fluorescence spectra, which nicely illustrate temporal and spectral evolution of the fluorescence due to vibrational and rotational energy transfer (VET and RET) within the OH molecule after excitation of a single state. VET and RET is the energy redistribution among vibrational and rotational levels in the same electronic state following excitation. In simple terms collisional quenching can be thought to decrease the

²Conventionally, for excitation as well as fluorescence transitions, the electronically excited vibrational state is mentioned first, i.e. the 3-0 transition refers to the $A^2\Sigma v' = 3$ and $X^2\Pi v'' = 0$ system. The excited fluorescence state $A^2\Sigma$ is marked by one apostrophe while the initial level $X^2\Pi$ is labeled by two apostrophes.

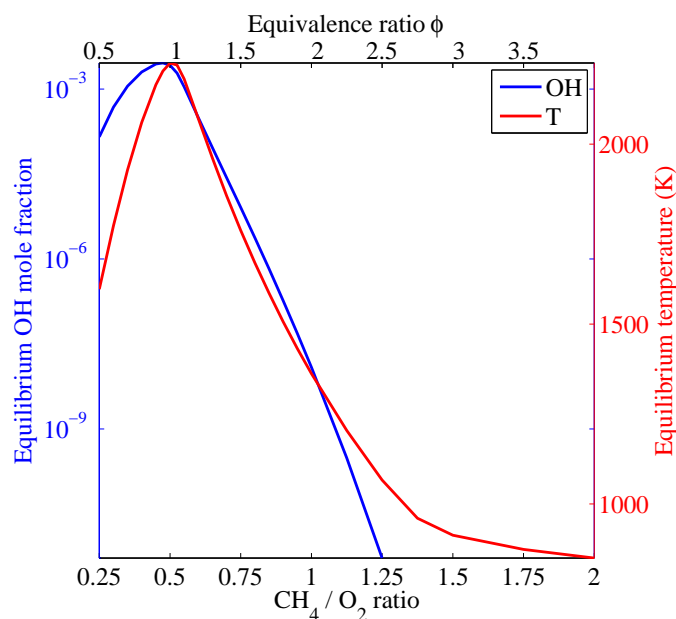


Figure 3.4: Equilibrium OH mole fraction and temperature as a function of CH_4/O_2 ratio (bottom axis) and equivalence ratio ϕ (top axis) in 80 % Ar.

overall fluorescence intensity due to non-radiative de-excitation (as represented by the quantum yield equation (3.3)), and furthermore there also is a dependence on chemical composition and temperature of the collisional bath and even with respect to the excited rotational states [54]. Multiple LIF excitation and detection schemes have been reported which are more or less sensitive to collisional quenching, and yield stronger or weaker signals depending on the vibrational-rotational state used for excitation and detection. Reference [55] compared some of them in respect to signal strength and quenching sensitivity for the OH radical. Though excitation and detection of the 0-0 band is most efficient this scheme is disregarded here since the fluorescence signal cannot be decoupled from elastic scattering effects. One particularity in OH is the existence of a predissociative vibrational state ($v'' = 3$) which exhibits a short dissociation lifetime compared to the lifetime at atmospheric pressure. Therefore the 3-0 scheme is convenient since its dependence on quenching is drastically reduced. However, the disadvantage is a significantly lower quantum yield. Excitation of the 1-0 band is the most suitable excitation scheme for our purposes, with an excitation wavelength around 281 nm and detection in the 1-0 and 0-0 bands around 310 nm. The fluorescence yield is reasonable and the red-shifted detection allows effective decoupling from any elastically scattered radiation.

3.1.3 Resonance-Enhanced Multi-Photon Ionization (REMPI)

Resonance-Enhanced Multi-Photon Ionization (REMPI) takes advantage of intermediate energy levels to selectively ionize the molecule of interest. Selectivity is achieved due to the resonant excitation of the intermediate energy level, following ionization by absorption of an additional photon. Depending on the number of photons need for the resonant N_r and the ionization transition N_i the REMPI process is labeled $N_r + N_i$.

	REMPI transition	Excitation wavelength
OH	$2+1 D^2\Sigma^- - X^2\Pi_i$	2 x 243 - 247 nm
NO	$1+1 A^2\Sigma^+ - X^2\Pi_i$	270 - 317 nm
	$2+2 A^2\Sigma^+ - X^2\Pi_i$	2 x 452 nm
CO	$2+1 B^1\Sigma^+ - X^1\Sigma^+$	2 x 230 nm
	$2+1 C^1\Sigma^+ - X^1\Sigma^+$	2 x 217.5 nm
CH ₃	$2+1 3p^2 A''_2 - \tilde{X}^2 A''_2$	2 x 333.5 nm
	$2+1 4p^2 A''_2 - \tilde{X}^2 A''_2$	2 x 286.3 nm

Table 3.2: REMPI transitions for some small molecules of interest in combustion studies (adapted from [64]).

REMPI enables the detection of absorbed laser photons by monitoring the ions which can be collected very efficient, and therefore this ionization spectroscopy method represents a very sensitive detection method [56]. The ions may be collected e.g. directly by means of a high-voltage electrode [57, 58], in a mass spectrometer [59, 60, 61], or by monitoring the microwave signal scattered by the free charge cloud [62, 63]. An advantage of REMPI in combination with mass spectrometry is that it yields fragment-free mass spectra. Table 3.2 lists examples of REMPI transitions for small molecules encountered in combustion studies.

3.2 In Situ Laser Diagnostics using Optical Fibers

Laser-spectroscopic methods, such as laser-induced fluorescence (LIF), allow detection of transient species, at the expense of providing optical access to the system. However, this is not always possible in practical systems. On this account fiber-optic probes have been developed in order to establish minimal-invasive optical access to the system.

3.2.1 Optical Fiber Probes

Throughout the thesis different fiber probes were developed and tested. Figure 3.5 shows three different fiber geometries that were most promising for laser-induced measurements in the gas-phase. The first fiber probe (a) consists of a single fiber through which the excitation light is delivered as well as fluorescence is collected. The benefit of this geometry is a maximum collection efficiency. However, the disadvantage is that the excitation laser induces scattering while passing through the fiber which consequently reduces the signal-to-background ratio. This fiber probe was used in the experiments presented in Chapters 4 and 5. The second probe assembly (b) consists of an individual excitation fiber surrounded by a light-guiding capillary for collection of the fluorescence. Since the delivery and detection channels are decoupled the scattering background is minimized and the signal-to-background ratio is maximum. One disadvantage, similarly to the single fiber, is the poor spatial resolution due to the elongated collection volume. This probe was employed in the experiments described in Chapter 6. The third geometry (c) constitutes a side-firing excitation fiber polished at a 45° angle [65]. The 45° interface gives rise to total internal reflection so that the light exits at right angles to the fiber axis. At the expense of a small collection efficiency

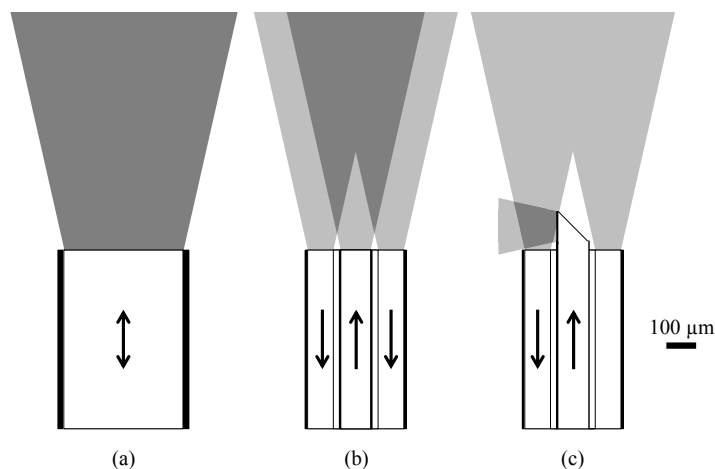


Figure 3.5: Fiber probe geometries. The dark shade represents those areas that are illuminated by the laser excitation and from which fluorescence is captured, i.e. the effective collection volume.

this probe feature a well-defined detection volume and a high spatial resolution. However, the shaped fiber-tip is difficult to manufacture and may easily be damaged during assembly.

3.2.2 Raman Thermometry through an Optical Fiber

In an analogous manner to the Raman thermometry method presented above (Section 3.1.1) and applied in Chapter 4, it was attempted to measure vibrational Raman spectra through an optical fiber. Due to the small Raman scattering cross-sections the single fiber probe (a) was used since it has the highest collection efficiency. The probe molecule needs to feature a Raman shift which is large enough so that the signal can be spectrally separated from the fused silica Raman background. N_2 Raman thermometry should generally be possible but the fiber-coupler would need to be flushed with a gas other than nitrogen, otherwise the ambient air Raman signal from the coupling-side is indistinguishable from the Raman signal originating from the other end of the fiber. Apart from this complication, our experiments were generally conducted in the absence of nitrogen and therefore N_2 thermometry was discarded. In principle, methane constitutes an ideal marker molecule for thermometry in fuel-rich feeds since it is present before as well as after the reaction in relatively larger amounts. Raman spectra of the 2917 cm^{-1} band were recorded, but unfortunately the temperature-sensitivity of that Raman band is relatively weak and interpretation is not straightforward [66, 67].

3.3 Capillary Sampling

Sampling of the reacting gas mixture is accomplished by means of a fused silica capillary that is traversable along the reactor axis and thus allows continuous sampling of the reacting gas. When probing a reacting gas mixture one has to ensure rapid

3.3. Capillary Sampling

quenching of the chemical reaction in order to achieve an unbiased and representative measurement at the probing position. This may be assured if either the sampling time is short compared to changes in chemical composition, or if wall quenching by heat or radical removal inhibits reaction progress. In the gas-phase OCM experiments, the reaction timescale is usually on the order of 0.1 s while sampling occurs on a slightly shorter timescale. As far as wall quenching is concerned Ref. [68] quotes experiments on the quenching process of methane/oxygen flames between quartz walls heated up to 1000 K and report a quenching wall distance on the order of ~ 1 mm. Since the wall distance in the present experiment is significantly smaller ($\sim 45 \mu\text{m}$) it can be assumed that due to quenching of the reaction on the capillary walls (i.e. by radical recombination) and the relatively rapid transfer process the unbiased composition of the reaction gas is analyzed. One may ask whether the radical recombination to stable products changes the overall mixture composition. However, even if concentrations of these unstable species were several orders of magnitude greater than their equilibrium values at 1000 K, stable product concentrations would not be changed significantly by their recombination [69].

Results

Chapter 4

Radical Detection in Harsh Environments by Means of Laser-Induced Fluorescence using a Single Bidirectional Optical Fiber

Abstract

A new experimental method is described enabling detection of hydroxyl radicals (OH) by laser-induced fluorescence in high-temperature gas-phase reactions. This is accomplished by means of a bidirectional optical fiber probe, which is of interest for applications where optical access is limited. An optical setup that allows simultaneous excitation and detection of fluorescence using one and the same fiber has been developed. Complications resulting from coupling as well as laser-induced scattering are addressed, and different fibers are compared with regard to core material composition and geometric collection efficiency. On this basis, a suitable fiber is identified, and OH detection and profile measurements are demonstrated in a premixed laminar flame as reference experiment.

4.1 Introduction

Free radicals play a fundamental role in reaction kinetics underlying combustion, plasma chemistry, as well as atmospheric chemistry. Detection of radical species is challenging because of their high reactivity and ppm to ppb concentrations levels, but can

This chapter is adapted from a research article by Heiner Schwarz, Robert Schlögl, Raimund Horn. Radical detection in harsh environments by means of laser-induced fluorescence using a single bidirectional optical fiber. *Applied Physics B*, 109(1): 19-26, 2012. DOI: 10.1007/s00340-012-5172-9. The final publication is available at <http://link.springer.com/article/10.1007/s00340-012-5172-9>.

be accomplished by laser-spectroscopic methods such as cavity ring-down absorption spectroscopy (CRDS) or resonance-enhanced multiphoton ionization (REMPI) [64]. A shortcoming of these techniques is the requirement that the measurement has to be performed in an optical cavity in the case of CRDS [70], or the insertion of an ionization probe [57] or a molecular beam nozzle [61] into the reaction medium in REMPI measurements.

Laser-Induced Fluorescence (LIF) is a spectroscopic method that features high sensitivity and potential for in-situ quantification [25, 71]. In LIF the laser wavelength is tuned to a species-specific rovibronic transition of the atom or molecule of interest, which is elevated to an excited electronic state and might - after having undergone collision-induced intra- or intermolecular energy transfer processes - eventually emit a fluorescence photon. The fluorescence signal may be considered proportional to the species' number density if quenching or predissociation effects are accounted for.

In many applications the use of LIF is hindered by the necessity for optical access to the system. The common detection arrangement necessitates at least two optical ports, which cannot always be provided. As representative examples one might imagine a reactor the walls of which consist of catalytically active (intransparent) material, a reaction chamber encapsulated by a furnace, or high pressure internal combustion engines. An alternative to direct optical access is an optical fiber which can be used for minimally-invasive in-situ detection even under harsh conditions. An example for recent experiments is a LIF sensor integrated in a spark plug in order to monitor the mixing process prior to ignition in an internal combustion engine via tracer LIF [72]. Though the excitation and fluorescence light are separately guided through optical fibers, eventually, optical access is again provided by miniature viewports in the sensor head, and the authors outline the optimization of the optical design with respect to collection efficiency.

In contrast the present approach regards the optical fiber as a probe itself. Since common fused silica fibers are chemically inert and show high temperature resistivity, they may be regarded as truly minimally-invasive probes and can be inserted directly into harsh reactive environments. There have been reports on the design and optimization of fiber-optic probes for (Raman-) measurements comprising separate fibers for delivering the excitation laser and collecting the scattered radiation [73]. It is pointed out that a single fiber "bidirectional probe design should be highly efficient since the excitation and collection light cones overlap completely" but the option is dismissed due to the amalgamation of the exciting and collected radiation. This aggravation is certainly a major concern when Raman scattering is being probed since the signal is inherently weak, and spectral decomposition of fiber-induced Raman scattering and desired Raman signal may not be possible. In contrast, fluorescence transitions may readily be found which are red-shifted beyond the vibrational Raman signature of the light-guiding material (i.e. $> 1000\text{ cm}^{-1}$) enabling spectral decoupling.

To the knowledge of the authors this is the first demonstration of experiments in which a single optical fiber is used for bidirectional LIF excitation and detection under harsh conditions.

In what follows we describe LIF detection using an optical fiber probe in a bidirectional manner and demonstrate LIF hydroxyl radical (OH) detection in a reference experiment. Section 4.2.1 outlines experimental details of the reference experiment, i.e. the premixed laminar flame, where quantitative OH concentration have been determined using a combination of conventional OH LIF and vibrational Raman scattering. Section 4.2.2 describes the optical setup for simultaneous coupling and detection

of laser-induced fluorescence, and discusses complications arising from laser-induced scattering of high-energy laser pulses through optical fibers. Section 4.3 focuses on the numerical determination of the collection efficiency and the effective detection volume of bidirectional fiber probes based on simple geometric considerations. Results are discussed in Section 4.4, and first successful fiber probe OH-LIF detection is demonstrated in the premixed laminar flame, which shows good agreement with the conventional detection scheme.

4.2 Experimental

4.2.1 Characterization of Laminar Premixed Flame

A laminar premixed stoichiometric methane-air flame was used to generate OH radicals and served as a reference experiment. The atmospheric premixed flame was anchored at the outlet of a 6 mm tube, which could be shifted vertically relative to the optic axis. Axial reference profiles of OH concentration and temperature along the burner's symmetry axis in the exhaust fume region were measured by means of LIF and vibrational Raman scattering using a conventional lens-type optical setup. Thermodynamic equilibrium considerations allow for quantification of OH concentrations based on the local temperature in the post-reaction zone.

OH-LIF The hydroxyl radical features electronic transitions in the ultraviolet spectral region and has thus been excited using a frequency-doubled dye laser (Sirah, Cobra-Strech), which is pumped by the second harmonic of a Q-switched Nd:YAG laser (Spectra-Physics, Quanta-Ray). Typical dye-laser pulses are characterized by a pulse length of ~ 8 ns, a pulse energy of ~ 1 mJ, and a nominal fundamental linewidth of 0.06 cm^{-1} . The system was tuned to the OH $Q_1(8)$ transition of the $A^2\Sigma - X^2\Pi$ (1-0) band at 283.553 nm (air) which shows only a weak temperature-dependence with respect to the Boltzmann fraction $f_B(T)$ for the expected temperature range [74]. Off-resonant detection of the 1-1 and 0-0 bands at 306-325 nm allows spectral separation of elastically scattered light of the excitation laser. In the reference experiment setup (Figure 4.1 top) the LIF laser is reflected by a longpass dichroic mirror (DM) and focused by a 15 mm lens (L, f-number $f_{\#} = 1.5$) into the flame detection volume (DV). The fluorescence is collected by the same lens in a collinear manner, and after having passed the dichroic mirror, it is focused onto a fiber bundle coupled to a grating spectrometer (SP). The dispersed light is captured on a conventional CCD without possibility for fast gating (hence the minimal exposure is set by the readout time, 16 ms). Typically 1000 individual shots were recorded. The chemiluminescence-corrected (due to the long exposure) LIF intensity may be assumed to be a measure for the OH number density. The resulting OH concentration profile above the flame's reaction cone is shown in Figure 4.2 (blue markers). Quantification is obtained by temperature measurements explained in the next section.

Raman Temperature Measurements In measurements conducted by Battles et al. [75] it was shown that local OH concentrations may be correlated to the local temperature by assuming thermodynamic equilibrium, an assumption valid in the product-gas plume behind the luminescent reaction zone of the flame. In order to calculate the equilibrium composition the local temperature was measured by means of vibrational Raman scattering. Lapp et al. [76, 46] suggest several methods to deduce temperature

from vibrational Raman signatures of nitrogen in air-fed flames. The same detection setup as described in the previous paragraph (and shown in Figure 4.1 top) was thus employed, but a continuous-wave Nd:YVO₄ laser (Coherent Verdi V10, 532 nm) was used providing a 7 W beam at right-angles to the collection optics, and N₂ spectra were recorded for exposure times of 30 seconds. Using a continuous-wave source under steady-state conditions permits high laser powers to be used without risk of inducing optical breakdown or the need for pulse stretching. The polarization plane could be rotated using a $\lambda/2$ -plate which allows for polarization-separated measurements as proposed by Gruenefeld [77]. Raman scattering occurs predominately perpendicular to the laser's polarization direction. If the laser-polarization is tuned to be parallel to the detection optical axis no Raman signal is captured while unpolarized fluorescence and chemiluminescence is seen (Figure 4.3 top). The difference spectrum yields the pure Raman signal (Figure 4.3 bottom). The vibrational Raman temperature was then determined by comparing the area of the $1 \leftarrow 0$ band to the $2 \leftarrow 1$ band and using Boltzmann statistics. The integral Raman vibrational band intensity I_v (i.e. the sum of all rotational lines within a $v + 1 \leftarrow v$ band) is [48]:

$$I_{v+1 \leftarrow v} \propto \frac{(v+1)}{\lambda_R^4 Q_{\text{vib}}} \exp\left(-\frac{E(v)}{k_B T}\right) \quad (4.1)$$

v being the vibrational quantum number, λ_R the Raman wavelength, Q_{vib} the partition function, and $E(v)$ the molecular energy term.

The resulting temperature profile is also depicted in Figure 4.2 (red markers) together with the OH concentration. The experimentally determined temperature maximum of ~ 2200 K agrees well with the expected adiabatic flame temperature. To obtain local OH concentrations for calibration thermodynamic equilibrium calculation were performed with CHEMKIN [78] based on the standard thermodynamic database provided with the program (v. 4.0).

4.2.2 Fiber Coupling and Laser-Induced Scattering

When optical fibers are used to transmit high power pulsed laser (UV-)radiation coupling, transmission attenuation and inelastic scattering of the fiber material need to be taken into consideration.

The bottom part of Figure 4.1 shows the optical setup adapted for bidirectional fiber coupling and detection, which is a modification of the arrangement described in the first section. The coupling lens is chosen such that the numerical aperture (NA) given by its focal length and the laser diameter corresponds to the numerical aperture NA of the fiber. At the same time, this assures that the fluorescence response returned through the fiber is completely captured. A tri-axial fiber coupler stage permits positioning of the fiber end-face.

Coupling high-intensity laser-pulses into optical fibers may lead to surface or bulk breakdown processes of the fiber material, such as optical breakdown occurring at the fiber entrance or exit surface [79], or re-imaging of the focal point within the fiber leading to bulk damage [80, 81]. Also optical breakdown of the gas-phase in front of the fiber surface would spoil every spectroscopic investigation, as the waist of the Gaussian beam is on the order of several microns, resulting in high peak intensities for pulsed lasers. With respect to this problem the focal spot intensity distribution was homogenized using a micro-lens array (LA in Figure 4.1) designed to yield an almost flat-top intensity distribution and a focal waist of the size of the fiber diameter [79]. The fiber end-faces were polished using 1 μm polishing paper.

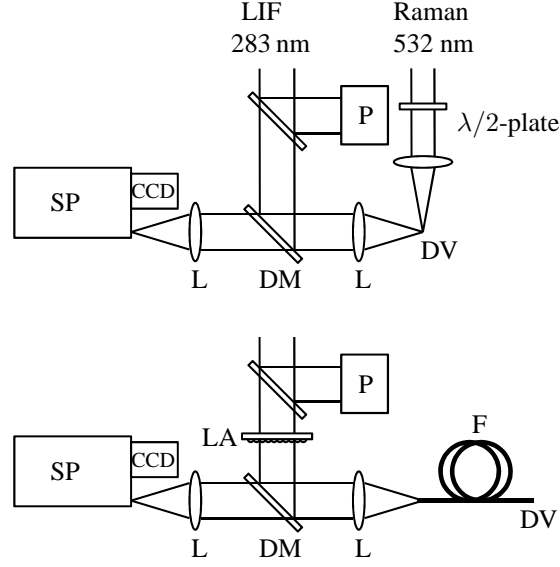


Figure 4.1: Schematic representation of optical setup for conventional LIF and Raman measurements (top), and bidirectional fiber coupling and detection (bottom): DM dichroic (longpass) mirror, L lens, LA micro-lens array, P power-meter, F fiber, DV detection volume, SP spectrometer.

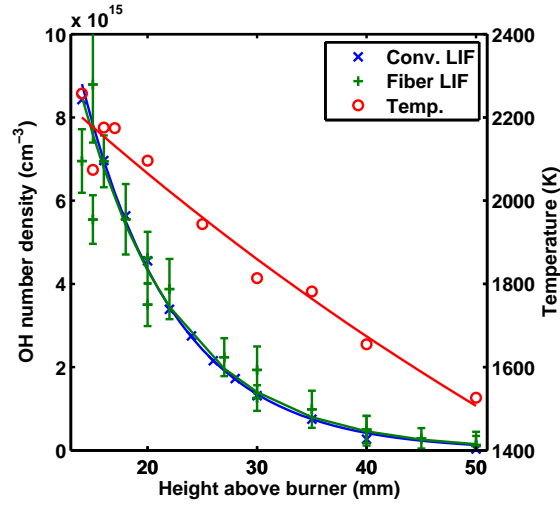


Figure 4.2: Left axis: OH number density profiles using conventional lens-type LIF (blue crosses) and fiber probe LIF (green pluses with error bars). Conventional measurement error bars of similar order as for fiber probe but omitted for clarity. Right axis: Raman temperature profile (red circles). Lines are exponential fits.

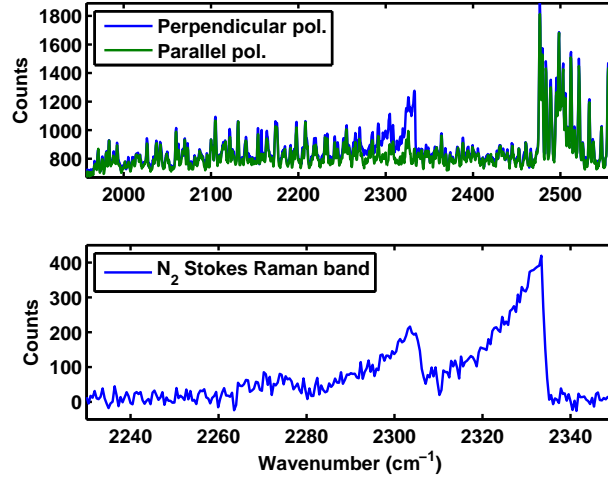


Figure 4.3: Top: Spectrum with laser polarization perpendicular (including Raman signal) and parallel (only fluorescence and chemiluminescence) to the detection optical axis. Bottom: Difference spectrum featuring the pure Raman signature of N_2 . Three vibrational bands are perceptible, corresponding to $v = 1 \leftarrow 0$, $2 \leftarrow 1$, and $3 \leftarrow 2$ (from right to left).

Step-index multimode fibers made of fused silica (SiO_2) with fluorine-doped claddings are commercially available and suitable for UV transmission. They possess high damage threshold intensities, and are characterized by their OH-content (referred to as high-OH and low-OH) as well as the amount of trace impurities. High-OH fibers show better UV-transmission characteristics than those with low OH-content. The fiber material's inherent, fabrication-induced impurities and defects may lead to undesired fluorescence, additional Raman bands, color-center formation, and photodegradation effects [82, 83, 84, 85]. Stimulated Raman scattering and non-linear effects become important only for longer fibers or higher laser intensities [84].

In Figure 4.4 the back-scattering spectra of two fibers characterized by low and high OH-content are shown. Both samples have the same geometrical properties (core diameter of $500 \mu m$, length 1 m) and comparable pulse-energies are transmitted (indicated in the legend) at a laser wavelength of 280 nm. The Raman spectrum of vitreous fused silica features phonon and defect bands at wavenumbers $< 1200 \text{ cm}^{-1}$ (corresponding to 290 nm here) [82]. These are to a large extent blocked by the dichroic mirror but are still clearly seen for both fiber types. Above 300 nm (corresponding to 2400 cm^{-1}) two distinct features are observed. The high-OH fiber has a nearly featureless spectrum except for a dominant peak around 312 nm (Raman shift 3714 cm^{-1} , FWHM 112 cm^{-1}) which is to be attributed to the vibrational Raman band of the OH-groups [82]. Naturally, the OH Raman peak is red-shifted by the same frequency from the excitation wavelength as the OH fluorescence band ($\omega_e = 3738 \text{ cm}^{-1}$ in the OH X^2II state) and thus interference renders the high-OH fiber less suitable with respect to the detection of OH radicals. On the other hand the low-OH fiber is characterized by broadband features the origin of which have not been unambiguously identified but might be attributed to fluorescence by trace species originating from the production process or color-center formation upon high-power UV transmission [84, 85]. It has to

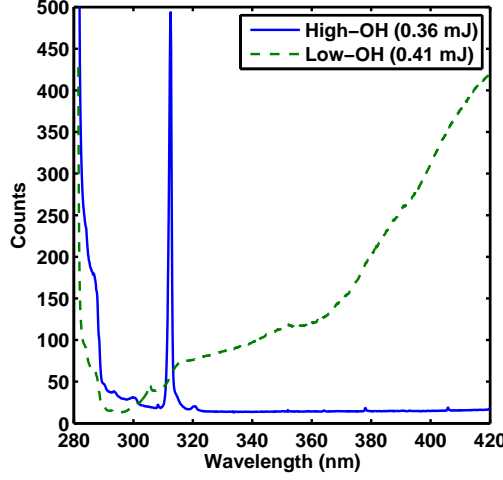


Figure 4.4: Laser-induced scattering for high- and low-OH fiber (core diameter 500 μm , length 1 m) induced by 280 nm laser pulses. The legend includes the respective transmitted pulse energies.

be mentioned that scattering depends strongly on accurate coupling alignment indicating that also the high-index fiber cladding (usually F-doped silica) may contribute to characteristic spectral features.

The same characteristic fiber scattering spectra (i.e. prominent OH Raman peak for high-OH fibers, and broadband fluorescence for low-OH fibers) have also been observed for excitation at 355 nm.

4.3 Geometrical Considerations on Collection Efficiency

On the one hand it is desirable to predict the detection efficiency's dependance on fiber parameters (like fiber diameter or numerical aperture), as well as to assess the size of the detection volume and the spatial resolution. On the other hand one would like to compare quantitatively the detection efficiency of an optical fiber probe to a conventional lens-type optical setup. The following section outlines an approach to describe the irradiance distribution $I(x)$, and the detection solid angle field $\Omega(x)$ of an optical fiber and to determine numerically the collection efficiency Γ which is going to be defined in Equation (4.2)).

An expression for the number of fluorescence photons N_{ph} upon laser-excitation may be given by

$$N_{\text{ph}} = \frac{B_{12} I_{\nu} \tau}{c} n V f_{\text{B}}(T) A_{21} \tau_{\text{eff}} \frac{\Omega}{4\pi} \quad (4.2)$$

where for simplicity a two-level system is assumed, and B_{12} is the Einstein coefficient of absorption (in $\text{m}^3 \text{Hz J}^{-1} \text{s}^{-1}$), I_{ν} the spectral irradiance of the laser (in $\text{W m}^{-2} \text{Hz}$), τ the pulse length (in s), c the speed of light; n is the number density of the probed molecule (here OH) in the electronic ground state (in m^{-3}), V the detection volume (in m^3), $f_{\text{B}}(T)$ the temperature dependant Boltzmann fraction, i.e. the portion

of molecules in the rovibronic level being excited, $A_{21} = 1/\tau_{\text{rad}}$ Einstein coefficient for spontaneous emission (in s^{-1}) with radiative lifetime τ_{rad} , τ_{eff} (in s) is the effective lifetime of the laser excited state accounting for non-radiative decay (quenching and predissociation), and Ω the collection solid angle.

Equation (4.2) holds for an infinitesimal volume dV and hence the total number of fluorescence photons collected for an arbitrary optical system is found by spatial integration

$$N_{\text{ph}} = \int_V dN_{\text{ph}} = \int_V \frac{\partial N_{\text{ph}}}{\partial V} dV \quad (4.3)$$

where $\partial N_{\text{ph}}/\partial V = B I \tau c^{-1} n f_B A \tau_{\text{eff}} (\Omega/4\pi)$ is readily found from Equation (4.2). In a homogenous environment the only parameters showing a spatial dependance are $I(\mathbf{x})$ and $\Omega(\mathbf{x})/4\pi$ if absorption is neglected for the time being. It is convenient to assume cylindrical coordinates $\mathbf{x}(r, \varphi, z)$ so that we can define the detection efficiency

$$\Gamma := \int_V I(\mathbf{x}) \frac{\Omega(\mathbf{x})}{4\pi} d\varphi r dr dz \quad (4.4)$$

as a quantitative measure for the number of collected photons for different optical setups (for convenience we only consider the irradiance I instead of the spectral quantity I_ν).

Fiber Probe Collection Efficiency A first-order estimate for the radiation field $I(\mathbf{x})$ behind the fiber endface is found by assuming the light emanates from a point source (i.e. $I(\mathbf{x}) = C/x^2$) and is isotropically distributed over the solid angle defined by the numerical aperture $\Theta_{\text{NA}} = \arcsin(\text{NA})$. According to Gauss' divergence theorem integrating $I(\mathbf{x})$ over a closed surface yields the total radiative power P within the volume enclosed by the integration surface, i.e. $P = \int I(\mathbf{x}) dS$. After integration over Θ_{NA} the constant is found to be $C = P / 2\pi(1 - \cos \theta_{\text{NA}})$ so that the radiation field can be readily expressed as

$$I(\mathbf{x}) = \frac{P}{2\pi(1 - \cos \theta_{\text{NA}}) x^2}. \quad (4.5)$$

Determining the effective collection solid angle $\Omega(\mathbf{x})$ of the fiber is a purely geometrical problem. The solid angle of an arbitrary surface S seen from a point \mathbf{x} in space may be defined as

$$\Omega(\mathbf{x}) = \int_{S(\mathbf{x}')} \frac{\mathbf{X} \cdot d\mathbf{x}'}{X^3}. \quad (4.6)$$

The integration is performed over $S(\mathbf{x}')$ with $d\mathbf{x}' = \mathbf{n}_S dS(\mathbf{x}')$ normal to $S(\mathbf{x}')$ and $\mathbf{X} = \mathbf{x}' - \mathbf{x}$. In the present consideration the surface S corresponds to the fiber end-face.

Optical rays impinging on the surface at an angle which is greater than the critical acceptance angle of the optical fiber θ_{NA} will be reflected and not contribute to the effective collection solid angle. In mathematical terms this condition is readily expressed in terms of the angle $\angle(\mathbf{X}, d\mathbf{x}')$, i.e. only if $\angle(\mathbf{X}, d\mathbf{x}') < \theta_{\text{NA}}$ does the surface element $d\mathbf{x}'$ contribute to the integration. Thus, we may rewrite Equation (4.6) as a conditional integral:

$$\Omega(\mathbf{x}) = \int_{S} \frac{\mathbf{X} \cdot d\mathbf{x}'}{X^3} \quad \angle(\mathbf{X}, d\mathbf{x}') < \theta_{\text{NA}} \quad (4.7)$$

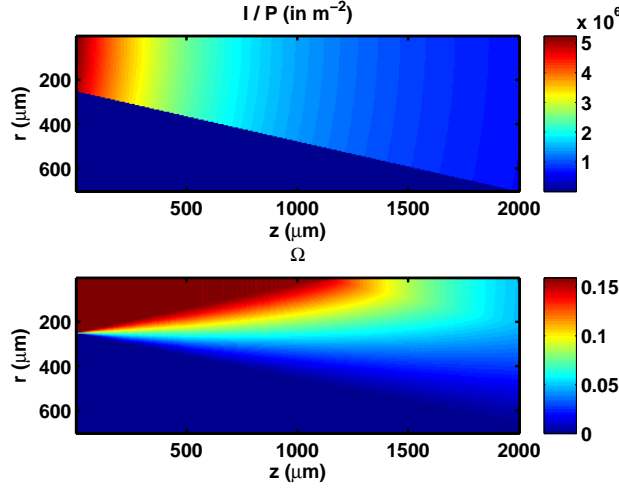


Figure 4.5: Irradiance field $I(\mathbf{x})$ (top), and effective collection solid angle distribution $\Omega(\mathbf{x})$ (bottom) in cylindrical coordinates (radial coordinated r and axial coordinated z). Fiber parameters: numerical aperture $\text{NA} = 0.22$ and diameter $D_{\text{fiber}} = 500\mu\text{m}$.

Knowledge of $I(\mathbf{x})$ and $\Omega(\mathbf{x})$ (Figure 4.5) now allows for determining the effective detection volume and the collection efficiency Γ by means of evaluating integral (4.4).

Conventional Lens-Type Collinear Detection It is of interest to compare the above result to the collection efficiency for a conventional LIF arrangement such as the lens-type collinear setup presented in the prior Section 4.2.1. This may be accomplished by considering that the collection solid angle is essentially constant over the detection volume seen by the collection lense (i.e. $\Omega(\mathbf{x}) = \Omega_0 = \text{const}$) so that

$$\Gamma = \int_V I(r, z) \frac{\Omega_0}{4\pi} d\varphi r dr dz = \frac{\Omega_0}{4\pi} \int_{z=-af/D_{\text{lens}}}^{af/D_{\text{lens}}} \int_{r=0}^{\infty} \int_{\varphi=0}^{2\pi} I(r, z) d\varphi r dr dz. \quad (4.8)$$

The inner two integrals corresponds to the radiant power P which is constant along the optical axis z , and the integration along z may as a first order estimate be performed over the depth of field $2af/D_{\text{lens}}$ (a detection aperture, D_{lens} diameter of the lens).

4.4 Results

4.4.1 Collection Efficiency and Detection Volume of Bidirectional Fiber

In Section 4.3 the fiber's excitation and detection distribution were determined, shown in Figure 4.5, so that the resulting detection efficiency Γ may be evaluated for different fiber geometries. It turns out that Γ/P (normalized by the total radiant power P) amounts to $\sim 1 \times 10^{-5}$ m for the fiber dimensions used in experiments presented here

Fiber type	Diameter (μm)	NA	E_{trans} (mJ)	Γ/P (10^5 m)	$E_{\text{trans}}\Gamma/P$ (10^5 mJ m)
LMA-PCF	15	0.04	0.004	0.007	0.00003
SMF	3.5	0.13	0.002	0.005	0.00001
All-silica MSIF	200	0.22	0.5	0.5	0.3
All-silica MSIF	550	0.22	2.2	1.4	3.1
MSIF	400	0.37	0.5	1.7	0.9
MSIF	600	0.37	1.5	2.6	3.9
MSIF	800	0.37	2.9	3.5	10.1
MSIF	1000	0.37	3.9	4.3	16.9

Table 4.1: Threshold transmitted pulse energies E_{trans} and overall detection efficiencies for various fiber types and sizes. Data for E_{trans} corresponds to 150 ps pulses at 532 nm and is adapted from [86]. The normalized detection efficiencies Γ/P for the respective fiber parameters were numerically determined as described in the text.

(NA = 0.22 and diameter $D_{\text{fiber}} = 500\mu\text{m}$). It is of interest to compare this value to the collection efficiency for a conventional LIF arrangement such as the collinear setup presented in Section 4.2.1. This results in $\Gamma/P = 4 \times 10^{-5} \text{ m}$ for the presented optical setup. This implies that we can expect LIF intensities of the same order of magnitude for the lens-type LIF reference experiment as for the fiber probe measurements which is confirmed by results presented below.

Evaluation of integral (4.4) further yields that 50 % of the LIF signal is collected from an area within a distance of 1.0 mm from the fiber endface. This corresponds roughly to the length of the cone of maximum collection solid angle given by $D/2 \tan \theta_{\text{NA}} = 1.1 \text{ mm}$. At the same time 90 % of the LIF photons are collected from an area within 6.4 mm distance from the fiber face. The detection volume and the spatial resolution is hence in the range of several mm and scales as the fiber diameter. Calculations also have shown that the collection efficiency Γ scales linearly with increasing fiber diameter as well as typical numerical apertures NA (multi-mode step index fiber (MSIF) with non-silica cladding NA = 0.37, all-silica MSIF NA = 0.22, single-mode fiber (SMF) NA = 0.13, and large mode-area photonic crystal fiber (PCF) NA = 0.04).

Apart from the fiber diameter's influence on collection efficiency one has to consider that thinner fibers permit less transmitted radiant power P due to the core material's threshold damage. Hence, it can be expected that P is roughly inversely proportional to the square of the fiber diameter D_{fiber} . This leads to the conclusion that the number of detectable fluorescence photons $N_{\text{ph}} \propto P\Gamma$ scales as D^3 . This trend is confirmed by including results of the measurements conducted by Hsu et al. [86] who have investigated damage thresholds of various fiber types and sizes (Table 4.1). The D^3 scaling is confirmed for fibers of which different sizes have been investigated, i.e. the multi-mode fibers. It can also be seen that single-mode and large mode-area photonic crystal fibers, which are both characterized by a small (mode-)core diameter, are less suitable due to their small collection efficiency as well as attainable pulse energy.

4.4.2 LIF OH Detection using Bidirectional Fiber Probe in Harsh Environment

In Section 4.2.1 conventional measurements of the OH concentration and temperature profiles in a stoichiometric methane-air flame were outlined. OH LIF was also performed using the fiber probe technique described above by traversing the fiber endface perpendicular to the flames's symmetry axis. Figure 4.6 shows the OH LIF spectra ($A^2\Sigma - X^2\Pi$ $1 \leftarrow 1$ and $0 \leftarrow 1$ band) for the two LIF arrangements, as well as the non-resonant fiber scattering background (dashed lines). Three conclusions may be drawn: first, the OH LIF spectrum is unaffected by the presence of the fiber probe, meaning that quenching effects are not observed in the spectrum; second, the inelastic fiber scattering, which was the same when the fiber was inside or outside the flame, is exceeded by the OH LIF signal; third, one finds a comparable LIF signal intensity - the conventional LIF spectrum being scaled by factor of 1/2 in the figure - for both optical arrangements as predicted by the above collection efficiency considerations.

The OH concentration gradient was scanned using the fiber probe, the outcome of which is included in Figure 4.2. The OH profile is resolved and in good agreement with the reference experiment. The relatively large error bars of the LIF measurements shown for the fiber in Figure 4.2 (conventional measurement error bars of similar order but omitted for clarity) are due to flame fluctuations and shot-to-shot fluctuations of the laser which could not be corrected for by the averaging power-meter used.

At first glance, it might be surprising that the fiber withstands the excessive flame temperatures. This may be explained by assuming an equilibrium between convective heat transfer $\dot{Q}_{\text{conv}} = \alpha A (T - T_{\text{gas}})$ from the hot product gases to the fiber, and heat losses due to conduction \dot{Q}_{cond} and radiative cooling $\dot{Q}_{\text{rad}} = \varepsilon \sigma A (T^4 - T_0^4)$ (σ is the Stefan-Boltzmann constant). An emissivity of 0.9 has been assumed for fused silica, and the heat transfer coefficient α has been evaluated from a Nusselt number correlation of the flow field (cylinder in cross flow). It turns out that conduction losses are negligible and an equilibrium temperature of $T \sim 1400$ K is found. Nevertheless the physical intrusion of the fiber close to the reaction zone disturbs the flow field and thus the flame cone which causes slightly biased results at low heights.

4.5 Conclusion

Detection of OH LIF has been demonstrated using a bidirectional fiber probe technique with the potential for minimally-invasive measurement under harsh conditions. Reference experiments have been performed (OH-LIF and Raman) in order to characterize a stoichiometric methane-air flame serving as a reference experiment. An optical setup has been presented which permits simultaneous coupling into the fiber and detection of the backscattered fluorescence signal. The detection efficiency and the dimensions of the sample volume have been characterized numerically using geometrical considerations. All-silica optical fibers may be found which are suitable for simultaneous UV-radiation transmission and detection of fluorescence, which is red-shifted beyond the vibrational Raman signature of the fiber (i.e. $> 1000 \text{ cm}^{-1}$). OH LIF was detected and the OH concentration profile in a laminar premixed flame could be reproduced.

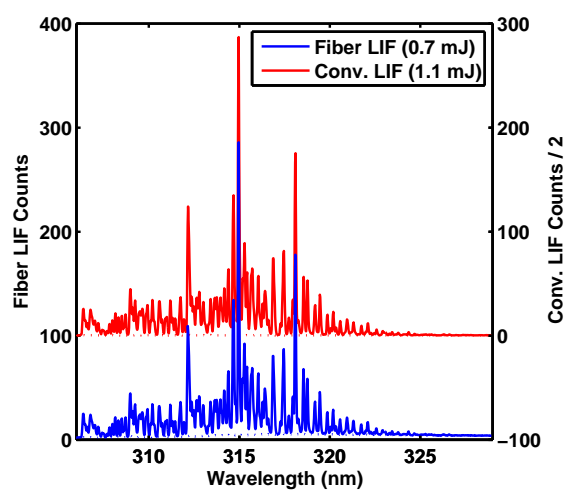


Figure 4.6: OH LIF spectrum of fiber probe and conventional lens-type optical setup LIF spectrum (scaled by a factor of 1/2 and shifted for clarity). The dashed line is the background including chemiluminescence and fiber scattering. For fiber probe LIF measurements a low-OH fiber was used.

Chapter 5

Fuel-Rich Methane Oxidation in a High-Pressure Flow Reactor studied by Optical-Fiber Laser-Induced Fluorescence, Multi-Species Sampling Profile Measurements and Microkinetic Simulations

Abstract

A versatile flow-reactor design is presented that permits multi-species profile measurements under industrially relevant temperatures and pressures. The reactor combines a capillary sampling technique with a novel fiber-optic Laser-Induced Fluorescence (LIF) method. The gas sampling provides quantitative analysis of stable species by means of gas chromatography (i.e. CH_4 , O_2 , CO , CO_2 , H_2O , H_2 , C_2H_6 , C_2H_4), and the fiber-optic probe enables in situ detection of transient LIF-active species, demonstrated here for CH_2O . A thorough analysis of the LIF correction terms for the temperature-dependent Boltzmann fraction and collisional quenching are presented. The laminar flow reactor is modeled by solving the two-dimensional Navier-Stokes equations in conjunction with a detailed kinetic mechanism. Experimental and simulated profiles are compared. The experimental profiles provide much needed data for the continued

This chapter is adapted from the author's version of a manuscript by Heiner Schwarz, Michael Geske, C. Franklin Goldsmith, Robert Schlögl, Raimund Horn, which was accepted for publication in *Combustion and Flame*, Elsevier (<http://www.journals.elsevier.com/combustion-and-flame/>). Changes resulting from the publishing process may not be reflected in this document. A definitive version will be subsequently published in the journal.

validation of the kinetic mechanism with respect to C_1 and C_2 chemistry; additionally, the results provide mechanistic insight into the reaction network of fuel-rich gas-phase methane oxidation, thus allowing optimization of the industrial process.

5.1 Introduction

Owing to the predicted depletion of petroleum reserves, the transformation of natural gas (i.e. methane) into value-added chemical products is of growing interest for the chemical industry. Conventional approaches rely on indirect conversion via synthesis gas production (from steam reforming, CO_2 reforming or partial oxidation), followed by a gas-to-liquid process, but these multi-step processes are particularly capital intensive. Therefore, the direct conversion of methane to ethylene, methanol or formaldehyde is economically more favorable [87, 11].

Oxidative Coupling of Methane (OCM) could be a desirable direct conversion route in which methane is transformed into ethylene under fuel-rich conditions ($CH_4/O_2 = 2 - 8$, or an equivalence ratio $\phi = 4 - 16$) at temperatures around 1000 K and pressures up to 30 bar. It has been suggested in the literature that the OCM reaction proceeds via a homogeneous/heterogeneous coupled mechanism [88, 22]. According to this model, methane is first activated on the catalyst, and the resulting methyl radical desorbs. Two gas-phase methyl radicals combine to form ethane, which is subsequently dehydrogenated to ethylene. In fact, OCM can occur even without a catalysts, albeit with very low selectivity [89, 90, 23, 91]. Although the exact role of oxygen in the homogeneous/heterogeneous mechanism is unclear, it is known that small concentrations of oxygen are necessary for OCM. If the concentration of oxygen is too high, however, the C_2 products will be oxidized, thereby decreasing the yield. Computational engineering will play a key role in the optimization of the reactor design, catalyst choice, and operating conditions. An essential component of this approach includes detailed models that describe the coupling between fluid mechanics and the kinetics of elementary surface and gas phase reactions. The predictive utility of these models depends upon the accuracy of the underlying rate coefficients for the elementary reactions. These kinetic¹ mechanisms are often tested against experimental data taken under low-pressure and/or highly dilute conditions. A more desirable approach would be to validate the mechanisms against data taken under industrially relevant conditions, since it requires less extrapolation, but this approach can work only if the flow field and chemistry can be modeled simultaneously in a rigorous yet computationally efficient manner. This manuscript presents an experimental apparatus designed precisely for this purpose and the accompanying kinetic simulations.

Gas-phase Oxidative Coupling of Methane was studied in a novel, versatile flow reactor designed for spatially resolved kinetic profile measurements under homogeneous (and/or catalytic) conditions, with temperatures up to 1300 K and pressures up to 45 bar [92]. The reactor features a sampling capillary through which a small fraction of the reacting gas mixture is transferred to quantitative gas analytics, e.g. a mass spectrometer (MS) or a gas chromatograph (GC). Complementarily, a recently developed fiber-optic Laser-Induced Fluorescence (LIF) method [93] was applied for in situ detection of CH_2O , which is an important intermediate in the oxidation process. It is worth emphasizing that the reactor does not require optical viewports; optical access

¹Mechanisms of elementary rate constants are commonly referred to as “microkinetic” in the catalysis community, whereas the preferred term in gas-phase chemistry is “detailed kinetics” or “elementary kinetics”.

is provided only via the novel fiber-optic LIF probe. This technique is of particular interest for applications where optical access is limited (e.g. high-pressure reactors or internal combustion engines).

Section 5.2.1 describes the experimental design of the profile reactor, in particular the sampling process as well as the temperature and species analysis. Section 5.2.2 outlines the optical setup of the fiber-endoscopic LIF method, and Section 5.2.3 details the corrections necessary to derive relative concentration measurement from the LIF data, including collisional quenching and the temperature-dependence of the excited state populations. Section 5.3 describes the reactor modeling using Computational Fluid Dynamics (CFD) and the required reduction procedure of the kinetic mechanism. In Section 5.4 the results of experiment and simulation are presented and discussed, followed by a kinetic description of the elementary reaction steps.

5.2 Experimental Methods

5.2.1 Profile Reactor Measurements

A detailed description of the reactor design is given in [92]; the essential features of the profile reactor are schematically summarized in Figure 5.1. The flow reactor consists of a cylindrical fused-silica tube of 18 mm inner diameter and 10 mm thick walls. It is enclosed by an electrical furnace (not shown in the drawing), the temperature of which is monitored using a thermocouple. The gas flow is regulated by calibrated mass-flow controllers for CH_4 , O_2 , and Ar/He mixture (8 vol-% He in Ar, serving as internal standard and carrier gas for the analytics).

Sampling of the reacting gas mixture is accomplished by means of a fused-silica capillary (outer diameter 652 μm). The capillary is translated along the reactor axis allowing continuous sampling of the reacting gas mixture and thus a determination of the chemical composition as a function of position. A K-type thermocouple can be inserted in the capillary void, additionally providing information about the axial temperature profile. An α -alumina foam (80 pores per linear inch) provides mechanical stability for the sampling capillary and allows efficient preheating of the gas stream prior to entering the free gas-phase region. The sampling rates (~ 10 ml/min) are adjusted such that they are considerably smaller than the total flow rate, so that (i) the flow remains largely unaffected from the sampling and (ii) the sampling volume remains small. It was verified experimentally and numerically (i.e. by CFD simulations of the sampling process) that the spatial resolution is on the order of several hundreds of microns so that profile gradients are not limited by the spatial resolution of the technique.

When probing a reacting gas mixture one has to ensure rapid quenching of the chemical reaction in order to achieve an unbiased measurement at the probing position. This may be assured if either (i) the sampling time is short compared to changes in chemical composition (i.e. rapid extraction), or if (ii) heat or radical removal by collisional wall-quenching inhibits reaction progress. In our experiments, the reaction timescale is on the order of 0.1 s while sampling occurs on a slightly shorter timescale, so that the first condition may not suffice to justify unbiased sampling. However, quenching distances of ~ 1 mm between silica walls, even when maintained at 1000 K, are generally sufficient to suppress a reaction [68]. Since in the present experiment the wall distance inside the capillary is much smaller (~ 100 μm) it can be assumed that thanks to wall-quenching (i.e. by radical recombination) an unbiased composition of

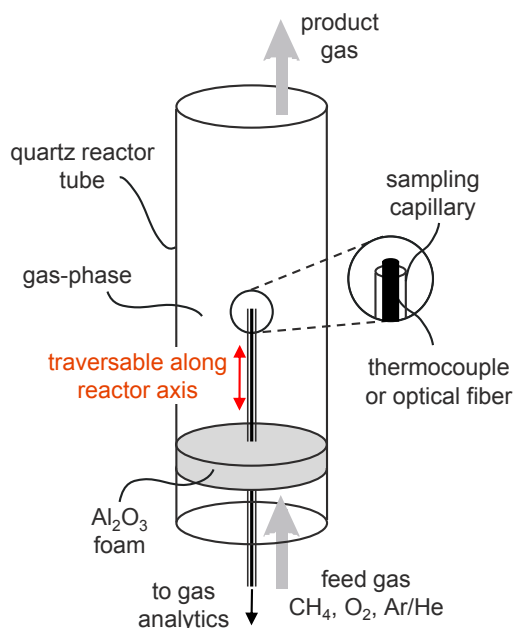


Figure 5.1: Reactor design. The electrical furnace enclosing the reactor is omitted for clarity.

the reaction gas is analyzed.

The sampled gas is transferred to a mass spectrometer for online monitoring of the reaction. Additionally, quantitative detection of the stable gas-phase species is attained by a micro gas-chromatograph (Varian, model CP-4900). The micro-GC consists of two columns: a Molsieve 5 A column for the permanent gases He, CH₄, O₂, H₂, and CO using Ar as carrier, and a PPU column for CO₂ as well as the three C₂ compounds – C₂H₆, C₂H₄ and C₂H₂ – with He as carrier. H₂O was removed from the gas stream before entering the gas chromatograph with a membrane particulate/water filter (Genie 170 from A+ corporation), since the micro-GC has to be operated below 100 °C in order to separate He and H₂. Consequently, water has to be calculated from the oxygen balance. All gases were calibrated against the internal standard prior to the experiment. On yet another column, C₃H₈ and C₃H₆ were detected but these gases were not calibrated. The experimental error originates mainly from the mass flow controllers with approximately 2% per gas species for a typical flow rate used (0.1 % of max. value + 0.5 % of current value). The overall error of the gas-chromatograph is better than 1 %. The carbon and hydrogen balances close to more than 95 %, although minor species such as oxygenates were not calibrated.

5.2.2 Fiber-Optic LIF Detection of CH₂O

Formaldehyde (CH₂O) is an important reaction intermediate in hydrocarbon oxidation. In combustion environments it can be observed in the preheating zone upstream

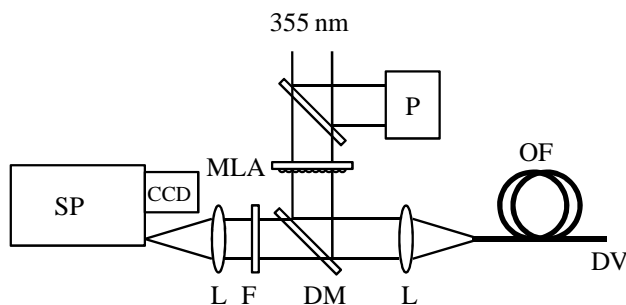


Figure 5.2: Schematic representation of the optical setup for bidirectional fiber coupling and fluorescence detection: DM dichroic (longpass) mirror, L lens, MLA micro-lens array, P power-meter, OF optical fiber, F glass filter, SP spectrometer, DV detection volume.

the flame front. Under partial oxidation conditions, it is a major intermediate in the undesired CO pathway [91, 94], which will also be seen in Section 5.4.3.

In order to quantify CH_2O concentrations experimentally, the extracted gas sample has to be heated so that CH_2O does not condense along with water in the tubing. However, such heating is not always practical; indeed, the micro-GC used in this experiments requires water (and in turn CH_2O) to be removed from the gas sample before entering the GC. Alternatively, *in situ* Laser-Induced Fluorescence (LIF) constitutes a sensitive optical technique for CH_2O detection. Even though this approach is rather intricate and involved, it has to be pointed out that LIF may also be applicable to species which cannot be extractively sampled (such as radical species). Therefore, in the context of this study, the LIF study has to be regarded as a proof-of-concept for setups in which conventional optical access is excluded.

Recently, we demonstrated the use of a novel technique permitting LIF detection in harsh environments using a single bidirectional optical fiber probe [93]. Since the reactor does not provide optical view-ports advantage is taken of the fact that the sampling capillary may (alternatively to the thermocouple) accommodate an optical fiber and thus provides optical access (magnification in Figure 5.1). Figure 5.2 shows the setup adapted for bidirectional coupling of the excitation laser and fluorescence detection using an optical fiber. 1 mJ/pulse of the third harmonic of a Q-switched Nd:YAG laser (Spectra-Physics, Quanta-Ray PRO) are coupled into the fiber to excite the 4^1_0 band (i. e. the out-of-plane bending vibration) of the CH_2O $A^1A_2 \leftarrow X^1A_1$ transition around 355 nm. The laser line was measured with a grating spectrometer and found at $28183.46 \pm 0.10 \text{ cm}^{-1}$ with a FWHM of 1.8 cm^{-1} . To prevent optical damage of the fiber's end-face a micro-lens array (MLA in Figure 5.2) serves to homogenize the focal beam waist. Fluorescence is excited in the detection volume (DV) at the tip of the fiber and emitted isotropically so that a portion is again captured by the fiber. The signal is transmitted by the long-pass dichroic mirror (DM) and analyzed in a fiber-coupled spectrometer (SP). Strong Fresnel reflections of the laser-line and low wavenumber Raman scattering of the fiber are suppressed by an additional GG395 Schott glass filter. Since the CCD camera does not allow fast gating 100 shots are accumulated on the chip before reading out the spectrum. The average pulse energy is monitored using a power-meter (P).

Step-index multimode fibers made of fused silica (SiO_2) with fluorine-doped claddings are commercially available. Being high-temperature resistive, at the same time they possess high damage threshold intensities thus being suitable for UV laser transmis-

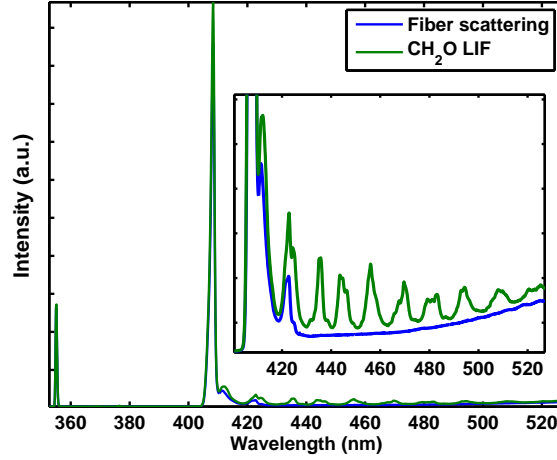


Figure 5.3: Backscattering spectrum of the optical high-OH fiber (blue) and ex situ CH_2O laser-induced fluorescence spectrum acquired through the fiber (green). The strong peak at 409 nm is attributed to the fiber's OH-stretch Raman peak ($\sim 3700 \text{ cm}^{-1}$). The inset clearly shows the characteristic CH_2O fluorescence superimposed on the fiber's Raman feature. The residue of the 355 nm laser line is seen while the spectral region up to 405 nm is filtered out by the dichroic mirror.

sion. There are two types of fused-silica fibers, characterized by their OH-content originating from the manufacturing process, commonly referred to as high-OH and low-OH. The fiber material's inherent, fabrication-induced impurities and defects may lead to undesired fluorescence, additional Raman bands, color-center formation, and photodegradation effects [82, 83, 84, 85]. Stimulated Raman scattering and non-linear effects become important only for long fibers or higher laser intensities [84]. Low-OH fibers are prone to strong broadband fluorescence at 355 nm excitation, thereby rendering them inappropriate for the current application. High-OH fibers show better UV-transmission characteristics, and it has been shown that the back-scattering spectra of high-OH fibers are characterized by the Raman signature of vitreous fused silica featuring phonon and defect bands at wavenumbers $< 1200 \text{ cm}^{-1}$, as well as a dominant peak around 409 nm which is to be attributed to the Raman band of the OH-groups stretching mode (Raman shift $\sim 3700 \text{ cm}^{-1}$), see Figure 5.3 and reference [93]. No spectral features are observed at longer wavelengths, so that this spectral window may be used to detect the CH_2O fluorescence signal (inset in Figure 5.3).

It is necessary to comment on the spatial resolution of the fiber-LIF technique. In the following we present an analytical expression for the intensity and collection efficiency distribution at the fiber tip and derive an instrumental function that will be used later in the profile measurements. First, recall that an expression for the number of fluorescence photons N_{ph} generated upon pulsed laser-excitation in the linear regime is given by

$$N_{\text{ph}} = \frac{B_{12} I_{\nu} \tau}{c} n V f_{\text{B}} A_{21} \tau_{\text{eff}} \frac{\Omega}{4\pi} \quad (5.1)$$

where for simplicity a two-level system is assumed, and B_{12} is the Einstein coefficient of absorption (in $\text{m}^3 \text{ Hz J}^{-1} \text{ s}^{-1}$), I_{ν} is the spectral irradiance of the laser (in W m^{-2}

5.2. Experimental Methods

Hz^{-1}), τ is the pulse length (in s), c the speed of light, n is the number density of the probed molecule (in m^{-3}), V is the detection volume (in m^3), f_B is the fraction of molecules in the rovibronic level being excited, $A_{21} = 1/\tau_{\text{rad}}$ is the Einstein coefficient for spontaneous emission (in s^{-1}) with radiative lifetime τ_{rad} , τ_{eff} (in s) is the effective lifetime of the laser excited state accounting for non-radiative decay (quenching and predissociation), and Ω is the collection solid angle.

Equation (5.1) holds for a differential volume dV and hence the total number of fluorescence photons collected for an arbitrary optical system is found by spatial integration

$$N_{\text{ph}} = \int_V dN_{\text{ph}} = \int_V \frac{\partial N_{\text{ph}}}{\partial V} dV \quad (5.2)$$

where $\partial N_{\text{ph}}/\partial V = B_{12} I_\nu \tau c^{-1} n f_B A_{21} \tau_{\text{eff}} (\Omega/4\pi)$ is readily found from Equation (5.1). For convenience we only consider the irradiance I instead of the spectral quantity I_ν in what follows. In a chemically homogeneous environment the only parameters showing a spatial dependence are $I(\mathbf{x})$ and $\Omega(\mathbf{x})/4\pi$. It is convenient to assume cylindrical coordinates $\mathbf{x}(r, \varphi, z)$ so that we can define the detection efficiency

$$\Gamma := \int_V I(\mathbf{x}) \frac{\Omega(\mathbf{x})}{4\pi} d\varphi r dr dz \quad (5.3)$$

as a quantitative measure for the number of collected photons for different optical setups.

Neglecting absorption and saturation in the present derivation, $I(\mathbf{x})$ and $\Omega(\mathbf{x})$ follow from purely geometrical considerations. This is most conveniently understood by referring to Figure 5.4. Figure 5.4 (a) shows the radiation field $I(\mathbf{x})$ in cylindrical coordinates, which is in a first approximation deduced in terms of a r^{-2} law. The irradiance distribution $I(\mathbf{x})$ is normalized by the laser power P , resulting in units m^{-2} . On the other hand the solid angle of an arbitrary surface S seen from a point \mathbf{x} in space may be defined as

$$\Omega(\mathbf{x}) = \int_{S(\mathbf{x}')} \frac{\mathbf{X}/X \cdot \mathbf{n}_S dS}{X^2}. \quad (5.4)$$

The integration is performed over $S(\mathbf{x}')$ where $\mathbf{n}_S = \mathbf{n}_S(\mathbf{x}')$ denotes the surface normal unit vector of the surface element dS at position \mathbf{x}' and $\mathbf{X} := \mathbf{x} - \mathbf{x}'$. The distance vector \mathbf{X} may also be interpreted as an optical ray from a point \mathbf{x} to the surface element $dS(\mathbf{x}')$ and in the present consideration the surface S obviously corresponds to the fiber end-face. Optical rays impinging on the surface at an angle which is greater than the critical acceptance angle of the optical fiber θ_{NA} are reflected and cannot contribute to the effective collection solid angle. In mathematical terms this condition is expressed in terms of the angle $\angle(\mathbf{X}, \mathbf{n}_S(\mathbf{x}'))$, i.e. only if $\angle(\mathbf{X}, \mathbf{n}_S(\mathbf{x}')) < \theta_{\text{NA}}$ does the surface element $d\mathbf{x}'$ contribute to the integration. Thus, we may rewrite Equation (5.4) as a conditional integral:

$$\Omega(\mathbf{x}) = \int_{S(\mathbf{x}')} \frac{\mathbf{X}/X \cdot \mathbf{n}_S dS}{X^2} \quad \angle(\mathbf{X}, \mathbf{n}_S(\mathbf{x}')) < \theta_{\text{NA}} \quad (5.5)$$

The result is shown in Figure 5.4 (b). Quantification of $I(\mathbf{x})$ and $\Omega(\mathbf{x})$ now allows for quantitative determination of the effective detection volume and the collection efficiency Γ by means of integral (5.3). In particular, we will need

$$\gamma(z) := \int_0^{2\pi} d\varphi \int_0^\infty r dr I(\mathbf{x}) \frac{\Omega(\mathbf{x})}{4\pi} \quad (5.6)$$

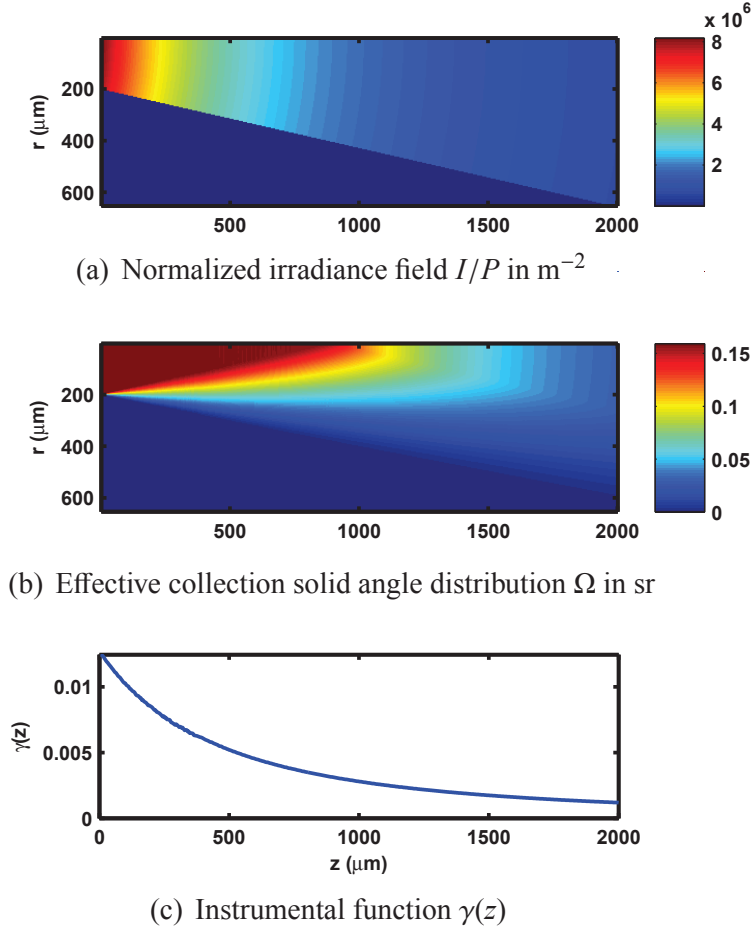


Figure 5.4: (a) Normalized irradiance field I/P , and (b) effective collection solid angle distribution Ω in cylindrical coordinates (r and z). The instrumental function $\gamma(z)$ for the optical fiber probe is shown in subfigure (c). Fiber parameters: numerical aperture $\text{NA} = 0.22$ and diameter $D_{\text{fiber}} = 400 \mu\text{m}$.

which serves as the instrumental function for the optical fiber measurements presented here. $\gamma(z)$ is shown in Figure 5.4 (c) and will be used to deconvolute the measured LIF profiles (cf. Section 5.4.1).

5.2.3 LIF Corrections

The preceding discussion suggests that some comments are in order on the likelihood of saturation effects. From the intensity distribution in Figure 5.4 (a) it can be seen that the maximum value for the normalized intensity I/P amounts to $8 \cdot 10^6 \text{ m}^{-2}$. Recalling a per-pulse-power P of roughly $1 \text{ mJ}/10 \text{ ns} = 0.1 \text{ MW}$ and a linewidth of 1.8 cm^{-1} , the spectral intensity is found to be on the order of $I_\nu = I/\Delta\nu = 8 \cdot 10^6 \text{ m}^{-2} \times 0.1 \text{ MW}/1.8 \text{ cm}^{-1} \sim 10^8 \text{ W/cm}^2 \text{ cm}^{-1}$. It is thus unlikely that saturation has occurred in the present experiment since this value is significantly lower than saturation inten-

5.2. Experimental Methods

sities reported by other authors [95, 96]. In retrospect, this justifies the linear regime assumption implied by Equation (5.1).

In view of making concentration profile measurements, two terms in Equation (5.1) need further consideration, namely the ro-vibrational Boltzmann population of the laser-coupled lower state and collisional quenching effects. Both will be discussed in the following paragraphs.

The portion of molecules in the lower laser-coupled state can be approximated assuming the molecule ensemble to be in thermodynamic equilibrium, i.e. the population distribution is described by the temperature-dependent Boltzmann fraction $f_B(T)$. It may be calculated with a statistical mechanical formulation based on fundamental well-established molecular parameters. Boltzmann fractions may be evaluated independently for the vibrational and rotational energy modes, $f_B(T) = f_{\text{vib}} f_{\text{rot}}$. The vibrational partition function Z_{vib} is expressed as a product over the vibrational energies ν_i [30],

$$Z_{\text{vib}} = \prod_{i=1}^{3n-6} \left(1 - \exp \frac{-h\nu_i}{k_B T} \right)^{-1} \quad (5.7)$$

where the product for the planar CH_2O is over the six vibrational normal modes with frequencies ν_1, \dots, ν_6 [97, 98]. The population of the vibrational ground state reduces to $1/Z_{\text{vib}}$ and is plotted as a function of temperature in Figure 5.5 (a). In the temperature range relevant for this study (600 - 1200 K) the ratio of maximum to minimum value for f_{vib} is ~ 2 ; this ratio is also given in parenthesis in the figure and will serve as a measure for the temperature-sensitivity of the different correction terms. Subsequently, this ratio will be referred to as sensitivity-factor and will be determined for the rotational population variation as well as the quenching term so that a quantitative comparison of the terms is possible.

The rotational structure of the formaldehyde molecule is correctly represented by an asymmetric top. Fortunately the asymmetry is only slight, and therefore in good approximation its energy level structure can be described by a symmetrical top where an algebraic expression for the rotational states may be found. The rotational term values in the rigid rotor approximation of the prolate symmetrical top are

$$E_{J,K}/hc = \tilde{B} J(J+1) + (A - \tilde{B}) K^2 \quad (5.8)$$

where J is the total angular momentum quantum number, K its component along the molecule's symmetry axis, $A > B > C$ are the rotational constants and $\tilde{B} = 1/2(B + C)$ [99, 97]. Due to the dense structure of the formaldehyde spectrum and the relatively broad excitation linewidth of the multimode laser, several transitions contribute [100]. From the tabulations provided by Dieke and Kistiakowsky it could be established that four transitions of the pP -branch are excited, and their line intensities are described by the Hönl-London formula for \perp bands [99, 31]

$$B_{J,K}^{pP} = \frac{(J+K-1)(J+K)}{J(2J+1)} \quad (5.9)$$

so that the overall absorption intensity is proportional to the weighted sum of the individual lines

$$f_{\text{vib}} \sum_{\{J,K\}} B_{J,K}^{pP} \frac{g_{KJ} \exp \frac{-E_{J,K}}{kT}}{Q_{\text{rot}}} \quad (5.10)$$

where g_{KJ} is the rotational-nuclear spin statistical weight for the state $\{J, K\}$ so that the latter term represents the Boltzmann fractions for the individual rotational states (Figure 5.5 (b)). Again, the sensitivity-factor of the rotational population temperature-dependence in the relevant temperature range is determined as the ratio of maximum to minimum value and amounts to ~ 2 (again given in parenthesis for each rotational state in the figure). The temperature dependence of the overall absorption over the relevant temperature range is plotted in Figure 5.5 (c). We note that both vibration and the rotation contribute comparably to the Boltzmann temperature-dependence and that the overall sensitivity-factor is roughly 4.

The effective lifetime of the laser excited state(-manifold) $\tau_{\text{eff}} = (A + Q)^{-1}$ is related of to the collisional quenching rate Q . The quenching rate $Q = \sum_i n_i \sigma_i v_i$ in turn is a function of composition n_i , the quenching cross-section σ_i and the relative molecular velocity $v_i = f(T)$ of all possible collision partners. Though Harrington and Smyth [95] state that the Boltzmann dilution is by far the larger correction term, the body of literature of fundamental quenching parameters in the appropriate temperature, pressure and composition space is rather scarce. Several groups [101, 102, 103, 100, 104] have measured effective fluorescence lifetimes τ_{eff} in flames and generally find a monotonically decreasing lifetime along the reaction coordinate, roughly described by a T^{-1} relation. Correction for this effect effectively leads to a downstream shift of the measured CH_2O profile with respect to the LIF signal. In those studies, ratios of maximum to minimum lifetimes and thus the sensitivity-factor to this correction term ranges between 2 - 3, while the temperature gradients spanned more than 1000 K accompanied by the drastic composition change characteristic for flames. With respect to the present experiment, the temperature gradient is smaller (~ 500 K), and also the composition change is moderate due to the dominating methane content. It may thus be expected that the lifetime correction term here is on the same order or smaller and in first approximation may be described by a $\tau_{\text{eff}} \propto T^{-1}$ relation.

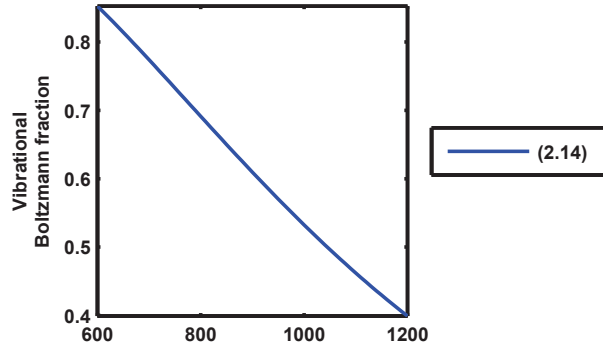
Summing up the preceding section, it is now possible to compare the effect of the two correction terms and it can be seen that the overall Boltzmann factor is indeed the larger contribution compared to the quenching term. The sensitivity to the latter can be expected to be smaller than 2 while the Boltzmann correction term sensitivity factor was roughly twice as large. While an expression for the Boltzmann variation has been derived (Figure 5.5 (c)), we will assume $\tau_{\text{eff}} \propto T^{-1}$ for the quenching effect; the influence of the correction terms on the measured profiles is discussed in Section 5.4.

5.3 Kinetic Reactor Simulations

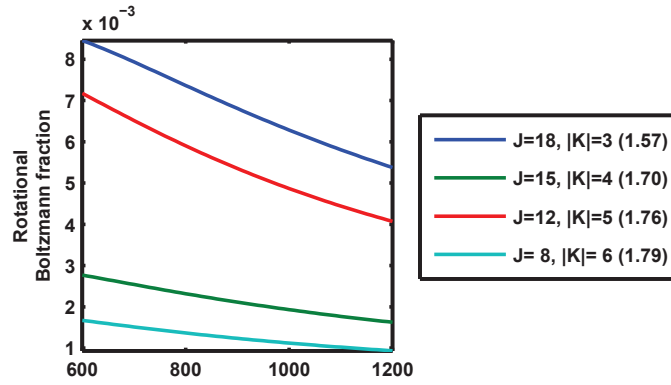
The challenge in reacting flow simulations is to describe accurately the coupled transport and chemistry phenomena. The present section discusses two important aspects of the detailed chemical kinetic simulations performed: (i) reduction of the elementary kinetic mechanism as a prerequisite for computational feasibility, and (ii) comprehensive modeling of the flow reactor by means of detailed kinetic Computational Fluid Dynamics (CFD).

5.3.1 Mechanism Reduction

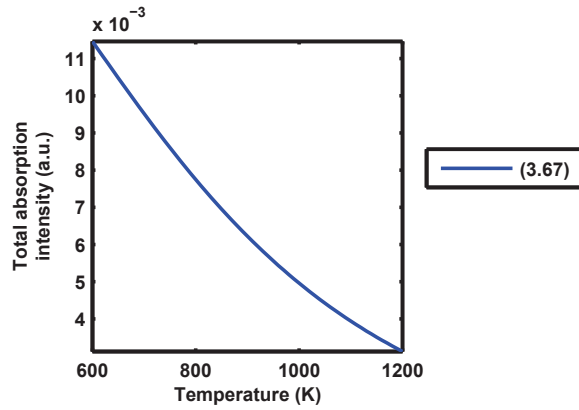
In a literature review of available detailed kinetic mechanisms for fuel-rich methane oxidation conditions characteristic for OCM – the study will be described in a forthcoming paper by the authors – it was found that the mechanism reported by Dooley et



(a) Boltzmann population of the excited vibrational ground state $f_{\text{vib}}(T)$



(b) Boltzmann population of rotational states $f_{\text{rot}}(T)$ contributing to the LIF signal



(c) Total absorption intensity as in equation (10)

Figure 5.5: Temperature dependence of the vibrational ground state population f_{vib} (a), the rotational state population f_{rot} (b), and total absorption intensity (c). As a measure for the correction effect the ratio of maximum to minimum values are given in parenthesis.

al. [5] performs most satisfactorily; this conclusion is drawn from the comparison of a set of experimental reactor profiles to kinetic simulations. Therefore this mechanism was employed in the present investigation. It is a comprehensive kinetic mechanism including H_2 , C_1 , C_2 , C_3 and C_4 oxidation chemistry. Broadly speaking, it consists of two sub-mechanisms: a small-molecule mechanisms by Li et al. [105] for synthesis gas combustion, and a larger mechanism for C_1 - C_4 oxidation and pyrolysis by Healy et al. [106]. The dependence of many elementary steps on pressure is considered and third-body efficiencies of many species are included.

Mechanism reduction is often indispensable in CFD simulations of chemically reacting flow. In fact, the commercial CFD software used in the present work, FLUENT, is hard-coded for a maximum of 50 species, and the mechanism by Dooley et al. has nearly 300 species. Fortunately, the vast majority of those species are irrelevant for fuel-rich methane oxidation under conditions relevant to this study, due to the consecutive nature of the reaction. From a chemical perspective, the 50-species limit is completely arbitrary; nonetheless, in order to determine the “50 most important species” for the present problem, the mechanism was reduced as follows. First, the experimental conditions were simulated using the Plug-Flow Reactor model (PFR) implemented in CHEMKIN², since this model allows for first-order sensitivity analysis of the species with respect to the rate coefficients. Sensitivity analysis was performed for each of the eight target species that were quantitatively detected: CH_4 , O_2 , H_2 , H_2O , CO , CO_2 , C_2H_6 and C_2H_4 . For each of these species, the reactions were sorted according to the absolute value of the sensitivity coefficients (in descending order). Next, each species in the mechanism was ranked according to its position in the list of sorted reactions; for example, each species in the first reaction was given a score of 1, and each species in the second reaction was given a score of 2 (assuming that those species were not also in the first reaction). Once this process had been repeated for all target species, the scores for all the species in the mechanism were summed, and the 49 species with the lowest scores were retained. Ar was forced to be the 50th species, since it served as internal standard in the experiments but does not occur in any reaction. Another reason for using Ar as 50th species was that all numerical rounding errors as well as errors from the mixture averaged diffusion treatment were lumped in the Ar mass fraction. The process was repeated for CH_4/O_2 feed ratios ranging from 4, 8 and 16, temperatures at 700 and 1100 K, and pressures of 1 and 8 bar. An alternative approach is to use the absolute flux through each reaction, rather than its sensitivity coefficient. The process above was repeated using the flux-based approach. The two methods were in close agreement regarding the most important species, with the top 41 species being identical. Where the two approaches differed, the sensitivity-based approach tended to favor smaller oxygenates, whereas the flux-based approach tended favor larger unsaturated hydrocarbons. A detailed comparison of the two reduction methods with other more established mechanism reduction methods is beyond the scope of the present work but will be the subject of a forthcoming manuscript. For simplicity, we have adopted the sensitivity-based method for the remainder of this work. The reduced mechanism is appended as Supplemental Material, with the different species between the two methods highlighted.

Using the Cylindrical Shear-Flow Reactor model (CSFR) in CHEMKIN the appropriateness of the mechanism reduction was verified. Shown in Figure 5.6 is the comparison between the complete and the reduced mechanism based on the CSFR center-line profiles (solid and dashed line respectively). The mechanism reduction results in

²REACTION DESIGN© CHEMKIN 10111

a slight upstream shift of the profiles, but all species concentrations are reproduced within a minor error. Although the 50-species limit is arbitrary, it can be stated that the disadvantage of the mechanism reduction is outweighed by the benefits of the detailed CFD simulations as will be outlined below.

5.3.2 Reactor Modeling

The complete set of steady-state, laminar Navier-Stokes equations was solved using the finite-volume implementation of the FLUENT software package³ with the CHEMKIN-CFD package for detailed kinetics⁴. The two-dimensional axisymmetric simulation domain comprises the reacting fluid zone as well as the silica reactor walls and the sampling capillary. The fluid physical properties of the individual gas-phase species are calculated based on kinetic theory expression, and polynomial coefficients for the temperature-dependent thermal conductivity of the fused-silica bodies were taken from the literature [107]. Diffusion was modeled based on the mixture-averaged approach. The only boundary conditions imposed are the fluid inlet conditions and the outer wall temperature. Inlet flow properties are assumed constant over the radius, which is experimentally assured by the foam at the flow inlet. Note that the sampling capillary imposes another no-slip condition in the reactor center, which leads to an annular flow profile. The computational domain was meshed using rectangular cells of uniform dimensions. Throughout the computational process the grid spacing of the fluid zone was gradually reduced down to 0.1 mm until no significant changes in the species contours could be observed. In the radial direction the fused-silica reactor wall was meshed with 1 mm spacing while the central capillary was radially subdivided into 2 equally sized cells. A steady-state solution was attained with residuals below 10^{-5} .

The Reynolds number, Re , is on the order of 100 so that laminar flow conditions can be assumed. The Péclet numbers for energy and mass transport $Pe_T = Lu/\alpha$ and $Pe_i = Lu/D_i$ are on the order of 50 and 20, respectively. Here, L is the characteristic length given by the extension of reaction zone (~ 10 mm), u the annular flow velocity (~ 0.1 m/s), α the thermal diffusivity ($\sim 2 \cdot 10^{-5}$ m²/s), and D_i represents the diffusion coefficients of species i ($\sim 5 \cdot 10^{-5}$ m²/s for H₂). The Péclet number derives from dimensional analysis and compares the convective and diffusive terms in the energy and species' mass conservation equation. If the Péclet number is substantially greater than unity, then it is assumed that axial diffusion is negligible compared to convection and may be omitted from the transport equations. Neglecting the diffusion term changes the system of partial differential equations from elliptic to parabolic, which has substantial implications for numerical solution. For the present problem of chemically reacting flow in a tube, this simplification is known as the boundary-layer model [38], and it is implemented in CHEMKIN as the Cylindrical Shear-Flow Model (CSFR)[39]. Using the boundary-layer model has the advantage that detailed kinetics can be implemented at reasonable computational costs, whereas full Navier-Stokes simulations with a comprehensive kinetic mechanism easily become computationally intractable on a workstation.

However, for laminar flow with a parabolic velocity profile, reliance on the Péclet number can be misleading. Due to the no-slip condition the local Péclet number is smaller than unity close to the wall. In order to scrutinize the impact of the simplifying assumptions made by the CSFR model, CHEMKIN CSFR simulations were compared

³ANSYS© Academic Research CFD, Release 14.5

⁴REACTION DESIGN© CHEMKIN-CFD for FLUENT Module 20112

with a complete Navier-Stokes simulation in FLUENT for identical geometrical and thermal boundary constraints, i.e. a parabolic flow with constant boundary temperature. Figure 5.6 shows the respective center-line profiles (dashed line CHEMKIN CSFR and dotted line FLUENT). It is seen, that the CSFR is an excellent approximation to the full Navier-Stokes solution for the conditions of interest, but the center-line profiles for the full solution are shifted upstream compared to the CSFR model, while the gradients themselves do not change. This result can be rationalized as follows: The fact that the CSFR assumption breaks down close to the wall leads to the axial shift. The radical chain branching reactions are thermally initiated, and these reactions first occur closest to the walls. Subsequently, diffusive (radical) species generated within the boundary layer can diffuse back upstream, which causes the profile shift. The fact that the profile gradients are conserved reflects that diffusive transport in the reactor center, where the flow velocity is higher, is negligible, as implied by the Péclet numbers stated above. If diffusion effects were strong one would expect dispersion of the profile gradients. These observation is analogous to findings in the context of simulations of a honeycomb channel in a catalytic combustion study [108].

Though we have seen that the CSFR model represents an excellent approximation to the the full Navier-Stokes solution in an empty tube, it is expected that its shortcomings will become more important when the full reactor geometry, including reactor wall and the second no-slip conditions due to the sampling capillary, are introduced into the model, in addition to the diffusion effect. Generally, profile shifts of 5-10 mm were observed under our conditions, while the profile gradients were retained.

5.4 Results and Discussion

5.4.1 CH₂O LIF Profile Measurements

Figure 5.7 shows fluorescence spectra upon 355 nm excitation with the optical probe anchored at different axial positions in the reactor. The spectra were corrected for the fiber background. Comparison with the reference spectrum, which was taken in the vapor phase over a formalin solution (dotted line), provides confirmation of formaldehyde detection. The vibrational bands observed are attributed to transitions in the CO stretch and the out-of-plane bending vibrations, designated $2^0_n 4^1_m$ ($n, m = 0, 1, 2, \dots$) with respect to the notation by Clouthier and Ramsay [97]. At the same time a changing broadband background is noticeable, the origin of which could not be unambiguously identified but might be attributed to fluorescence of polyaromatic hydrocarbons (PAH). It was shown by Metz et al. [109] and Brackmann et al. [110] that the spectral features of CH₂O fluorescence do not change significantly with temperature or pressure. Therefore, in order to extract the desired concentration information from the spectra a least-square fitting analysis was applied, in which the experimental spectra $s(\lambda)$ were fitted to the superposition of the scaled reference spectrum $r(\lambda)$ and a third order polynomial $p_3(\lambda)$ representing the broadband background,

$$s(\lambda) = C r(\lambda) + p_3(\lambda). \quad (5.11)$$

A good match of the fitting procedure is attained, which is shown in the inset of Figure 5.7. The scaling constant C is taking as a measure for the CH₂O concentration and the resulting LIF profile as function of the fiber tip position is shown in Figure 5.8.

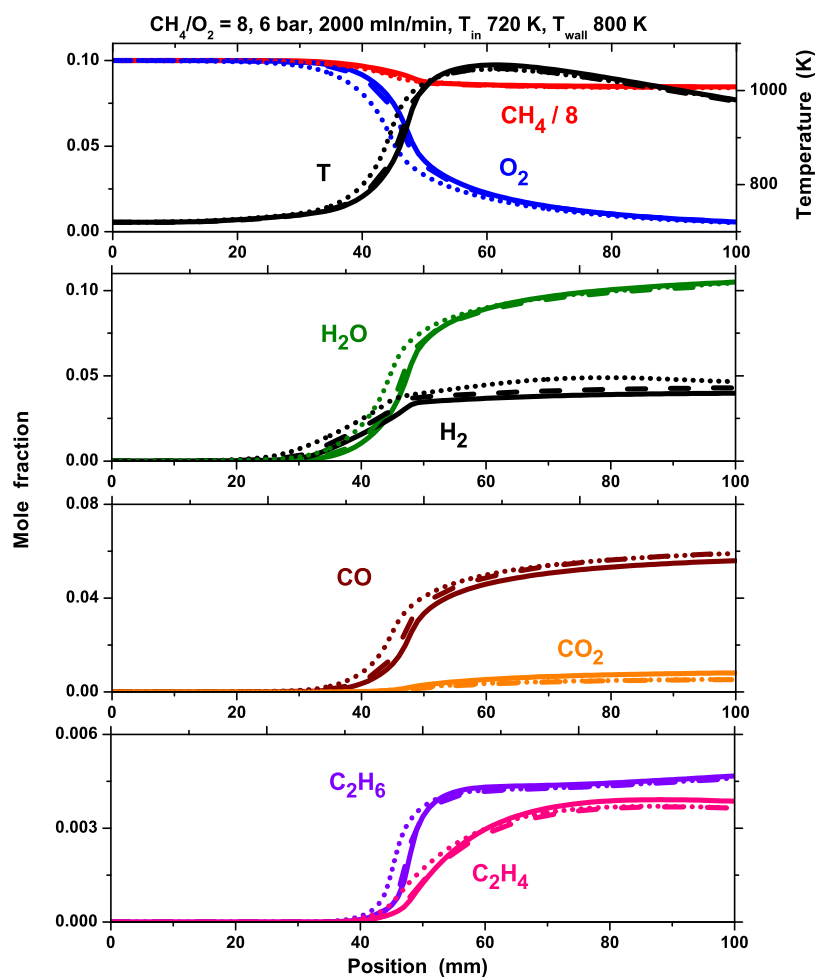


Figure 5.6: Simulated temperature and speciation profiles. The solid and dashed lines are CHEMKIN CSFR simulation results using the complete and the reduced Dooley mechanism respectively; the dotted line is the FLUENT CFD simulation also based on the reduced Dooley mechanism. Conditions correspond to a CH_4/O_2 feed ratio of 8, 6 bar pressure, and a total flow rate of 2000 ml/min in a tubular flow reactor with a constant boundary temperature of 800 K.

As discussed in Section 5.2.2, the LIF signal is integrated over a finite volume ahead of the fiber tip. Mathematically speaking the LIF signal is a convolution of the CH_2O concentration and the instrumental function of the LIF fiber probe. In fact, the instrumental function was derived analytically above and is given by $\gamma(z)$ (Figure 5.4 (c)). The deconvolution was performed, the resulting profile of which is presented in Figure 5.8. As expected, the CH_2O profile is shifted downstream with respect to the raw LIF data.

As outlined in Section 5.2.3, validation of the CH_2O profiles requires correction for the temperature-dependent Boltzmann fraction and collisional quenching. An analytic expression was derived for the former whereas the impact of the latter can in first approximation be described by a $\tau_{\text{eff}} \propto T^{-1}$ relation. Rather than correcting the measured signal, which would in turn require temperature measurements and introduce additional statistical or systematic experimental errors, the simulation results were corrected so as to yield a computed fluorescence signal, an approach proposed by Connelly et al. [111]. In anticipation of the simulation results the experimental CH_2O LIF profile along with the CH_2O profile is presented in Figure 5.8. The effect of both the Boltzmann and quenching correction can be seen. It is found that both correction terms leads to significant shifting and contour change of the profiles. However, as will be seen in the next section, on the global scale of reactor profile measurements the effect is of minor importance and certainly not to be held responsible for the observed offset between experimental and numerical data.

5.4.2 Species Profiles

A set of experiments was performed by varying pressure (1 - 8 bar), composition (CH_4/O_2 4 - 16) and flow rate (2000 - 4000 ml_n/min); the findings were all in qualitative agreement so that general features of the reaction could be isolated. Here we present a representative experiment that was performed with a CH_4/O_2 feed ratio of 8 (C/O atom ratio of 4), at 6 bar pressure and a flow rate of 2000 ml_n/min ⁵. A 10% dilution by an Argon/Helium mixture as internal standard for the gas analysis was used, and the ceramic oven enclosing the reactor tube was set to 970 K. The residence time amounts to roughly 2 seconds.

The outcome of the numerical simulation is depicted in Figure 5.9, where contour plots of velocity, temperature as well as the investigated species are shown. The boundary conditions were defined such that the reactants, methane and oxygen, enter from the left at uniform temperature and flow velocity. In each plot, the thin solid and dashed white lines correspond to the 0.099 and 0.09 isolines of the O_2 mole fraction, respectively, i.e. 1 and 10% conversion; these lines help indicate qualitatively the reaction onset. The following qualitative observation can be made from the contour plots: First, it is seen that an annular velocity profile develops due to the dual no-slip boundary condition at the wall and the fused silica capillary at the center. Second, the wall exhibits an inhomogeneous temperature distribution – ranging from ~ 900 to 980 K – which underlines the importance of heat transport within the wall. Once the exothermic chemistry has begun, it dominates the heat release in the flow, and the reactor wall becomes a heat sink. Third, it is instructive to observe the onset of reaction indicated by the 0.099 and 0.09 O_2 mole fraction contour lines. Close to the wall, the temperature between the two contour lines is between 910 and 940 K, whereas at the center of the

⁵The entire set of results is going to be presented in a forthcoming report by the authors.

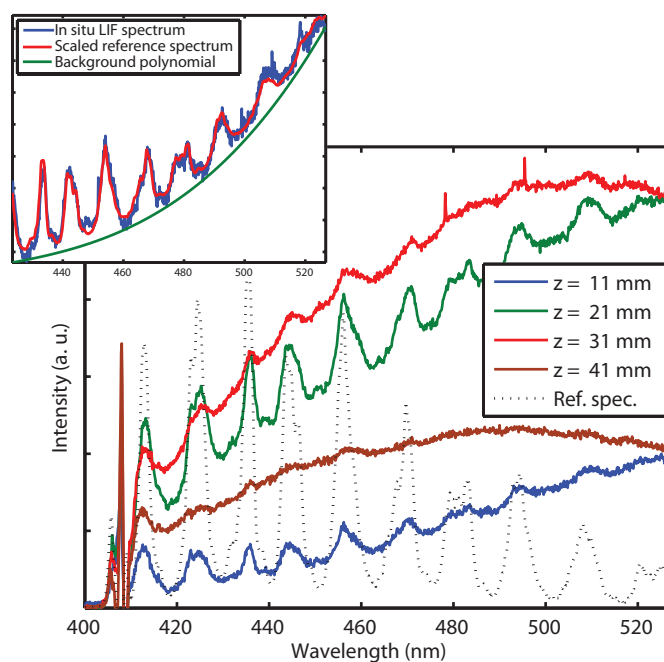


Figure 5.7: In situ CH_2O LIF spectra at different axial positions in the reactor. An ex situ CH_2O spectrum is also depicted as reference (dotted line), clearly showing the characteristic CH_2O vibrational features in the in situ spectra. The inset shows the polynomial fitting of the broadband background which allows isolation of the CH_2O signal.

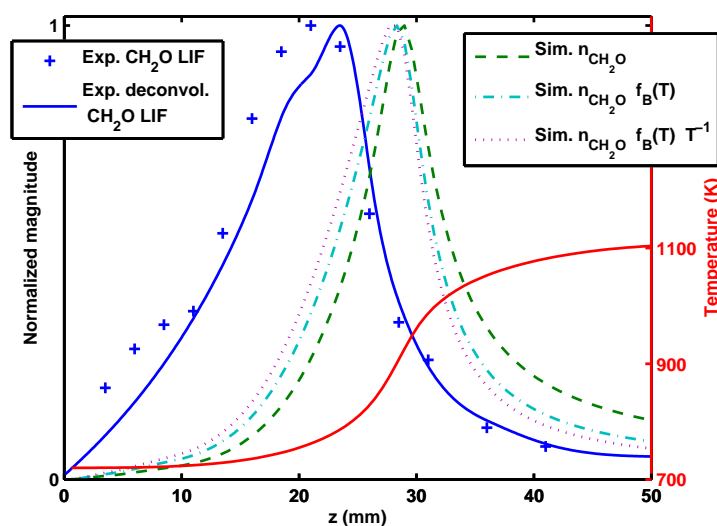
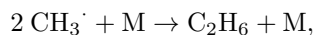


Figure 5.8: Deconvolution of LIF profile and impact of Boltzmann and quenching correction on CH_2O profile.

reactor oxygen consumption starts at a much lower temperature of 730 - 770 K. This suggests that the reaction first ignites thermally close to the wall due to external heating and only then the reaction diffuses radially into the reactor center. The centerline temperature profile is therefore not a good benchmark for the onset temperature of the reaction. Fourth, once the O₂ mole fraction drops below roughly 0.02, then the gradients for all other species become considerably less steep, and downstream of that point the overall composition changes only slightly. Lastly, the concentration profiles for H₂ and CH₂O stand out in particular. The H₂ gradients are less pronounced, presumably due to its high diffusivity. The CH₂O is unique in that it is clearly a reactive intermediate, with a concentration profile confined to a narrow region of peak oxidation.

The centerline profiles from the two-dimensional distributions are compared with the experimental data. The simulated profiles and experimental data are depicted in Figure 5.10. Globally, we observe the following trends in both experiment and simulation: Primary reaction products in order of abundance are H₂O, CO, H₂, and minor amounts of CO₂. Formaldehyde CH₂O is formed as one of the primary products in the pre-reaction zone; being a reaction intermediate it is almost completely consumed subsequently. While C₂H₆ is produced predominantly by the direct coupling of two methyl radicals via the trimolecular reaction



C₂H₄ is only a secondary product formed by dehydrogenation of C₂H₆. Further dehydrogenation is minor, and therefore acetylene is formed only in trace amounts on the order of $\sim 6 \cdot 10^{-5}$. Though the GC was not calibrated for C₃ species, we estimate that C₃H₆ and C₃H₈ were formed in amounts of approximately 0.001 and 0.0003, respectively. Consumption of oxygen leads to a slowdown and eventually to an almost halt of the reaction. It is interesting to note that the exit composition is far from the composition predicted by thermodynamic equilibrium. The kinetic control provided by the self-induced oxygen exhaustion and the short residence time yields a mixture composition in an off-equilibrium state (cf. Table 5.1).

While experiment and simulation are in good agreement, it is now of interest to focus on the discrepancies between the two. It should be mentioned that the temperature measurements were not corrected for radiation, so the thermocouple reading may be biased by radiation heat exchange with the oven coils. But this effect is presumably only important when the gas temperature is low, such as at the reactor entrance. As soon as exothermic chemistry starts and the temperature rises, it dominates the temperature reading of the thermocouple. Generally, the temperature profile is in fair agreement with the simulation indicating that the global heat balance is conserved by the simulation. In the following, we will successively discuss causes that may contribute to the quantitative disagreement between the experiments and modeling. The discussion is based on the following three observations, i. e. differences in

- reaction onset,
- reaction gradients, and
- absolute concentrations.

The difference in *reaction onset* is manifested in an axial shift of the profiles, which is most evident in the shift of the formaldehyde peak concentration position. It bears mentioning that this problem is routinely encountered in flow reactor measurements [112]. Although “time-shifting” is an accepted practice when modeling flow-reactors (cf. to Supplementary Material of [112]), we have chosen not to do so as to highlight

5.4. Results and Discussion

Molar fractions	Experiment	Simulation	Thermodynamic Equilibrium
CH ₄	0.67	0.67	0.46
O ₂	0.007	0.008	0
H ₂ O	0.122	0.103	0.001
H ₂	0.032	0.046	0.30
CO	0.049	0.055	0.15
CO ₂	0.005	0.007	0.0006
C ₂ H ₆	0.011	0.004	0.0003
C ₂ H ₄	0.011	0.007	0.0002
C ₂ H ₂	$\sim 6 \cdot 10^{-5}$	$5 \cdot 10^{-5}$	$2 \cdot 10^{-6}$
C ₃ H ₈	$\sim 3 \cdot 10^{-4}$	$8 \cdot 10^{-5}$	$5 \cdot 10^{-7}$
C ₃ H ₆	$\sim 1 \cdot 10^{-3}$	$5 \cdot 10^{-4}$	$4 \cdot 10^{-6}$

Table 5.1: Molar fractions at reactor outlet of experiment and simulation in comparison to the thermodynamic equilibrium composition at 1100 K. All species showing an equilibrium value above 10^{-6} as well as C₃H₈ are listed.

the strengths and limitations of the current approach. The shift in reaction onset could be attributed to a combination of two possible effects. (i) In the simulations, the outer wall temperature was set equal to the oven temperature which was measured in each experiment. Using the oven temperature as boundary condition on the reactor tube is naturally an overestimate because the oven coils and the outer tube wall are not in thermal equilibrium. The actual boundary condition for the outer wall may hence be lower than assumed. Also, the uniform temperature boundary conditions imposed at the inlet can only be an approximation to the real inlet distributions where one may still find radial gradients despite the efficient heat-transfer inside the foam. (ii) Radiative heat transfer was not included in the simulation, though methane features infra-red absorption bands. Since the inlet gas composition is 80 % methane, radiative heat transfer from the oven coils to methane could have a non-negligible heating effect. In the optically thin approximation, Bhattacharjee and Grosshandler [113] have introduced a dimensionless quantity (similar to the Reynolds and Péclet number) which compares radiative and convective heat transport,

$$\frac{\sigma a (T_{\text{wall}}^4 - T^4)}{\rho u c_p / L (T_{\text{out}} - T_{\text{in}})}. \quad (5.12)$$

Here, σ is the Stefan-Boltzmann constant, a is the absorption coefficient of the gas [114], T_{wall} and T are the wall and gas temperatures, respectively, ρ is the fluid density, u and L are the characteristic velocity and length scale, and $T_{\text{out}} - T_{\text{in}}$ is the characteristic fluid temperature gradient. If global characteristic scales are considered this value is of order 0.1, but again the dimensional analysis may not be valid locally so that radiative heat transport may still have an influence. However, the effect is pronounced only in regions where the fluid temperature T is much lower than the wall temperature T_{wall} such as at the reactor inlet and close to walls where the velocity is vanishing. Accordingly, it has been observed in accompanying experiments that the disagreement

of the reaction onset becomes more pronounced the longer the non-reacting thermal entrance region of the flow is. In these cases the heat balance error accumulates up to the point of reaction onset and leads to more pronounced relative shifts of experimental and simulated profiles. However, once the ignition temperature is reached the heat generation due to the reaction dominates the energy balance and the temperature difference between fluid and “radiating” wall is then relatively small, which justifies comparison of experiment and simulation despite this shortcoming of the model.

The simulated *reaction gradients* are steeper than those observed in the experiments. There are three possible explanations: (i) In the experiment, the gas mixture is sampled over a finite volume. But since the sampling volume is much smaller than the observed gradients, this effect can be excluded from causing the shallower gradients. (ii) A second consideration is the modeling of molecular transport within the gas phase. The present work uses the more computationally feasible mixture-average approach. Although a more rigorous multi-component model could change the gradients, it is unlikely that this effect would be major. (iii) The third explanation for the observed differences is attributed to the mechanism itself. Since the mechanism reduction did not show a significant difference in reaction gradients, the differences would imply generally overpredicted rates by the mechanism.

The *absolute concentrations* of the major species are in good agreement. H_2O is somewhat underpredicted and H_2 is slightly overestimated by the simulation, while both CO and CO_2 are slightly overpredicted. However, the discrepancy for the concentrations of the C_2 species is considerably more significant. The primary coupling product C_2H_6 is underestimated by a factor of three, while C_2H_4 is underpredicted by roughly one-third of the experimental value. As was shown in Section 5.3.1, the deviations resulting from the mechanism reduction were considerably smaller. Since ethylene is produced predominantly by the dehydrogenation of its (underpredicted) precursor C_2H_6 , it is probable that the smaller disagreement of C_2H_4 is rather a coincidence. It therefore appears that C_2H_6 formation might be underestimated, while at the same time the dehydrogenation channel of C_2H_6 to C_2H_4 is overestimated. The estimated mole fractions for C_2H_2 , C_3H_8 and C_3H_6 are in agreement the simulation trends. Since the LIF measurements are non-quantitative no judgment on the CH_2O concentrations can be made.

5.4.3 Kinetic Discussion

It is of interest to use the mechanism to reveal the underlying kinetic pathways of methane oxidation at the above conditions. The fundamental kinetics of methane oxidation are well understood, even if as seen above the rate coefficients are not always suitably accurate for all conditions. The mechanism by which methane is oxidized changes with temperature, and it is commonly divided into a low-temperature and a high-temperature pathway. OCM is unusual in that it is highly fuel rich and thus a combination of oxidation and pyrolysis. The current conditions correspond to the upper limit in temperature of the low-temperature oxidation regime.

To generate the flux diagram, a plug-flow reactor was performed in CHEMKIN-PRO, using the experiment’s temperature profile to fix the energy equation. A reaction path analysis was performed for three positions along the reactor, each position being representative for a certain temperature regime along the reaction coordinate, i.e. 700, 900 and 1100 K. In the following we provide a qualitative description for the three reaction domains; the respective flux diagrams are presented in Figure 5.11.

5.4. Results and Discussion

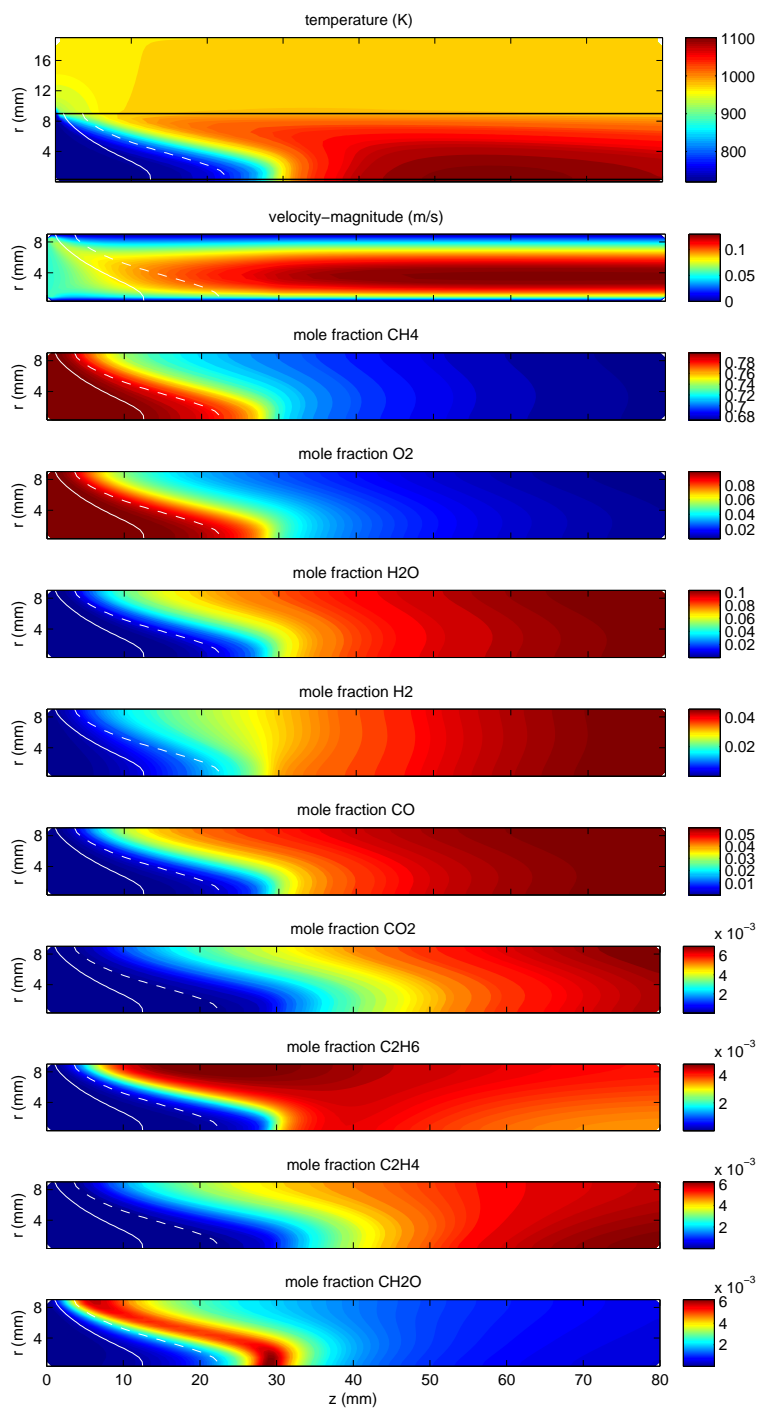


Figure 5.9: Numerical simulation contours of temperature, velocity and major species' mole fractions in cylindrical coordinates. The symmetry axis is at the bottom, the reactor entry is on the left and the flow direction is from left to right. As a guide for the eye the 0.099 and 0.09 isolines of the O_2 molar fraction (i.e. 1 and 10% conversion) is indicated as white lines.

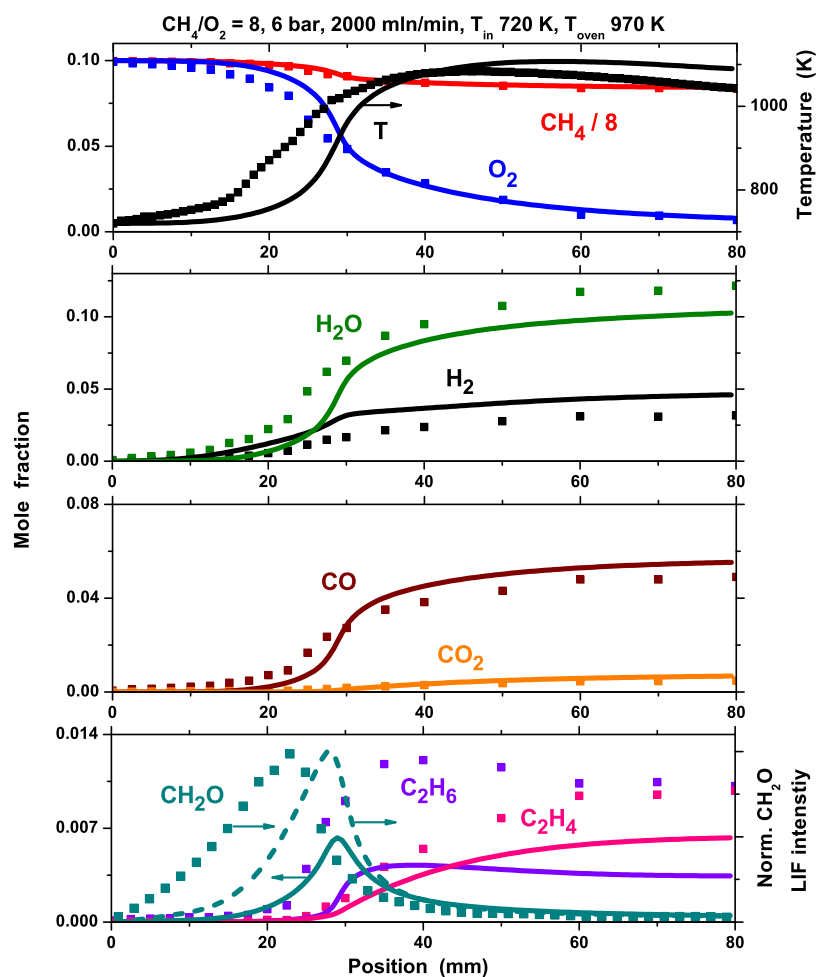
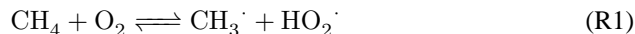


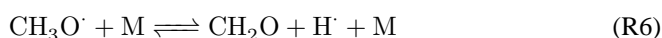
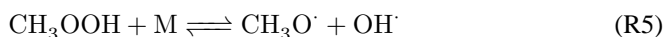
Figure 5.10: Experimental (marks) and simulated (lines) temperature and speciation profiles. Mole fractions for all species are depicted with respect to the left axis. In the top graph also the temperature is given with respect to the right axis, while the bottom plot includes the experimental (marks) and simulated (dashed line) normalized CH_2O LIF intensities on the right axis. Conditions correspond to a CH_4/O_2 feed ratio of 8, 6 bar pressure, and a total flow rate of 2000 ml_n/min. The simulation results are based on the reduced kinetic mechanism of Dooley [5].

5.4. Results and Discussion

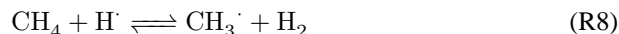
At the inlet, the temperature is low (700 K), which is solidly in the low-temperature kinetic regime. The initiation reaction is



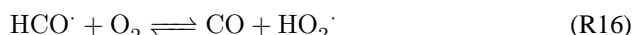
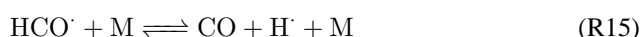
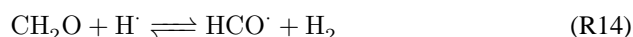
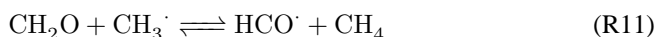
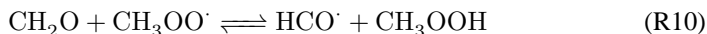
At this temperature, we have the following sequence of reactions:



With these six reactions, a radical pool is established consisting of $\text{H}\cdot$, $\text{OH}\cdot$, $\text{CH}_3\cdot$, $\text{CH}_3\text{O}\cdot$, $\text{HO}_2\cdot$, and $\text{CH}_3\text{OO}\cdot$. Once the radical pool is established, most methyl is generated not by R1 but through H-abstraction from methane via R3 and R7-R9:



The first six reactions convert CH_4 into CH_2O , which is converted to $\text{HCO}\cdot$, which in turn either decomposes or reacts with oxygen to yield CO :

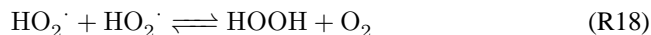


At this point the only stable carbon-containing products are CH_2O and CO . In Figure 5.11a, we see that most of the CH_4 is broken down by $\text{OH}\cdot$, followed by $\text{CH}_3\text{OO}\cdot$, $\text{H}\cdot$, and $\text{HO}_2\cdot$. Virtually all of the $\text{CH}_3\cdot$ reacts with oxygen to form $\text{CH}_3\text{OO}\cdot$. The $\text{CH}_3\text{OO}\cdot$ reacts with CH_4 and with $\text{HO}_2\cdot$. CH_3OOH decomposes via R5. Eventually CH_2O builds up, which reacts with $\text{CH}_3\text{OO}\cdot$ and $\text{HO}_2\cdot$ to form $\text{HCO}\cdot$. $\text{HCO}\cdot$ is mostly consumed by O_2 , yielding CO .

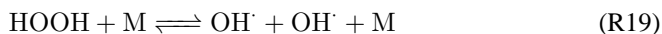
Another important reaction is:



Even though R16 and R17 are chain propagating, they convert a reactive radical ($\text{H}\cdot$ or $\text{HCO}\cdot$) into a more stable radical ($\text{HO}_2\cdot$), and thus temporarily slow down oxidation. Additionally, there is also the chain terminating reaction:



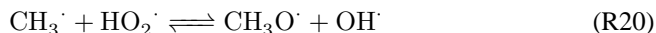
Reaction R9, R12, and R18 form hydrogen-peroxide, HOOH. Once there is sufficient HOOH, a new chain-branching reaction becomes competitive:



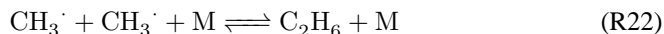
R19 is quite slow at these temperatures, so HO_2^\cdot formation generally acts like a radical sink. The decomposition of methyl-hydroperoxide R5 is the main chain branching reaction. At higher temperatures, however, R19 becomes much faster and ultimately becomes the main chain branching reaction in the reaction zone.

R1-R19 is an abbreviated description of the classical low-temperature mechanism for CH_4 oxidation. Numerous cross reactions have been omitted for clarity (for example: some $\text{CH}_3\text{O}^\cdot$ will abstract H-atoms to form methanol, which has its own submechanism, but it is irrelevant for the present conditions).

The reaction zone is characterized by rapid O_2 conversion, product build-up, and a sharp profile for the intermediate CH_2O at a temperature around 900 K. This temperature is close to the upper limit at which $\text{CH}_3\text{OO}^\cdot$ is stable, with the equilibrium constant beginning to shift back in favor of the bimolecular reactants (cf. reaction R2). Some of the CH_3^\cdot still reacts with O_2 to form $\text{CH}_3\text{OO}^\cdot$, but it is now a minor channel. The most important sink for CH_3^\cdot is the reaction with HO_2^\cdot and to a smaller extent with O_2 :



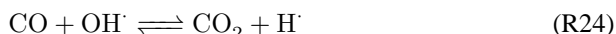
After R20, the next most important reaction is R22, the main coupling reaction:



Roughly 85% of the CH_3 goes through R20, and only $\sim 10\%$ through R22, thereby opening up the C_2 channel. The $\text{CH}_3\text{OO}^\cdot$ channel is minor at this point, and the main chain branching sequence at 700 K (R2-R5) becomes almost irrelevant at 900 K. Instead, the formation and decomposition of HOOH – reactions R9, R12, R18, and R19 – is now the main chain branching sequence. The slow build-up of HOOH reaches a tipping point at the start of the reaction front, which leads to spontaneous growth in OH^\cdot production, which accelerates both the formation and decomposition of CH_2O . The rapid increase in CH_2O decomposition leads to a spike in HCO^\cdot . Almost all of the HCO^\cdot reacts with O_2 , which is the main reaction for O_2 consumption.

As C_2H_6 builds up, it reacts with OH^\cdot , H^\cdot , CH_3^\cdot , and to a lesser extent HO_2^\cdot to form ethyl. Virtually all of the $\text{C}_2\text{H}_5^\cdot$ reacts with O_2 to form $\text{C}_2\text{H}_4 + \text{HO}_2^\cdot$.

Behind the reaction front the temperature has reached almost 1100 K. The coupling reaction R22 becomes the most important sink for CH_3^\cdot , followed by the reactions with HO_2^\cdot , and CH_2O . At this temperature $\text{CH}_3\text{OO}^\cdot$ is not stable; the equilibrium constant has shifted back to the bimolecular reactants, and the reaction sequence R2-R5 is inconsequential. Additionally, the increase in temperature now allows for the oxidation of CO. The reaction of CO with HO_2^\cdot and OH^\cdot releases considerably heat, creating a positive thermal feedback loop.



5.5. Conclusion

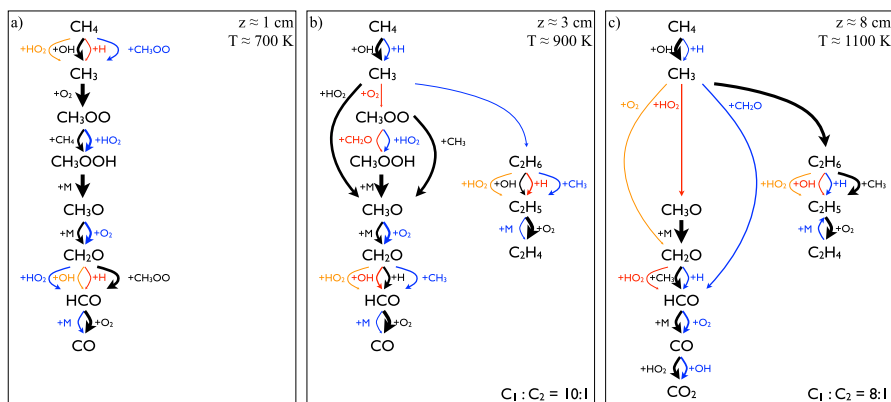


Figure 5.11: Flux diagrams for three different positions along the reaction coordinate, corresponding to temperatures 700, 900 and 1100 K. With respect to the experiment, the temperature regimes correspond to the reactor entry, the reaction zone (defined by the steepest O_2 gradient) and the exit of the reactor, respectively. The line color and thickness indicate the relative importance of each pathway, with the black lines being the most dominant, followed by blue, red, then orange.

In the C_2 pathway the only differences are: (i) the build-up of C_2H_4 causes the thermal decomposition of C_2H_5 to run in reverse (i.e. $H^\cdot + C_2H_4 \rightarrow C_2H_5^\cdot$), (ii) the onset of high-molecular weight growth (not shown).

The formation and decomposition of HO_2 is still the main chain branching sequence. Even at 1100 K, the temperature is still too low for



The temperature is high enough that CH_3OO^\cdot is minor, but it is low enough that R17 dominates R25 (i.e. $H^\cdot + O_2$ gives HO_2 instead of $OH^\cdot + O$), so oxidation is still slow and incomplete.

5.5 Conclusion

We presented kinetic profile measurements and numerical simulations for fuel-rich methane partial oxidation stoichiometries encountered in methane oxidative coupling, the results of which are representative of a set of experiments performed under different conditions (by varying composition CH_4/O_2 4 - 16 and pressure 1 - 8 bar). The experiment was conducted at a pressure of 6 bar with a CH_4/O_2 ratio of 8 and temperatures around 900 K in a versatile flow reactor with spatial sampling capabilities. Use of a novel technique for laser-induced fluorescence (LIF) detection of CH_2O using an optical fiber probe was demonstrated. Full Navier-Stokes kinetic numerical simulation were performed using a reduced version of the mechanism by Dooley et al. [5], and the results were compared to the experimental data.

The results show that predictive kinetic modeling of industrial processes is still challenging. Comprehensive and numerically expensive simulations have to assure the accurate description of both physical and chemical processes in the reactor. Not only accurate kinetic mechanisms but also heat and mass transport properties play an

important role in the evaluation of the profiles. The results suggest that the mechanism gives qualitatively and quantitatively correct predictions for the main species. However, in particular the evolution of the C_2 species appears to be captured less accurately. As a systematic difference between experiment and simulation it was observed that the mole fraction profiles of C_2H_6 and C_2H_4 are predicted too low.

The findings give interesting insight into the kinetics of fuel-rich methane oxidation at the upper limit of the low-temperature kinetic regime in particular with respect to C_2 formation. It is noteworthy that formation of C_2 species through coupling of methyl radicals is possible in the pure gas-phase. However, the selectivity observed in the gas-phase is poor. Under industrial catalytic high-pressure conditions gas-phase reactions are likely to occur in parallel to heterogeneous reactions which may lead to homogeneous-heterogeneous coupling. The inclusion of gas-phase chemistry in modeling is thus a prerequisite for design of an efficient process.

Chapter 6

Methane Oxidation over a Platinum Gauze at $\phi = 0.5$ and 2.0

This Chapter presents the last set of methane oxidation experiments that were performed in the profile reactor. The aim is to prove the feasibility of OH radical detection under over-stoichiometric (excess methane) conditions using the optical-fiber LIF method. With this intention the reaction was anchored on a platinum gauze. Despite this objective I will give a more general introduction.

6.1 Introduction

Literature contains a large body of works on methane oxidation on platinum catalysts, ranging from lean combustion with equivalence ratios $\phi < 1$ to partial oxidation at equivalence ratios ϕ up to 10*. Different catalyst morphologies and reactor geometries have been studied, such as stagnation flows [115, 116], gauzes [117, 16, 118, 119, 120, 13, 121, 122], coated foam and channel monoliths [123, 115, 16, 124, 125] and channel-flow reactors [126]. This report summarizes experiments which are closely related to the works of Davis et al. [119], Heitnes Hofstad et al. [117] and de Smet et al. [118, 120], which have all studied methane oxidation over platinum gauzes. Reactions over gauzes are characterized by the intrinsic short contact times and oxidation over gauzes is also an industrially relevant process, e.g. in selective ammonia oxidation [127].

Davis et al. have studied lean methane/air combustion (equivalence ratio $\phi = 0.32$ – 0.52) over a resistively heated platinum gauze at ambient pressure. In the wake of the Pt gauze OH radical concentration profiles were measured using laser-induced fluorescence (LIF) spectroscopy, however no other product species were analyzed. Both, Heitnes Hofstad et al. and de Smet et al., performed their experiments in the partial oxidation regime ($\phi = 4$ and 3.6 – 10 , respectively). Their reactors were externally heated and the product species composition was analyzed at the reactor outlet. While

*In particular in the combustion community it is common to use the equivalence ratio ϕ as a measure for the feed stoichiometry. It is defined as the CH_4/O_2 feed ratio divided by the stoichiometric CH_4/O_2 ratio, so that $\phi = 1$ represents a stoichiometric mixture.

the former group operated their reactor at ambient pressure and diluted the feed gas with 77% argon, the latter experiments were conducted at elevated pressures (1.3–2.4 bar) and varying dilution of 40–80% helium. In Heitnes Hofstad’s experiments the platinum gauze was sandwiched between two ceramic monoliths, whereas in the other setups the gauze was positioned in the free gas-phase.

In all reports the question was addressed whether homogeneous and heterogeneous reactions compete and transport-limitation occur. It is known that there are different regimes for homogeneous-heterogeneous dynamics [41, 43, 44]. Apart from cases in which either surface or gas-phase reactions dominate, there can be cases in which gas-phase chemistry is sustained by heterogeneous processes or conversely, the surface represents a sink for radical species thus terminating the homogeneous reaction channel. Davis et al. note that the homogeneous and heterogeneous reactions appeared to be spatially decoupled in their lean combustion experiments. Apart from using high inert gas dilution, in the reactor from Heitnes Hofstad gas-phase reactions before and after the gauze are presumably suppressed by radical quenching in the monolith. De Smet et al. state that they used low reactant partial pressures to suppress homogeneous chemistry and argued that gas-phase reactions can be neglected because homogeneous plug-flow reactor simulations showed very low conversion.

One of the main hindrance in answering the question of homogeneous-heterogeneous dynamics is the lack of experimental techniques to recover the intrinsic kinetics of the process. This report presents an approach to attain the kinetic information by measuring species profiles over a platinum gauze. The experiments were conducted at two stoichiometries, namely $\phi = 0.5$ and 2.0, in a dedicated flow reactor [92]. In this reactor, stable product species as well as gas-phase radicals can be measured along the reactor centerline using a sampling technique in combination with a novel fiber-optic laser-induced fluorescence method allowing detection of OH radicals [93].

6.2 Experimental

6.2.1 Sampling Reactor

A sketch of the reactor assembly is depicted in Figure 6.1. The platinum gauze consists of 3600 meshes/cm² with a wire diameter of 40 μm and is clamped inside the reactor as shown. The fused silica flow reactor is heated by an electrical furnace and operated at a slightly elevated pressure of 1.5 bar. As indicated, the sampling capillary can be traversed along the center of the reactor allowing reactant mixture samples to be extracted continuously. Positioning of the capillary using a stepper motor permits high spatial resolution. The magnification in Figure 6.1 illustrates the sampling process and reveals the fiber-optic probe for OH detection accommodated inside the sampling capillary. A top-view microscope image of the assembly is shown in Figure 6.2. The sampling rates are adjusted such that they are considerably smaller than the total flow rate ($\dot{V}_{\text{sampl}}/\dot{V}_{\text{tot}} \sim 10^{-4}$), so that the main flow remains unaffected from the sampling. Rapid sample extraction and radical removal by collisional wall-quenching [68] inhibit reaction progress inside the sampling capillary and hence ensure unbiased ex situ sample analysis. The gas composition is analyzed in a mass spectrometer. It is clear that the gas mixture is sampled over a finite volume which may deteriorate the spatial resolution of the measured profiles. In accompanying experiments another sampling capillary was used which possesses a small side sampling orifice with a diameter of 100 μm (this capillary was also described in the original report on the reactor [92]).

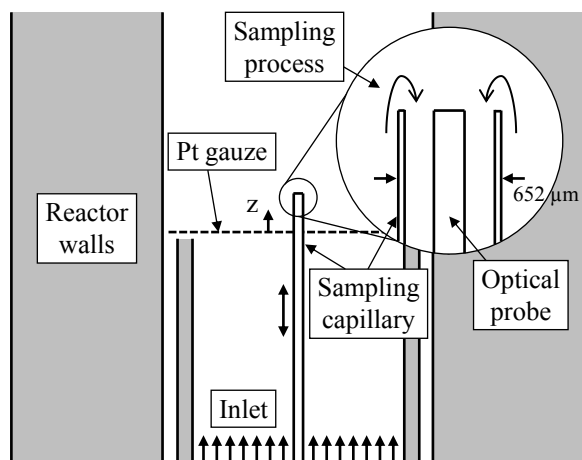


Figure 6.1: Experimental setup. The magnification shows the sampling capillary as well as the optical-fiber probe.

The sampling volume of that probe is of the size of the orifice which was ascertained by CFD simulations of the sampling process. Since, species profiles taken with either sampling capillary showed congruent results a spatial resolution on the order of $100\ \mu\text{m}$ is generally assumed for the presented data.

The Pt gauze was prepared and activated in a similar manner as described by de Smet et al. [118]. It was first reduced in a flow of 10 % H_2 in Ar while heating the reactor up to $700\ ^\circ\text{C}$. Then, the catalyst was activated using a $\text{C}_2\text{H}_6/\text{O}_2/\text{Ar} = 3/2/5$ mixture. The actual experiments were conducted with a CH_4/O_2 mixture diluted in 80 % Argon. The flow rates for the lean (oxygen-rich) conditions, i.e. $\phi=0.5$, were 120 mln/min CH_4 , 480 mln/min O_2 , and 2400 mln/min Ar, while in the fuel-rich case, i.e. $\phi = 2.0$, flow rates were 150 mln/min CH_4 , 150 mln/min O_2 , and 1200 mln/min Ar. The furnace temperature was controlled at $700\ ^\circ\text{C}$ in both experiments.

6.2.2 Fiber-optic LIF

Gas-phase methane oxidation involves radical chain reactions. Unlike stable reaction species, radicals are quenched throughout the sampling process and can therefore not be detected in that way. This common problem can be overcome by introducing laser-spectroscopic methods such as laser-induced fluorescence (LIF) spectroscopy, at the expense of providing optical access to the system. However, this is not always possible in practical systems. On this account a fiber-optic probe has been developed which is conveniently accommodated inside the sampling capillary. The presented fiber assembly is an advancement of the optical probe reported previously (cf. [93] or Chapter 4). It consists of a multi-mode fiber (core-diameter $100\ \mu\text{m}$) for delivering the excitation laser-pulse, while the surrounding light guiding capillary collects the fluorescence signal (Figure 6.2). In the former experiments, a single fiber was used for both, laser delivery and fluorescence collection. The disadvantage of the latter excitation-detection geometry is that the transmission of the laser pulse leads to detrimental scattering interferences and hence low signal-to-background ratios for the desired OH fluorescence. Even though the overall collection efficiency is smaller for the new fiber-capillary as-

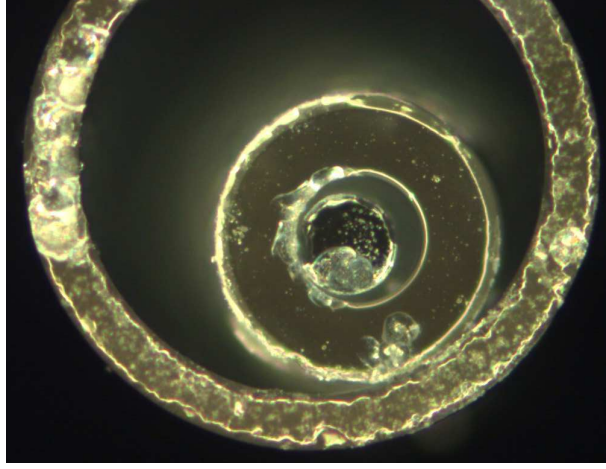


Figure 6.2: Microscope top-view image of the sampling capillary and the polished optical-fiber probe. The image was taken after use. The outer diameters for the capillary and the optical-fiber probe are $652\ \mu\text{m}$ and $323\ \mu\text{m}$, respectively. The optical-fiber probe consists of the excitation fiber in the center (core diameter $100\ \mu\text{m}$) surrounded by the collection light-guiding capillary.

sembly, it achieves significantly better signal-to-background ratios compared to the single fiber probe.

It is evident that the LIF signal is collected over a finite volume. Based on geometrical considerations an instrumental function $\gamma(z)$ can be derived. Generally, the LIF signal originating from a certain point in space \mathbf{x} is proportional to the excitation intensity $I(\mathbf{x})$ and the collection solid angle $\Omega(\mathbf{x})$. Following the same considerations as outlined in [93], the instrumental function $\gamma(z)$, as a function of the distance from the probe tip z , may be found:

$$\gamma(z) = \int_0^{2\pi} d\varphi \int_0^\infty r dr I(\mathbf{x}) \frac{\Omega(\mathbf{x})}{4\pi} \quad (6.1)$$

Figure 6.3 shows $\Omega(\mathbf{x})$ (top) and $I(\mathbf{x})$ (middle), and the resulting instrumental function $\gamma(z)$ (bottom). Also shown in the plot is experimental data, showing good agreement with the analytically determined instrumental function. This experimental data corresponds to the scattering signal originating from the platinum gauze when the fiber probe approaches the gauze from the bottom and was acquired in the same experiment as described hereafter. The analytical instrumental function will be applied in what follows.

A frequency-doubled dye laser (Sirah, Cobra-Strech), which is pumped by the second harmonic of a Q-switched Nd:YAG laser (Spectra-Physics, Quanta-Ray) was used for excitation. Dye-laser pulses are characterized by a pulse length of $\sim 8\ \text{ns}$ and a nominal fundamental linewidth of $0.06\ \text{cm}^{-1}$. Pulses of around $0.1\ \text{mJ}$ were coupled into the excitation fiber, the LIF signal was guide on a metal-package photomultiplier (Hamamatsu, R9980U) and the voltage was acquired with a high-bandwidth digitizer. Every acquisition constitutes an excitation scan of the OH $A^2\Sigma - X^2\Pi$ ($0 \rightarrow 1$) band head at $\sim 281\ \text{nm}$, while detecting the $1 \rightarrow 0$ and $1 \rightarrow 1$ bands ($306 - 330\ \text{nm}$). The LIF signal depends on temperature through the Boltzmann population distribution of the

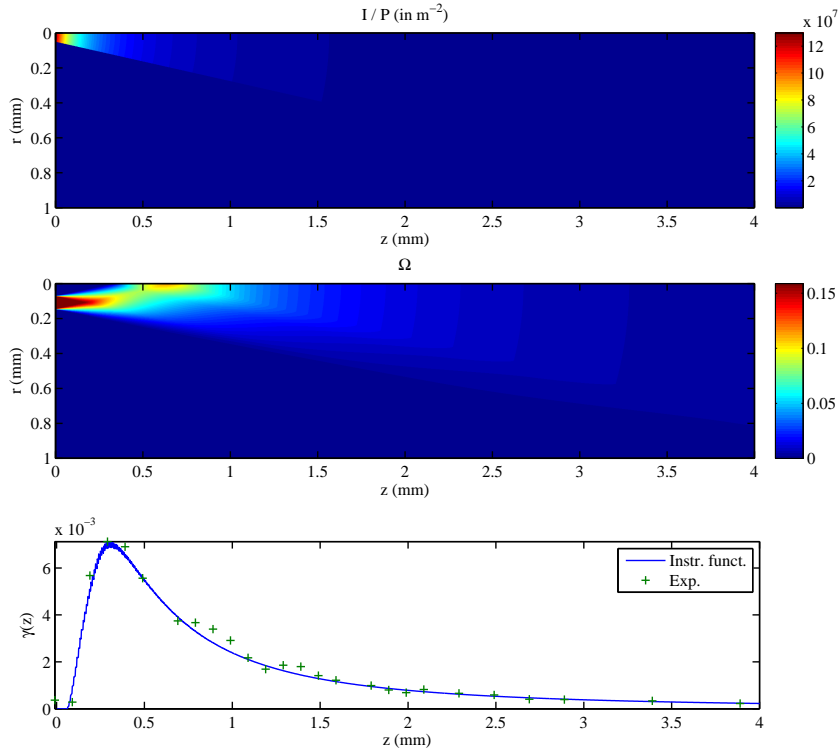


Figure 6.3: Irradiance field $I(\mathbf{x})$ normalized by the laser power P (top), and effective collection solid angle distribution $\Omega(\mathbf{x})$ (middle) in cylindrical coordinates (radial coordinated r and axial coordinated z). The excitation fiber has a core diameter of $100 \mu\text{m}$, while the collection light-guiding capillary has an outer diameter of $300 \mu\text{m}$. Both have a numerical aperture $\text{NA} = 0.22$. The bottom graph shows the instrumental function $\gamma(z)$ of the fiber probe, according to Equation (6.1). Also shown is experimental data which shows good agreement to the analytically determined function $\gamma(z)$

rotational states. In order to alleviate the temperature-dependence, the integral area under each spectrum was defined as the LIF signal. A one-point calibration with respect to the LIF signal was used to assign a OH number density to the signal. For the calibration a stoichiometric Bunsen-type flame as described in reference [93] was used.

6.3 Results and Discussion

6.3.1 Lean Combustion Regime ($\phi = 0.5$)

Hydroxyl-Radical LIF

Figure 6.4 shows OH excitation scans acquired at different positions inside the reactor, more precisely just before and after the Pt gauze as well as at greater distances from the gauze. It may be anticipated that the linewidth increases before and after the gauze due to thermal Doppler broadening. Likewise, it is expected that the rotational population distribution and thus the line intensities change. Both features are seen in the spectra. At this pressure, due to collisional quenching, the effective fluorescence lifetime is on the order of the excitation pulse length. Therefore it was not possible to extract a clear trend of the fluorescence lifetime from the oscilloscope traces.

A broad wavelength scan was performed 4 mm above the gauze in order to determine the rotational temperature; the corresponding Boltzmann plot of the rotational population distribution is shown in Figure 6.5. Despite the data scattering, the fitted temperature of 1650 K agrees with the expected equilibrium temperature of ~ 1600 K under the assumption that the fluid at the centerline of the reactor does not heat up considerably before reaching the catalyst gauze.

The one-point calibration yields OH number densities which are comparable (by a factor of 2) to those reported by Davis et al. and are in good agreement with the simulation presented below.

Species Profiles

The species profiles for the experiment performed with an equivalence ratio $\phi = 0.5$ are shown in Figure 6.6. The molar fractions are shown for the detected stable species, while the + symbols represent the OH signal measured by LIF. The instrumental function $\gamma(z)$ (cf. Equation 6.1) has been used to deconvolve the OH signal and the resulting OH number density profile is plotted as solid line. The deconvolution effectively leads to a downstream shift of the OH profile.

It is evident that the reaction is anchored at the gauze ($z = 0$). Methane is totally consumed and the major stable products are CO_2 and water. In proximity to the gauze $\sim 1\%$ of CO and small amounts of H_2 are detected. The OH number density peaks just above the gauze and subsequently decreases only slowly albeit the major reaction is over. It has to be pointed out that OH is an equilibrium product of considerable amount under these conditions which is one of the reasons why it is readily detected in combustion environments (cf. Figure 3.4). In fact, the OH equilibrium number density corresponds to $1 \cdot 10^{15} \text{ cm}^{-3}$ for the present conditions, which is in good agreement with the limit concentration reached at the reactor exit.

The fact that OH seems to be produced upstream of the catalyst gauze may be an artifact of the LIF method. As described above, the LIF signal is collected from a finite volume above the optical fiber tip described by the instrumental function. When the fiber approaches the gauze from the bottom, the signal collection is obscured by

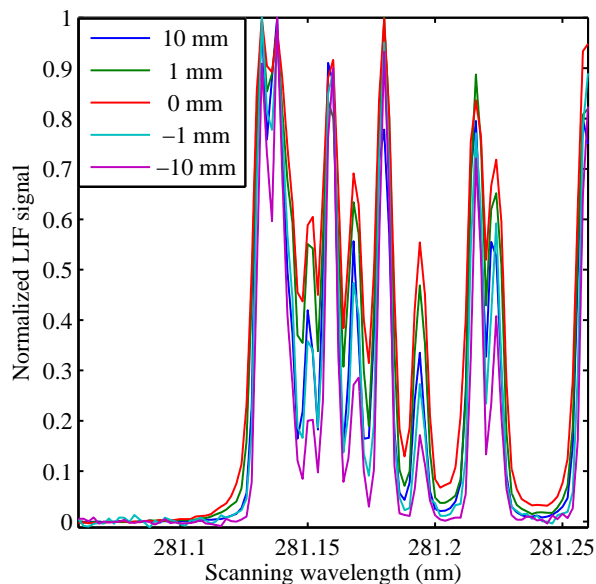


Figure 6.4: OH LIF excitation spectra of the 0→1 band-head under lean oxidation conditions. The individual spectra correspond to different positions in the reactor, namely before and after the gauze.

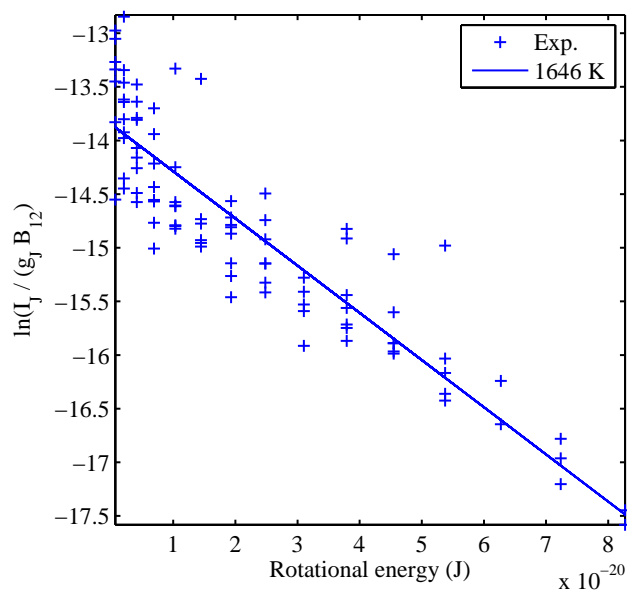


Figure 6.5: Boltzmann plot of rotational line intensity I_J corrected for degeneracy g_J and absorption coefficient B_{12} vs. rotational energy $hcBJ(J+1)$. J is the rotational quantum number. The rotational temperature of the Boltzmann fit corresponds to a temperature of 1650 K.

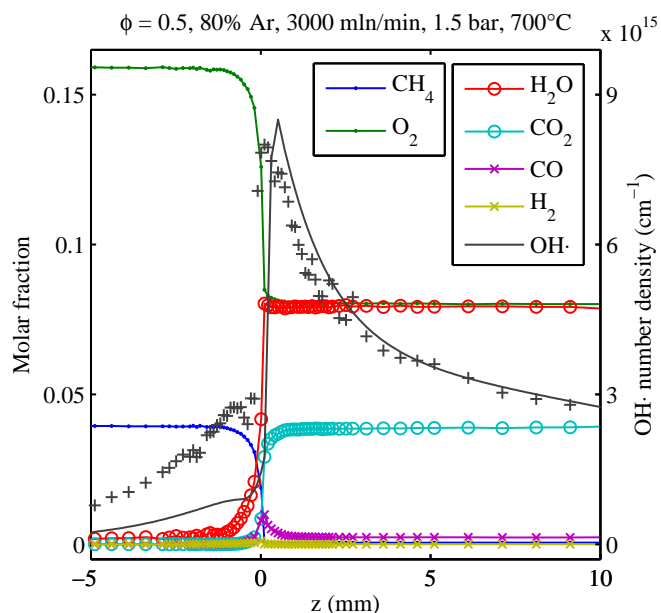


Figure 6.6: Experimental species profiles for $\phi = 0.5$, diluted in 80 % Ar, at 1.5 bar and a total flow rate of 3000 ml/min. The furnace temperature is 700 °C. The black solid line represents the OH number density profile obtained from deconvolution of the LIF signal (+ symbols).

the Pt gauze. This effect is obviously not included in the instrumental function and therefore the deconvolution is strictly valid only above the gauze ($z \geq 0$). The non-zero OH concentrations upstream the gauze may indicate the presence of a radical cloud surrounding the gauze.

Comparison to Simulation

Figure 6.7 shows a comparison of the experimental data to a CHEMKIN simulation. The freely propagating flame model was used together with the GRI reaction mechanism [128] optimized for combustion and ignition of methane[†]. The model also solves the energy equations so that no temperature profile has to be provided by the user. The inlet temperature ($T_{\text{in}} = 393$ K) for the simulation was chosen such that the temperature above the gauze matches the temperature acquired with LIF. In the plot the simulation results have been axially shifted to provide overlap of methane at 50% conversion. At the gauze ($z=0$) steeper, step-like gradients are observed in the experiment, indicating the catalytically assisted conversion at the gauze.

[†]It bears mentioning that the mechanism by Dooley et al. [5], which has been applied in the simulations for gas-phase OCM (Chapter 5), does not provide a converged solution using the same boundary conditions.

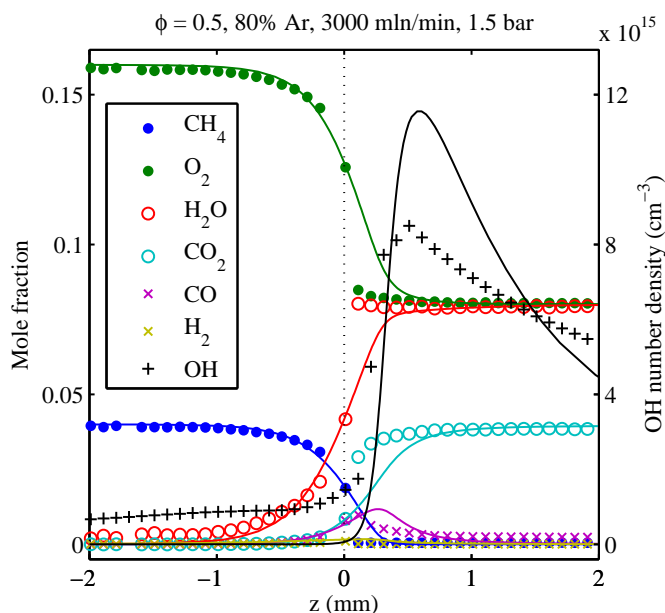


Figure 6.7: Species profiles of experiment (marks) and simulation (lines). For the simulation a freely propagating flame model was used.

6.3.2 Fuel-Rich Regime ($\phi = 2.0$)

Hydroxyl-Radical LIF

Under these conditions hardly any spectral features of OH could be identified in the LIF spectra. It appears that OH concentrations are just below the detection limit (~ 1 ppm) and therefore, no OH profiles could be recorded. Similarly, Davis et al. stated that they were not able to detect OH radicals while maintaining their experiments at equivalence ratios > 3.4 .

Species Profiles

Figure 6.8 shows the species profiles for the experiment performed in the fuel-rich regime, i.e. an equivalence ratio $\phi = 2.0$. Unfortunately, the data quality is not as good as in the previous results, but the important aspects still become clear. Again the molar fraction for the detected stable species are shown. Total conversion is achieved and H_2O , CO , H_2 and CO_2 are the major products in this order. Acetylene is the primary C_2 product on the order of 1 %. The reason for the obscure gradients remains unclear. Presumably, the reaction is instable or the Pt gauze may have been accidentally displaced while traversing the sampling capillary.

Comparison to Simulation

Using the same numerical model as applied for the lean conditions, the simulation did not yield a converged solution. When a reasonable temperature profile is provided, the simulation predicts merely minor conversion due to pure gas-phase chemistry. Hetero-

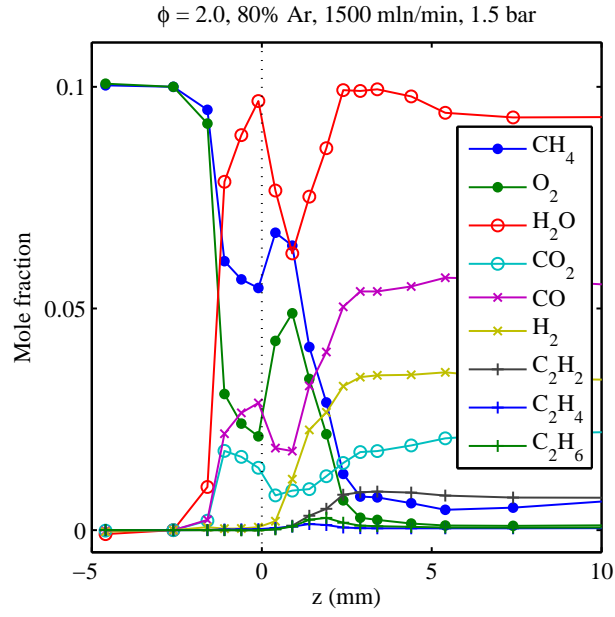


Figure 6.8: Experimental species profiles for $\phi = 2.0$, diluted in 80 % Ar, at 1.5 bar and a total flow rate of 1500 mln/min. The furnace temperature is 700 °C.

geneous kinetics would need to be included in the model to capture the experimental observations.

Chapter 7

Summary and Conclusions

In this thesis gas-phase kinetics of methane-oxidation was investigated under different stoichiometric regimes, namely stoichiometric combustion in an open, atmospheric Bunsen-type flame, fuel-rich methane oxidation in a high-pressure flow reactor with intent to study gas-phase oxidative coupling kinetics, and catalytically assisted methane-oxidation over a platinum gauze.

The key-approach is based on species profile measurements in conjunction with kinetic numerical simulations. The kinetic profile reactor, which had been developed by the group [92], is used for this purpose. Two methodological aspects are emphasized: (i) The development of a fiber-optic probe to measure transient species, such as OH radicals and CH_2O , using laser-induced fluorescence (LIF) spectroscopy. (ii) Based on state-of-the-art kinetic mechanisms taken from literature, appropriate reactor models and kinetic numerical simulations are employed to interpret the experimental results and unravel the underlying chemistry.

Up to now the profile reactor only allowed detection of stable species. In order to measure transient species a novel technique was developed which permits LIF measurements through an optical-fiber probe in otherwise optically inaccessible systems. Different fiber-optic probe geometries were developed and tested. A single fiber for excitation as well as collection of the LIF signal was employed in the experiments presented in Chapters 4 and 5 for detection of OH and CH_2O , respectively. An advanced fiber probe, consisting of individual excitation and collection channels, was employed in Chapter 6 for measuring OH radicals. Though the collection efficiency of the advanced probe is smaller it features a higher signal-to-background ratio compared to the single fiber.

In Chapter 4 vibrational Raman thermometry was applied in an air-fed flame using N_2 as probe molecule. Raman thermometry through an optical fiber was attempted but discarded due to the lack of an appropriate marker molecule under the investigated conditions.

Oxidative coupling of methane in the gas-phase was investigated in a high-pressure flow reactor at a CH_4/O_2 feed ratio of 8 (Chapter 5). Species profiles were measured and LIF detection of CH_2O through an optical fiber was demonstrated. Based on the full set of Navier-Stokes equations CFD simulations in conjunction with a detailed kinetic mechanism were performed. The agreement of experiment and simulation for the primary species was good. However, in particular the evolution of the C_2 species appears to be captured less accurately by the best state-of-the-art mechanism. A pathway

analysis gives interesting insight into the kinetics of fuel-rich methane oxidation, in particular with respect to C_2 formation. The information may be helpful in the design of efficient coupling processes.

In Chapter 6 methane oxidation over a platinum gauze was studied. The gauze serves to anchor the reaction and the intention was to verify the feasibility of detecting OH radicals under over-stoichiometric (excess methane) conditions. OH radicals were readily detected under lean (excess oxygen) conditions ($\phi = 0.5$). Under this conditions the temperature is high ($T_{\text{equ}} \sim 1600$ K) and OH is a quasi-equilibrium product appearing mainly in the post-reaction zone. Upstream the gauze the experimental profiles are reproduced by pure gas-phase simulation, while at the gauze a step-like conversion occurs due to catalytically assisted chemistry. Under methane-rich conditions with an equivalence ratio of $\phi = 2.0$ the temperature is still relatively high ($T_{\text{equ}} \sim 1400$ K) which favors higher OH concentrations. However, the concentrations appeared to be just below the detection limit of the technique (~ 1 ppm) and therefore detection at higher methane partial pressures, where OH concentrations are expected to be even lower, is unlikely. Simulations showed merely minor conversion, indicating that gas-phase chemistry is very slow under this condition and the impact of heterogeneous chemistry is more pronounced than for the previous case.

As respects the detection of OH radicals, the sensitivity of (optical-fiber) LIF has been proved to be insufficient to measure species profiles under conditions common to chemical synthesis. OH profiles could be recorded only under conditions in which the radical is a quasi-equilibrium product. One reason why OH detection using LIF could not be achieved is the fact that at atmospheric and above pressures a large portion of fluorescence is lost due to collisional deactivation (approximately one in a thousand at atmospheric pressure) which significantly lowers the detection limit of LIF. Other (spectroscopic) methods which provide higher sensitivities may have to be employed to detect OH and other radical species under methane-rich conditions.

Kinetic simulations are an invaluable tool in interpreting the experimental data. However, reactor modeling with respect to accurate description of both physical and chemical processes is challenging, and computational time constraints require a trade-off between the level of detail of the reactor model and the complexity of the chemical mechanism. Depending on the conditions a suitable mechanism has to be chosen and it may become necessary to reduce the mechanism to an appropriate subset of species. In spite of decades of research a universal kinetic mechanism accurately describing gas-phase methane oxidation in all stoichiometric regimes is not yet available. This fact has to be taken into consideration when coupling the gas-phase chemistry to a catalytic mechanism in a homogeneous-heterogeneous model. In proximity to the catalyst, i.e. within the catalytic boundary-layer, the partial pressures may be substantially different from the bulk gas-phase and hence, the accuracy of the mechanism may become questionable.

Bibliography

- [1] Richard A. Kerr. Peak oil production may already be here. *Science*, 331(6024):1510–1511, 2011.
- [2] Jack H. Lunsford. Catalytic conversion of methane to more useful chemicals and fuels: a challenge for the 21st century. *Catalysis Today*, 63(2-4):165–174, 2000.
- [3] Tao Ren, Martin Patel, and Kornelis Blok. Olefins from conventional and heavy feedstocks: Energy use in steam cracking and alternative processes. *Energy*, 31(4):425 – 451, 2006.
- [4] Eric McFarland. Unconventional chemistry for unconventional natural gas. *Science*, 338(6105):340–342, 2012.
- [5] S. Dooley, M. P. Burke, M. Chaos, Y. Stein, F. L. Dryer, V. P. Zhukov, O. Finch, J. M. Simmie, and H. J. Curran. Methyl formate oxidation: Speciation data, laminar burning velocities, ignition delay times, and a validated chemical kinetic model. *International Journal of Chemical Kinetics*, 42(9):527–549, 2010.
- [6] Hans Dieter Baehr and Stephan Kabelac. *Thermodynamik*. Springer, 15 edition, 2012.
- [7] Z. R. Ismagilov and M. A. Kerzhentsev. Catalytic fuel combustion—a way of reducing emission of nitrogen oxides. *Catalysis Reviews*, 32(1-2):51–103, 1990.
- [8] K. Aasberg-Petersen, J.-H. Bak Hansen, T.S. Christensen, I. Dybkjaer, P. Seier Christensen, C. Stub Nielsen, S.E.L. Winter Madsen, and J.R. Rostrup-Nielsen. Technologies for large-scale gas conversion. *Applied Catalysis A: General*, 221(1-2):379 – 387, 2001. Hoelderich Special Issue.
- [9] Ceri Hammond, Sabrina Conrad, and Ive Hermans. Oxidative methane upgrading. *ChemSusChem*, 5(9):1668–1686, 2012.
- [10] J. Eilers, S.A. Posthuma, and S.T. Sie. The shell middle distillate synthesis process (SMDS). *Catalysis Letters*, 7(1-4):253–269, 1990.
- [11] Francis G. Billaud, Christophe P. Gueret, and Francois Baronnet. Thermal coupling of methane in a tubular flow reactor: experimental setup and influence of temperature. *Industrial & Engineering Chemistry Research*, 31(12):2748–2753, 1992.
- [12] S.S. Bharadwaj and L.D. Schmidt. Catalytic partial oxidation of natural gas to syngas. *Fuel Processing Technology*, 42(2–3):109–127, 1995.

-
- [13] Marie-Francoise Reyniers, Carlo R.H. de Smet, P.Govind Menon, and Guy B. Marin. Catalytic partial oxidation. part i. catalytic processes to convert methane: Partial or total oxidation. *CATTECH*, 6(4):140–149, 2002.
- [14] Y.R. Luo. *Comprehensive Handbook of Chemical Bond Energies*. Taylor & Francis, 2010.
- [15] Peter Pässler, Werner Hefner, Klaus Buckl, Helmut Meinass, Andreas Meiswinkel, Hans-Jürgen Wernicke, Günter Ebersberg, Richard Müller, Jürgen Bässler, Hartmut Behringer, and Dieter Mayer. *Ullmann's Encyclopedia of Industrial Chemistry*, chapter Acetylene, pages 277–326. Wiley-VCH Verlag GmbH & Co. KGaA, 2000.
- [16] K.L. Hohn, P.M. Witt, M.B. Davis, and L.D. Schmidt. Methane coupling to acetylene over pt-coated monoliths at millisecond contact times. *Catalysis Letters*, 54(3):113–118, 1998.
- [17] Gerhard Ertl. *Handbook of heterogeneous catalysis*. Wiley-VCH, Weinheim, 2 edition, 2008.
- [18] Ulyana Zavyalova, Martin Holena, Robert Schlögl, and Manfred Baerns. Statistical analysis of past catalytic data on oxidative methane coupling for new insights into the composition of high-performance catalysts. *ChemCatChem*, 3(12):1935–1947, 2011.
- [19] Yee San Su, Jackie Y. Ying, and William H. Green. Upper bound on the yield for oxidative coupling of methane. *Journal of Catalysis*, 218(2):321–333, 2003.
- [20] Jay A. Labinger. Oxidative coupling of methane: An inherent limit to selectivity? *Catalysis Letters*, 1(11):371–375, 1988.
- [21] Q. Chen, P. M. Couwenberg, and G. B. Marin. Effect of pressure on the oxidative coupling of methane in the absence of catalyst. *AIChE J*, 40(3):521–535, 1994.
- [22] Jack H. Lunsford. The Catalytic Oxidative Coupling of Methane. *Angewandte Chemie International Edition in English*, 34(9):970–980, 1995.
- [23] Kenji Asami, Kohji Omata, Kaoru Fujimoto, and Hiro-o Tominaga. Oxidative coupling of methane in the homogeneous gas phase under pressure. *Journal of the Chemical Society, Chemical Communications*, 17:1287, 1987.
- [24] S. Mavlyankariyev, H. Schwarz, K. Korup, M. Geske, C.F. Goldsmith, R. Schlögl, and R. Horn. Screening of microkinetic gas-phase mechanisms for fuel-rich methane oxidation. *to be submitted*, 2013.
- [25] Alan C. Eckbreth. *Laser diagnostics for combustion temperature and species*, volume 7 of *Energy and engineering science series*. Abacus Press, Tunbridge Wells, 1988.
- [26] J.D. Jackson. *Classical electrodynamics*. Wiley, 1975.
- [27] B.E.A. Saleh and M.C. Teich. *Fundamentals of Photonics*. Wiley Series in Pure and Applied Optics. Wiley, 2007.

BIBLIOGRAPHY

- [28] L. Bergmann, H.J. Eichler, H. Niedrig, and C. Schäfer. *Optik: Wellen- und Teilchenoptik*. Bergmann Schaefer – Lehrbuch der Experimentalphysik. Gruyter, Walter de GmbH, 2004.
- [29] Joseph Fielding, Jonathan H. Frank, Sebastian A. Kaiser, Mitchell D. Smooke, and Marshall B. Long. Polarized/depolarized rayleigh scattering for determining fuel concentrations in flames. *Proceedings of the Combustion Institute*, 29(2):2703 – 2709, 2002.
- [30] G. Herzberg. *Molecular Spectra and Molecular Structure: II. Infrared and Raman Spectra of Polyatomic Molecules*. Molecular Spectra and Molecular Structure. D. Van Nostrand Company, Inc., 1964.
- [31] G. Herzberg. *Molecular Spectra and Molecular Structure: III. Electronic Spectra of Polyatomic Molecules*. Molecular Spectra and Molecular Structure. D. Van Nostrand Company, Inc., 1966.
- [32] G.D. Billing and K.V. Mikkelsen. *Introduction/Advanced Molecular Dynamics and Chemical Kinetics*. John Wiley & Sons Australia, Limited, 1997.
- [33] H.B. Callen. *Thermodynamics and an Introduction to Thermostatistics*. Wiley, 1985.
- [34] Henry Eyring. The activated complex in chemical reactions. *The Journal of Chemical Physics*, 3(2):107–115, 1935.
- [35] Svante Arrhenius. Über die reaktionsgeschwindigkeit bei der inversion von rohrzucker durch säuren. *Zeitschrift für physikalische Chemie*, 4:226, 1889.
- [36] Osborne Reynolds. *The Sub-Mechanics of the Universe*. Papers on Mechanical and Physical Subjects. Cambridge University Press, 1903.
- [37] J.C. Slattery. *Momentum, energy, and mass transfer in continua*. R.E. Krieger Pub. Co., 1981.
- [38] Hermann Schlichting. *Boundary-layer theory*. McGraw-Hill series in mechanical engineering. McGraw-Hill, New York, 7 edition, 1979.
- [39] R.J Kee, M.E Coltrin, and P. Glarborg. *Chemically Reacting Flow: Theory and Practice*. John Wiley & Sons, 2005.
- [40] ANSYS 14.0. Fluent theory guide, 2012.
- [41] L. D. Pfefferle and W. C. Pfefferle. Catalysis in Combustion. *Catalysis Reviews: Science and Engineering*, 29(2):219–267, 1987.
- [42] X. Song, W. R. Williams, L. D. Schmidt, and R. Aris. Ignition and extinction of homogeneous-heterogeneous combustion: CH₄ and C₃H₈ oxidation on Pt: Twenty-Third Symposium (International) on Combustion. *Symposium (International) on Combustion*, 23(1):1129–1137, 1991.
- [43] W.R. Williams, M.T. Stenzel, X. Song, and L.D. Schmidt. Bifurcation behavior in homogeneous-heterogeneous combustion: I. experimental results over platinum. *Combustion and Flame*, 84(3-4):277 – 291, 1991.

- [44] R.J. Olsen, W.R. Williams, X. Song, L.D. Schmidt, and R. Aris. Dynamics of homogeneous-heterogeneous reactors. *Chemical Engineering Science*, 47(9–11):2505 – 2510, 1992. Twelfth International Symposium on Chemical Reaction Engineering Today.
- [45] W. Meier and O. Keck. Laser raman scattering in fuel-rich flames: background levels at different excitation wavelengths. *Measurement Science and Technology*, 13(5):741, 2002.
- [46] M. C. Drake, M. Lapp, and C. M. Penney. Use of the vibrational Raman effect for gas temperature measurements. In James F. Schooley, editor, *Temperature*. American Inst. of Physics, New York, 1982.
- [47] Normand M. Laurendeau. Temperature measurements by light-scattering methods. *Progress in Energy and Combustion Science*, 14(2):147 – 170, 1988.
- [48] Derek Albert Long. *Raman spectroscopy*. McGraw-Hill, New York, 1977.
- [49] Peter F. Bernath. *Spectra of Atoms and Molecules*. Oxford University Press, USA, 2005.
- [50] A. R. Masri, R. W. Dibble, and R. S. Barlow. The structure of turbulent non-premixed flames revealed by Raman-Rayleigh-LIF measurements. *Progress in Energy and Combustion Science*, 22(4):307–362, 1996.
- [51] Andreas Brockhinke, Ulrich Lenhard, Andreas Bulter, and Katharina Kohse-Hoinghaus. Energy transfer in the OH A²Σ⁺ state: The role of polarization and of multi-quantum energy transfer. *Phys. Chem. Chem. Phys.*, 7(5):874–881, 2005.
- [52] David R. Yarkony. A theoretical treatment of the predissociation of the individual rovibronic levels of OH/OD(A²Σ⁺). *The Journal of Chemical Physics*, 97(3):1838–1849, 1992.
- [53] J. J. L. Spaanjaars, J. J. ter Meulen, and G. Meijer. Relative predissociation rates of OH (A²Σ⁺, v[′] = 3) from combined cavity ring down—Laser-induced fluorescence measurements. *J. Chem. Phys.*, 107(7):2242–2248, 1997.
- [54] Richard A. Copeland and David R. Crosley. Rotational level dependence of electronic quenching of OH(A²Σ⁺, [nu][′] = 0). *Chemical Physics Letters*, 107(3):295–300, 1984.
- [55] W. Ketterle, M. Schäfer, A. Arnold, and J. Wolfrum. 2D single-shot imaging of OH radicals using tunable excimer lasers. *Applied Physics B: Lasers and Optics*, 54(2):109–112, 1992.
- [56] Wolfgang Demtröder. *Laser Spectroscopy: Vol. 2 Experimental Techniques*. Springer-Verlag, Berlin and Heidelberg, 4 edition, 2008.
- [57] Terrill A. Cool. Quantitative measurement of NO density by resonance three-photon ionization. *Applied optics*, 23(10):1559 EP – 1572, 1984.

BIBLIOGRAPHY

- [58] Kermi C. Smyth and Philip H. Taylor. Detection of the methyl radical in a methane/air diffusion flame by multiphoton ionization spectroscopy. *Chemical Physics Letters*, 122(5):518–522, 1985.
- [59] Ulrich Boesl. Laser mass spectrometry for environmental and industrial chemical trace analysis. *Journal of Mass Spectrometry*, 35(3):289–304, 2000.
- [60] Katharina Kohse-Hoinghaus, Alexander Schocker, Tina Kasper, Michael Kamphus, and Andreas Brockhinke. Combination of laser- and mass-spectroscopic techniques for the investigation of fuel-rich flames. *Zeitschrift für Physikalische Chemie*, 219(5):583–599, 2005.
- [61] N. Hansen, T. A. Cool, P. R. Westmoreland, and K. Kohse-Hoinghaus. Recent contributions of flame-sampling molecular-beam mass spectrometry to a fundamental understanding of combustion chemistry. *Progress in Energy and Combustion Science*, 35(2):168–191, 2009.
- [62] Yue Wu, Andrew Bottom, Zhili Zhang, Timothy M. Ombrello, and Viswanath R. Katta. Direct measurement of methyl radicals in a methane/air flame at atmospheric pressure by radar rempi. *Opt. Express*, 19(24):23997–24004, Nov 2011.
- [63] Jordan Sawyer, Yue Wu, Zhili Zhang, and Steven F. Adams. O₂ rotational temperature measurements in an atmospheric air microdischarge by radar resonance-enhanced multiphoton ionization. *Journal of Applied Physics*, 113(23):233304, 2013.
- [64] Katharina Kohse-Hoinghaus and Jay Barker Jeffries. *Applied combustion diagnostics*. Combustion. Taylor & Francis, New York, 2002.
- [65] Brian J. Boothe, Albert J. Shih, Jian Kong, and William L. Roberts. Goniometric characteristics of optical fibres for temperature measurement in diesel engine exhaust filters. *Measurement Science and Technology*, 14(5):563, 2003.
- [66] Eric Jourdanneau, Frederic Chaussard, Robert Saint-Loup, Tony Gabard, and Hubert Berger. The methane raman spectrum from 1200 to 5500 cm⁻¹: A first step toward temperature diagnostic using methane as a probe molecule in combustion systems. *Journal of Molecular Spectroscopy*, 233(2):219 – 230, 2005.
- [67] Eric Jourdanneau, Tony Gabard, Frederic Chaussard, Robert Saint-Loup, Hubert Berger, Elena Bertseva, and Frederic Grisch. {CARS} methane spectra: Experiments and simulations for temperature diagnostic purposes. *Journal of Molecular Spectroscopy*, 246(2):167 – 179, 2007.
- [68] C. Miesse, R. Masel, M. Short, and M. Shannon. Experimental observations of methane-oxygen diffusion flame structure in a sub-millimetre microburner. *Combustion Theory and Modelling*, 9(1):77–92, 2005.
- [69] F. L. Dryer. High temperature oxidation of carbon monoxide and methane in a turbulent flow reactor. PhD Thesis, Princeton University, 1972.
- [70] Alexander Schocker, Katharina Kohse-Hoinghaus, and Andreas Brockhinke. Quantitative determination of combustion intermediates with cavity ring-down spectroscopy: systematic study in propene flames near the soot-formation limit. *Applied Optics*, 44(31):6660–6672, 2005.

- [71] J. W. Daily. Laser induced fluorescence spectroscopy in flames. *Progress in Energy and Combustion Science*, 23(2):133–199, 1997.
- [72] R. Reichle, C. Pruss, W. Osten, H. J. Tiziani, F. Zimmermann, and C. Schulz. Fiber optic spark plug sensor for UV-LIF-measurements close to the ignition spark. In W. Osten, C. Gorecki, and E. Novak, editors, *Optical Measurement Systems for Industrial Inspection IV, Pts 1 and 2*, volume 5856 of *Proceedings of the Society of Photo-Optical Instrumentation Engineers*, pages 158–168, 2005.
- [73] Ian R. Lewis and Peter R. Griffiths. Raman Spectrometry with Fiber-Optic Sampling. *Appl. Spectrosc.*, 50(10):12A–30A, 1996.
- [74] J. Luque and D. R. Crosley. LIFBASE: Database and spectral simulation (version 2.1). *SRI International Report*, MP 99-009, 1999.
- [75] Brett E. Battles and Ronald K. Hanson. Laser-induced fluorescence measurements of NO and OH mole fraction in fuel-lean, high-pressure (1-10 atm) methane flames: Fluorescence modeling and experimental validation. *Journal of Quantitative Spectroscopy and Radiative Transfer*, 54(3):521–537, 1995.
- [76] M. Lapp, L. Goldman, and C. Penney. Raman scattering in flames. *Science*, 175(4026), 1972.
- [77] G. Gruenefeld, V. Beushausen, and P. Andresen. Interference-free UV-laser-induced Raman and Rayleigh measurements in hydrocarbon combustion using polarization properties. *Applied physics. B, Lasers and optics*, B61(5):473 EP – 478, 1995.
- [78] R. J. Kee, F. M. Rupley, J. A. Miller, M. E. Coltrin, J. F. Grcar, E. Meeks, H. K. Moffat, A. E. Lutz, G. Dixon-Lewis, M. D. Smooke, J. Warnatz, G. H. Evans, R. S. Larson, R. E. Mitchell, L. R. Petzold, W. C. Reynolds, M. Caracotsios, W. E. Stewart, P. Glarborg, C. Wang, C. L. McLellan, O. Adigun, W. G. Houf, C. P. Chou, S. F. Miller, P. Ho, P. D. Young, D. J. Young, D. W. Hodgson, M. V. Petrova, and K. V. Puduppakkam. CHEMKIN 15101, 2011.
- [79] T. Schmidt Uhlig, P. Karlitschek, G. Marowsky, and Y. Sano. New simplified coupling scheme for the delivery of 20 MW Nd:YAG laser pulses by large core optical fibers: YAG laser pulses by large core optical fibers. *Applied physics. B, Lasers and optics*, 72(2):183 EP – 186, 2001.
- [80] B. Richou and P. Pellat-Finet. Delivery of Nd-YAG laser pulses by large optical fiber: Dependence of the laser intensity profile on threshold of energy transmission. *High-Power Lasers: Applications and Emerging Applications*, 2789:186 EP – 194, 1996.
- [81] Duncan P Hand, Jonathan D Entwistle, Robert R J Maier, Andreas Kuhn, Clive A Greated, and Julian D C Jones. Fibre optic beam delivery system for high peak power laser PIV illumination. *Measurement Science and Technology*, 10(3):239, 1999.
- [82] Guey-Liou Lan, P. K. Banerjee, and S. S. Mitra. Raman scattering in optical fibers. *Journal of Raman Spectroscopy*, 11(5):416–423, 1981.

BIBLIOGRAPHY

- [83] Hiroaki Imai and Hiroshi Hirashima. Intrinsic- and extrinsic-defect formation in silica glasses by radiation: Proceedings of the First PAC RIM Meeting on Glass and Optical Materials. *Journal of Non-Crystalline Solids*, 179(0):202–213, 1994.
- [84] P. Karlitschek, G. Hillrichs, and K. F Klein. Photodegradation and nonlinear effects in optical fibers induced by pulsed uv-laser radiation. *Optics Communications*, 116(1-3):219–230, 1995.
- [85] P. Karlitschek, G. Hillrichs, and K. F Klein. Influence of hydrogen on the colour center formation in optical fibers induced by pulsed UV-laser radiation.: Part 2: All-silica fibers with low-OH undoped core. *Optics Communications*, 155(4-6):386–397, 1998.
- [86] Paul Hsu, Anil Patnaik, James Gord, Terrence Meyer, Waruna Kulatilaka, and Sukesh Roy. Investigation of optical fibers for coherent anti-Stokes Raman scattering (CARS) spectroscopy in reacting flows. *Experiments in Fluids*, pages 1–16, 2010.
- [87] Yoshimitsu Amenomiya, Viola I. Birss, Maciej Goleczynski, Jan Galuszka, and Alan R. Sanger. Conversion of Methane by Oxidative Coupling. *Catalysis Reviews: Science and Engineering*, 32(3):163–227, 1990.
- [88] Daniel J. Driscoll, Wilson Martir, Ji Xiang Wang, and Jack H. Lunsford. Formation of gas-phase methyl radicals over magnesium oxide. *J. Am. Chem. Soc.*, 107(1):58–63, 1985.
- [89] Graham J. Hutchings, Michael S. Scurrall, and Jeremy R. Woodhouse. The role of gas phase reaction in the selective oxidation of methane. *Journal of the Chemical Society, Chemical Communications*, 4:253–255, 1988.
- [90] Gerald S. Lane and Eduardo E. Wolf. Methane utilization by oxidative coupling: I. A study of reactions in the gas phase during the cofeeding of methane and oxygen. *Journal of Catalysis*, 113(1):144–163, 1988.
- [91] John C. Mackie. Partial Oxidation of Methane: The Role of the Gas Phase Reactions. *Catalysis Reviews*, 33(1-2):169–240, 1991.
- [92] R. Horn, O. Korup, M. Geske, U. Zavyalova, I. Oprea, and R. Schlögl. Reactor for in situ measurements of spatially resolved kinetic data in heterogeneous catalysis. *Review of Scientific Instruments*, 81(6):064102, 2010.
- [93] Heiner Schwarz, Robert Schlögl, and Raimund Horn. Radical detection in harsh environments by means of laser-induced fluorescence using a single bidirectional optical fiber. *Applied Physics B*, 109(1):19–26, 2012.
- [94] C. A. Mims, R. Mauti, A. M. Dean, and K. D. Rose. Radical Chemistry in Methane Oxidative Coupling: Tracing of Ethylene Secondary Reactions with Computer Models and Isotopes. *J. Phys. Chem.*, 98(50):13357–13372, 1994.
- [95] Joel E. Harrington and Kermit C. Smyth. Laser-induced fluorescence measurements of formaldehyde in a methane/air diffusion flame. *Chemical Physics Letters*, 202(3–4):196–202, 1993.

- [96] Christian Brackmann, Jenny Nygren, Xiao Bai, Zhongshan Li, Henrik Bladh, Boman Axelsson, Ingemar Denbratt, Lucien Koopmans, Per-Erik Bengtsson, and Marcus Aldén. Laser-induced fluorescence of formaldehyde in combustion using third harmonic Nd:YAG laser excitation. *Spectrochimica Acta Part A: Molecular and Biomolecular Spectroscopy*, 59(14):3347–3356, 2003.
- [97] D. J. Clouthier and D. A. Ramsay. The Spectroscopy of Formaldehyde and Thioformaldehyde. *Annu. Rev. Phys. Chem.*, 34(1):31–58, 1983.
- [98] Bärbel Maessen and Max Wolfsberg. Variational calculation of lower vibrational energy levels of formaldehyde X 1A1. *The Journal of Chemical Physics*, 80(10):4651, 1984.
- [99] G. H. Dieke and G. B. Kistiakowsky. The Structure of the Ultraviolet Absorption Spectrum of Formaldehyde. I. *Physical Review*, 45(1):4–28, 1934.
- [100] C. Brackmann, J. Bood, M. Aldén, G. Pengloan, and Ö. Andersson. Quantitative measurements of species and temperature in a DME-air counterflow diffusion flame using laser diagnostic methods. *Combustion Science and Technology*, 178(6):1165–1184, 2006.
- [101] D. I. Shin, G. Peiter, T. Dreier, H.-R Volpp, and J. Wolfrum. Spatially resolved measurements of CN, CH, NH, and H₂CO concentration profiles in a domestic gas boiler. *Proceedings of the Combustion Institute*, 28(1):319–325, 2000.
- [102] D.I Shin, T. Dreier, and J. Wolfrum. Spatially resolved absolute concentration and fluorescence-lifetime determination of H₂CO in atmospheric-pressure CH₄/air flames. *Applied Physics B*, 72(2):257–261, 2001.
- [103] J. Tobai and T. Dreier. Effective A-state fluorescence lifetime of formaldehyde in atmospheric pressure CH₄/air flames. *Applied Physics B: Lasers and Optics*, 74(1):101–104, 2002.
- [104] A. Ehn, O. Johansson, J. Bood, A. Arvidsson, B. Li, and M. Aldén. Fluorescence lifetime imaging in a flame. *Proceedings of the Combustion Institute*, 33(1):807–813, 2011.
- [105] Juan Li, Zhenwei Zhao, Andrei Kazakov, and Frederick L. Dryer. An updated comprehensive kinetic model of hydrogen combustion, 2004.
- [106] D. Healy, H.J Curran, J.M Simmie, D.M Kalitan, C.M Zinner, A.B Barrett, E.L Petersen, and G. Bourque. Methane/ethane/propane mixture oxidation at high pressures and at high, intermediate and low temperatures. *Combustion and Flame*, 155(3):441–448, 2008.
- [107] V. K. Bityukov and V. A. Petrov. Optical quartz glass as a reference substance for the thermal conductivity coefficient of partially transparent materials. *High Temperature*, 38(2):293–299, 2000.
- [108] Laxminarayan L. Raja, Robert J. Kee, Olaf Deutschmann, Juergen Warnatz, and Lanny D. Schmidt. A critical evaluation of Navier–Stokes, boundary-layer, and plug-flow models of the flow and chemistry in a catalytic-combustion monolith. *Catalysis Today*, 59(1–2):47–60, 2000.

BIBLIOGRAPHY

- [109] Thomas Metz, Xiao Bai, Frederik Ossler, and Marcus Aldén. Fluorescence lifetimes of formaldehyde (H₂CO) in the band system at elevated temperatures and pressures. *Spectrochimica Acta Part A: Molecular and Biomolecular Spectroscopy*, 60(5):1043–1053, 2004.
- [110] C. Brackmann, Z. Li, M. Rupinski, N. Docquier, G. Pengloan, and M. Aldén. Strategies for formaldehyde detection in flames and engines using a single-mode Nd:YAG/OPO laser system. *Applied Spectroscopy*, 59(6):763–768, 2005.
- [111] B.C Connelly, B.A.V Bennett, M.D Smooke, and M.B Long. A paradigm shift in the interaction of experiments and computations in combustion research. *Proceedings of the Combustion Institute*, 32(1):879–886, 2009.
- [112] Xing-hai Zhao, Yang Gao, Wen-yong Cheng, Yong-sheng Cheng, Wei Su, Jonathan A. Terry, Thomas Graf, and Helena Jelinkova. Novel coupling device of high peak power pulsed laser to multimode fiber. *Proc. SPIE*, 6998(1):69980O–8, 2008.
- [113] Subrata Bhattacharjee and William L. Grosshandler. Effect of radiative heat transfer on combustion chamber flows. *Combustion and Flame*, 77(3–4):347–357, 1989.
- [114] C. L. Tien. Thermal radiation properties of gases. In Jr. T. F. Irvine and J. P. Hartnett, editors, *Advances in Heat Transfer*, volume 5, pages 253–324. Academic Press, New York, 1968.
- [115] O. Deutschmann, F. Behrendt, and J. Warnatz. Modelling and simulation of heterogeneous oxidation of methane on a platinum foil. *Catalysis Today*, 21(2–3):461–470, 1994.
- [116] James T. Wiswall, Margaret S. Wooldridge, and Hong G. Im. An experimental study of the effects of platinum on methane/air and propane/air mixtures in a stagnation point flow reactor. *Journal of Heat Transfer*, 131(11):111201, 2009.
- [117] K.Heitnes Hofstad, O.A. Rokstad, and A. Holmen. Partial oxidation of methane over platinum metal gauze. *Catalysis Letters*, 36(1-2):25–30, 1996.
- [118] C.R.H. de Smet, M.H.J.M. de Croon, R.J. Berger, G.B. Marin, and J.C. Schouten. An experimental reactor to study the intrinsic kinetics of catalytic partial oxidation of methane in the presence of heat-transport limitations. *Applied Catalysis A: General*, 187(1):33–48, 1999.
- [119] Mark B. Davis, Michael D. Pawson, Götz Vesper, and Lanny D. Schmidt. Methane oxidation over noble metal gauzes: an {LIF} study. *Combustion and Flame*, 123(1-2):159 – 174, 2000.
- [120] C.R.H. de Smet, M.H.J.M. de Croon, R.J. Berger, G.B. Marin, and J.C. Schouten. Kinetics for the partial oxidation of methane on a pt gauze at low conversion. *AIChE J*, 46(9):1837–1849, 2000.
- [121] R. Quiceno, J. Pérez-Ramírez, J. Warnatz, and O. Deutschmann. Modeling the High Temperature Catalytic Partial Oxidation of Methane over Platinum Gauze: Detailed Gas-Phase and Surface Chemistries Coupled with 3D Flow Field Simulations. *Appl. Catal. A: General*, 303:166–176, 2006.

- [122] R. Quiceno, O. Deutschmann, J. Warnatz, and J. Pérez-Ramírez. Rational modeling of the {CPO} of methane over platinum gauze: Elementary gas-phase and surface mechanisms coupled with flow simulations. *Catalysis Today*, 119(1–4):311–316, 2007.
- [123] D.A. Hickman and L.D. Schmidt. Synthesis gas formation by direct oxidation of methane over pt monoliths. *Journal of Catalysis*, 138(1):267 – 282, 1992.
- [124] A. Bitsch-Larsen, R. Horn, and L.D. Schmidt. Catalytic partial oxidation of methane on rhodium and platinum: Spatial profiles at elevated pressure. *Applied Catalysis A: General*, 348(2):165–172, 2008.
- [125] Oliver Korup, Claude Franklin Goldsmith, Gisela Weinberg, Michael Geske, Timur Kandemir, Robert Schlögl, and Raimund Horn. Catalytic partial oxidation of methane on platinum investigated by spatial reactor profiles, spatially resolved spectroscopy, and microkinetic modeling. *Journal of Catalysis*, 297:1–16, 2013.
- [126] Michael Reinke, John Mantzaras, Rolf Bombach, Sabine Schenker, and Andreas Inauen. Gas phase chemistry in catalytic combustion of methane/air mixtures over platinum at pressures of 1 to 16 bar. *Combustion and Flame*, 141(4):448–468, 2005.
- [127] Edvard Bergene, Olav Tronstad, and Anders Holmen. Surface areas of Pt-Rh catalyst gauzes used for ammonia oxidation. *Journal of Catalysis*, 160(2):141 – 147, 1996.
- [128] Gregory P. Smith, David M. Golden, Michael Frenklach, Nigel W. Moriarty, Boris Eiteneer, Mikhail Goldenberg, C. Thomas Bowman, Ronald K. Hanson, Soonho Song, William C. Gardiner Jr., Vitali V. Lissianski, and Zhiwei Qin. GRI 3.0. http://www.me.berkeley.edu/gri_mech/, 1999.